BRNO UNIVERSITY OF TECHNOLOGY
VYSOKÉ UČENÍ TECHNICKÉ V BRNĚ

FACULTY OF MECHANICAL ENGINEERING
INSTITUTE OF PHYSICAL ENGINEERING

FAKULTA STROJNÍHO INŽENÝRSTVÍ
ÚSTAV FYZIKÁLNÍHO INŽENÝRSTVÍ

STUDY OF OPTICAL PROPERTIES OF METALLIC STRUCTURES AND THEIR APPLICATIONS IN NANO-OPTICS

MASTER'S THESIS
DIPLOMOVÁ PRÁCE

AUTHOR TOMÁŠ NEUMAN
AUTOR PRÁCE

BRNO 2014

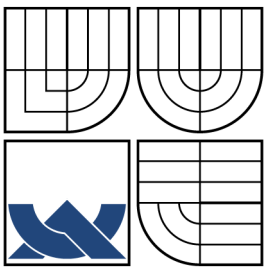

BRNO UNIVERSITY OF TECHNOLOGY
VYSOKÉ UČENÍ TECHNICKÉ V BRNĚ

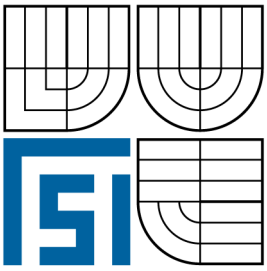

FACULTY OF MECHANICAL ENGINEERING
INSTITUTE OF PHYSICAL ENGINEERING

FAKULTA STROJNÍHO INŽENÝRSTVÍ
ÚSTAV FYZIKÁLNÍHO INŽENÝRSTVÍ

STUDY OF OPTICAL PROPERTIES OF METALLIC STRUCTURES AND THEIR APPLICATIONS IN NANO-OPTICS

STUDIUM OPTICKÝCH VLASTNOSTÍ KOVOVÝCH STRUKTUR A JEJICH VYUŽITÍ V NANOOPTICE

MASTER'S THESIS
DIPLOMOVÁ PRÁCE

AUTHOR
AUTOR PRÁCE
Bc. TOMÁŠ NEUMAN

SUPERVISOR
VEDOUCÍ PRÁCE
doc. Ing. RADEK KALOUSEK, Ph.D.

BRNO 2014

Vysoké učení technické v Brně, Fakulta strojního inženýrství

Ústav fyzikálního inženýrství
Akademický rok: 2013/2014

ZADÁNÍ DIPLOMOVÉ PRÁCE

student(ka): Bc. Tomáš Neuman

který/která studuje v **magisterském navazujícím studijním programu**

obor: **Fyzikální inženýrství a nanotechnologie (3901T043)**

Ředitel ústavu Vám v souladu se zákonem č.111/1998 o vysokých školách a se Studijním a zkušebním řádem VUT v Brně určuje následující téma diplomové práce:

Studium optických vlastností kovových struktur a jejich využití v nanooptice

v anglickém jazyce:

Study of Optical Properties of Metallic Structures and Their Applications in Nano-Optics

Stručná charakteristika problematiky úkolu:

Analytický popis interakce světla se strukturami různých tvarů bývá zpravidla dosti komplikovaný, proto se pro tyto výpočty hojně využívá numerických metod. Při použití těchto metod se však mnohdy objevují vážné problémy, např. pomalá konvergence, vysoké nároky na výpočetní techniku, obtížně zachytitelné závislosti různých fyzikálních veličin na vstupních parametrech, aj. Hledání dalších analytických metod se tedy stále jeví jako nezbytné pro studium fyzikálních vlastností struktur, zejména nanostruktur, jejichž rozměry jsou srovnatelné nebo menší než 100 nm.

Cíle diplomové práce:

1. Proveďte rešeršní studii současného stavu poznání interakce světla s nanostrukturami a možných aplikací kovových nanostruktur v plazmonice.
2. Navrhněte teoretický popis interakce světla s kovovými nanostrukutrami a zkoumejte vliv přítomnosti sondy mikroskopie v blízkém poli.
3. Navrhněte experimenty, které by prokázaly adekvátnost teoretického popisu a jejichž výsledky by mohly být využity pro aplikace, např. pro studium fotoluminiscence.

Seznam odborné literatury:

[1] L. Novotny, B. Hecht: Principles of Nano-Optics. Cambridge 2006.
[2] Optical Antennas. Ed.: M. Agio, A. Alu, Cambridge University Press 2013.

Vedoucí diplomové práce: doc. Ing. Radek Kalousek, Ph.D.

Termín odevzdání diplomové práce je stanoven časovým plánem akademického roku 2013/2014.

V Brně, dne 5.12.2013

L.S.

_____	_____
prof. RNDr. Tomáš Šikola, CSc.	prof. RNDr. Miroslav Doupovec, CSc., dr. h. c.
Ředitel ústavu	Děkan fakulty

ABSTRACT

Interaction of metallic structures with electromagnetic radiation is a living topic of near-field optics including plasmonics and nanophotonics. The field-matter interaction treated on the subwavelength scale opens the path to a wide range of applications, among others to different variants of the surface enhanced spectroscopy. In this thesis we theoretically describe how the near-field properties of the metallic structures can be accessed by a probe of near-field scanning optical microscope. Formation of the signal in the near-field microscopy utilizing weakly interacting probes is discussed. Further, we elucidate the mechanism of the surface enhanced infrared spectroscopy. We utilize a model example of linear dipole antennas interacting with sample structures. A close connection is found between the spectroscopic signal and signal of the scattering type near-field optical microscopy.

KEYWORDS

Infrared antenna, SNOM, plasmonics, infrared spectroscopy

ABSTRAKT

Interakce kovových struktur s elektromagnetickým zářením je živoucím tématem oboru optiky blízkého pole, které zahrnuje oblasti plasmoniky a nanofotoniky. Interakce světla a látky na rozměrech menších než vlnová délka záření otevírají možnosti aplikacím, jakými jsou mezi jinými nejrůznější varianty povrchově zesílené spektroskopie. V této práci se teoreticky zabýváme mapováním vlastností blízkého pole kovových struktur pomocí mikroskopie v blízkém poli rozptylového typu. Diskutujeme zde mechanismus tvorby signálu za podmínek, kdy je možné sondu mikroskopu považovat za slabě rozptylující. V další části práce objasňujeme mechanismus povrchově zesílené infračervené spektroskopie pomocí numerických simulací a analytického modelu. Aparát aplikujeme na systém lineární dipólové antény interagující s vrstvou vzorku. Pomocí analytického modelu a numerických simulací nalézáme na vhodném modelu spojení mezi formací spektroskopického signálu a signálu mikroskopie v blízkém poli.

KLÍČOVÁ SLOVA

Infračervená anténa, SNOM, plasmonika, infračervená spektroskopie

NEUMAN, T. Studium optických vlastností kovových struktur a jejich využití v nanooptice. Brno: Vysoké učení technické v Brně, Fakulta strojního inženýrství, 2014. 94 s. Vedoucí diplomové práce doc. Ing. Radek Kalousek, Ph.D.

PROHLÁŠENÍ

Prohlašuji, že svou diplomovou práci na téma „Study of Optical Properties of Metallic Structures and Their Applications in Nano-Optics“ jsem vypracoval samostatně pod vedením vedoucího diplomové práce a s použitím odborné literatury a dalších informačních zdrojů, které jsou všechny citovány v práci a uvedeny v seznamu literatury na konci práce.

Jako autor uvedené diplomové práce dále prohlašuji, že v souvislosti s vytvořením této diplomové práce jsem neporušil autorská práva třetích osob, zejména jsem nezasáhl nedovoleným způsobem do cizích autorských práv osobnostních a jsem si plně vědom následků porušení ustanovení § 11 a následujících autorského zákona č. 121/2000 Sb., včetně možných trestněprávních důsledků vyplývajících z ustanovení § 152 trestního zákona č. 140/1961 Sb.

V Brně dne ....

(podpis autora)

Acknowledgement

I thank my supervisor Doc. Radek Kalousek for inspiring discussions and proof-reading. My gratitude belongs to Dr. Javier Aizpurua who kindly introduced me to the topic of the scattering-type near-field scanning optical microscopy from the theoretical point of view and who treated me as a regular member of his group in San Sebastián. I also thank Javier for his kindness and patience with me. The work would not be possible without Dr. Rainer Hillenbrand and his group, who provided the experimental s-SNOM images. I also thank them for showing me the practical site of the scattering-type near-field optical microscopy. I want to express my gratitude to Prof. Annemarie Pucci who helped me to gain insight into the field of surface enhanced infrared spectroscopy. I thank people who helped me with corrections of the text as well, namely: Andrea Konečná, Michal Staňo, Jonáš Gloss, Prof. Jiří Spousta and Prof. Petr Dub. My gratitude also belongs to all the people who helped me during my studies and supported me not only by fruitful scientific discussions but also by their friendship. Last but not least, I thank my family for their support during my whole studies and for their love.

Contents

1 | Introduction

The discovery of extraordinary light-matter interaction of noble metal structures gave rise to a new branch of scientific research, nowadays called plasmonics. The collective oscillations of electrons, plasmons, and their coupling with photons was found to be the mechanism promising applications in the areas of information technology, sensorics, medical applications or enhancement of optical and infrared spectroscopy and many others. The large research of plasmonic waveguides discovered severe obstacle for practical plasmon waveguide applications, the losses. The long range waveguiding using surface plasmon polaritons seems today as one of unfulfilled wishes even though the short range signal handling by plasmons is still an open task.

Discovery and manufacturing of optical antennas [1–3], the nanometer-sized metallic structures which interact with the light similarly as the radio antennas with the radio waves, enabled manipulation with the light on nanoscale. The optical and analogously the infrared antennas are capable of focusing the electromagnetic radiation to nanometric areas and provide strong field enhancements [4–6]. The electromagnetic near-fields are nowadays widely exploited for enhancement of spectroscopic signals in both visible and infrared part of the spectrum [6–17]. Recent progress in nanofabrication techniques allows for tailoring of the near-field optical properties of the artificial metallic antennas by precise fabrication of their shapes and sizes.

Both, the theoretical and the experimental studies of the interaction of light with the antennas are therefore needed for design of proper antenna geometry and understanding processes taking place in the antenna near-field regions. The interaction of light with the structures is in most cases treated within the framework of the classical Maxwell's theory. The quantum mechanical effects are usually encompassed in the phenomenological dielectric function with sufficient accuracy. Recently it was pointed out that the quantum mechanical nature of the antenna material blurs the antenna borders and must be taken into account when subnanometer features are treated [18]. Today, numerical methods are well established for exact calculation of antenna spectral response to the incident light including the calculation of the near-field distribution. Among others, the method of finite elements, the method of boundary elements, method of finite differences or the discrete dipole approximation have strong position in the computational electrodynamics [19, 20].

The numerical methods are often not sufficiently insightful when understanding of underlying physical mechanisms is required. The analytical methods are irreplaceable in this situation, even though they often do not provide a perfect match with experiment. The analytical methods also suit for solution of problems hardly tractable by means of conventional numerical methods. A typical example is a cal-

culation of objects with shape singularities, such as cylinders touching the substrate at a single spot or objects having sharp corners in general. A transformation optics approach has proven useful in these situations [21–23] even though the considered singular geometries are rather unrealistic due to the quantum mechanical effects [18].

Experimental investigation of light interaction with metallic antennas employs two basic different approaches, the far-field spectroscopic measurements and the near-field microscopy. The far-field methods utilize conventional optics for illumination and collection of light. The detected signal carries information about the total antenna response to the illumination but are not able to resolve the detailed near-field antenna properties which are so important for understanding of processes taking place at nanoscale. The main constraint for resolution of the conventional optics is the Ryleigh diffraction limit. An ingenious idea to put a near-field probe into the vicinity of the antenna enabled development of a new type of optical microscopy, the near-field optical microscopy.

Surprisingly, the idea of the near-field optical imaging was originally proposed by Synge back in 1928 [24, 25]. However, the authority of Albert Einstein, who did not believe in application potential of the method, forced Synge to publish the concept of the near-field microscopy without further experimental studies and effectively prevented further development of the method. The experimental realization of the near-field optical microscope had to wait decades until it became one of the fastest developing and most successful nano-imaging optical techniques.

It is impossible to devote the thesis to the whole wide area of plasmonics and all of its applications. This thesis will predominantly deal with near-field characterization of the infrared antennas by scanning near-field optical microscopy and their application in surface enhanced infrared spectroscopy. In Chapter 2, the reader will be introduced to the theory of electromagnetic scattering based on the volume integral formulation. The following Chapter 3 will apply the formalism to the near-field scanning optical microscopy of scattering type and present an interpretation of infrared antenna near-field images. Chapter 4 will also briefly touch interesting novel developments of the near-field microscopy elucidating the properties of photoluminescence and spontaneous emission of point-like objects. The rest of the thesis will discuss one of the most prominent application of the metallic structures which is the field of an enhanced vibrational spectroscopy. Special attention will be paid to the field of surface enhanced infrared spectroscopy. We will discuss here interpretation of the measured spectra in terms of the electromagnetic coupling between the antenna and the sample modes.

This thesis brings novel view of the near-field microscopy in terms of the mixing of near-field components and sets a basis for further theoretical and experimental studies. The presented original results in the field of the surface enhanced infrared spectroscopy should help to understand the mechanism of spectroscopic signal formation and should also provide a bridge between the otherwise separate areas of the near field microscopy and the far-field infrared spectroscopy.

2 | Electromagnetic scattering

The scattering theory of electromagnetic waves is a central method of light-matter interaction description on a classical level. Here, the material properties of the sample are treated phenomenologically and the fields are fully governed by the Maxwell's equations. Historically, a lot of effort has been devoted to the development of a description of the electromagnetic scattering, including the illustrious Rayleigh work on light scattering by small particles [26] or the widely used Mie theory [27] for scattering by spheres of an arbitrary size.

Among other analytical methods, the method of transformation optics is worth attention [21–23]. The transformation optics utilizes coordinate transformation to change the geometry of the scattering problem to analytically feasible situation. The method is however practically restricted to a limited amount of geometries and works best only for two dimensional problems and in quasi-static regime, where methods of complex analysis are naturally employed. The restriction of the method follows mainly from the necessity of utilizing a transform which does not change the material properties of the environment and only reshapes the space. A general transformation yields a highly anisotropic environment where the solution is even more difficult than in the original geometry.

In realistic situations where the field distribution or spectral response of metallic structures is desired numerical methods find an irreplaceable position. The numerical methods for electromagnetic scattering are well developed in recent times and most of them are available as either commercial or freely accessible computer codes. Among others we mention the commercial software FDTD Lumerical Solutions [28], which is based on the method of finite differences in time domain, or the Comsol Multiphysics software [29], which provides versatile computational environment utilizing the method of finite elements. The boundary element method based on formulation of the scattering problems via surface integrals [30] is also nowadays freely available as a MATLAB code [31].

In this work we will not attempt, nor intend, to provide a comprehensive review of various scattering models, but we will predominantly focus on a scattering model based on a volume integral formulation. The volume integral formulation, as we will see later, sheds light on physical principles of scattering for general geometries and provides deeper physical insight into studied processes such as surface enhanced infrared spectroscopy or interaction of light with probe of the near-field optical microscope.

2.1 Equations of electrodynamics

We will start our way towards the integral description of scattering by writing the laws of electrodynamics in the form of the Lorentz force law

$$\mathbf{F} = q\left(\mathbf{E} + \mathbf{v} \times \mathbf{B}\right), \tag{2.1}$$

where q is an electric charge moving with a velocity $\mathbf{v}$, and the Maxwell's equations

$$\nabla \cdot \mathbf{E} = \frac{\rho}{\varepsilon_0}, \tag{2.2}$$

$$\nabla \cdot \mathbf{B} = 0, \tag{2.3}$$

$$\nabla \times \mathbf{E} = -\frac{\partial \mathbf{B}}{\partial t}, \tag{2.4}$$

$$\nabla \times \mathbf{B} = \mu_0 \mathbf{j} + \mu_0 \varepsilon_0 \frac{\partial \mathbf{E}}{\partial t}, \tag{2.5}$$

by which the time evolution of the electric field $\mathbf{E}$, the magnetic induction $\mathbf{B}$, and their interaction with the source current density $\mathbf{j}$ and the charge density ρ is specified. Here ε_0 is the vacuum permittivity and μ_0 is the vacuum permeability. Velocity of light in vacuum is related to ε_0 and μ_0 by $c = 1/\sqrt{\varepsilon_0 \mu_0}$. The equations (2.1) to (2.5) describe, in general, behaviour of electromagnetic fields in arbitrary environments. From the macroscopic point of view, we can distinguish between charge and current densities confined to dielectric bodies, so called bound charges and currents, and free charges and currents which are inserted into the system externally. The bound charges and currents are usually incorporated in newly defined vector fields, an electric displacement $\mathbf{D}$ and a magnetic field $\mathbf{H}$:

$$\mathbf{D} = \varepsilon_0 \mathbf{E} + \mathbf{P}, \tag{2.6}$$

$$\mathbf{H} = \frac{1}{\mu_0}\mathbf{B} - \mathbf{M}. \tag{2.7}$$

The new vector fields which appear in definitions (2.6) and (2.7) are the electric polarization (or simply polarization) $\mathbf{P}$ and the magnetization $\mathbf{M}$. Precise and general definition of these vector fields is rather cumbersome, but intuitively and for most applications sufficiently, we can say that the polarization represents a volume density of an electric dipole moment and so does the magnetization for a magnetic dipole moment. Changes of the vector fields $\mathbf{P}$ and $\mathbf{M}$ (understand the derivatives) in space and time have straightforward physical meaning. Negative divergence of the polarization represents the density of bound charges:

$$\rho_\mathrm{b} = -\nabla \cdot \mathbf{P}, \tag{2.8}$$

on the other hand, density of bound currents comprises contributions from both, the time derivative of polarization ($\mathbf{j}_\mathrm{e}$) and the curl of magnetization ($\mathbf{j}_\mathrm{m}$):

$$\mathbf{j}_\mathrm{b} = \mathbf{j}_\mathrm{e} + \mathbf{j}_\mathrm{m} = \frac{\partial \mathbf{P}}{\partial t} + \nabla \times \mathbf{M}. \tag{2.9}$$

The relations (2.6) and (2.7) usually gain a different form by assuming a linear response of media to the external electromagnetic stimuli:

$$\mathbf{D}(\mathbf{r},t) = \varepsilon_0 \int \boldsymbol{\varepsilon}(\mathbf{r},\mathbf{r}',t,\tau)\cdot\mathbf{E}(\mathbf{r}',\tau)\mathrm{d}\mathbf{r}'\mathrm{d}\tau, \tag{2.10}$$

$$\mathbf{B}(\mathbf{r},t) = \mu_0 \int \boldsymbol{\mu}(\mathbf{r},\mathbf{r}',t,\tau)\cdot\mathbf{H}(\mathbf{r}',\tau)\mathrm{d}\mathbf{r}'\mathrm{d}\tau, \tag{2.11}$$

where $\boldsymbol{\varepsilon}$ and $\boldsymbol{\mu}$ are tensors of permittivity and permeability, relating fields $\mathbf{D}$ and $\mathbf{B}$ at some time t and position $\mathbf{r}$ to the fields $\mathbf{E}$ and $\mathbf{H}$ at all preceding times τ and all spatial positions $\mathbf{r}'$. Similar expression can be stated for relationship between the induced current density and the electric field:

$$\mathbf{j}(\mathbf{r},t) = \int \boldsymbol{\sigma}(\mathbf{r},\mathbf{r}',t,\tau)\cdot\mathbf{E}(\mathbf{r}',\tau)\mathrm{d}\mathbf{r}'\mathrm{d}\tau, \tag{2.12}$$

where $\boldsymbol{\sigma}$ is the tensor of conductivity.

The relations (2.10), (2.11) and (2.12) are said to be spatially and temporally non-local (in other words, to have spatial and temporal dispersion). For systems possessing translational symmetry, the non-locality manifests itself in the form of convolution and allows one to exploit the well known Fourier transform theorem. In the Fourier domain[1], the relations (2.10) and (2.11) read:

$$\mathbf{D}(\mathbf{k},\omega) = \mathcal{F}\left\{\varepsilon_0 \int \boldsymbol{\varepsilon}(\mathbf{r}-\mathbf{r}',t-\tau)\cdot\mathbf{E}(\mathbf{r}',\tau)\mathrm{d}\mathbf{r}'\mathrm{d}\tau\right\} = \varepsilon_0\boldsymbol{\varepsilon}(\mathbf{k},\omega)\cdot\mathbf{E}(\mathbf{k},\omega), \tag{2.13}$$

$$\mathbf{B}(\mathbf{k},\omega) = \mathcal{F}\left\{\mu_0 \int \boldsymbol{\mu}(\mathbf{r}-\mathbf{r}',t-\tau)\cdot\mathbf{H}(\mathbf{r}',\tau)\mathrm{d}\mathbf{r}'\mathrm{d}\tau\right\} = \mu_0\boldsymbol{\mu}(\mathbf{k},\omega)\cdot\mathbf{H}(\mathbf{k},\omega), \tag{2.14}$$

$$\mathbf{j}(\mathbf{k},\omega) = \mathcal{F}\left\{\mu_0 \int \boldsymbol{\sigma}(\mathbf{r}-\mathbf{r}',t-\tau)\cdot\mathbf{E}(\mathbf{r}',\tau)\mathrm{d}\mathbf{r}'\mathrm{d}\tau\right\} = \boldsymbol{\sigma}(\mathbf{k},\omega)\cdot\mathbf{E}(\mathbf{k},\omega), \tag{2.15}$$

where $\mathbf{k}$ and ω are Fourier variables having meaning of the propagation vector and the frequency in the plane wave decomposition of the electromagnetic field. In most applications, we can treat media as spatially local. By retaining only the time dispersion, we have:

$$\mathbf{D}(\mathbf{r},\omega) = \varepsilon_0\boldsymbol{\varepsilon}(\mathbf{r},\omega)\cdot\mathbf{E}(\mathbf{r},\omega), \tag{2.16}$$

$$\mathbf{B}(\mathbf{r},\omega) = \mu_0\boldsymbol{\mu}(\mathbf{r},\omega)\cdot\mathbf{H}(\mathbf{r},\omega), \tag{2.17}$$

$$\mathbf{j}(\mathbf{r},\omega) = \boldsymbol{\sigma}(\mathbf{r},\omega)\cdot\mathbf{E}(\mathbf{r},\omega). \tag{2.18}$$

For later convenience, we will not distinguish between polarization currents and conduction currents and we will treat both phenomena on the same footing. That is possible by proper definition of the dielectric function [19]

$$\boldsymbol{\varepsilon} + \frac{\mathrm{i}\boldsymbol{\sigma}}{\varepsilon_0\omega} \to \boldsymbol{\varepsilon}(\mathbf{r},\omega). \tag{2.19}$$

Furthermore, in the following we will consider only the non-magnetic materials by setting $\boldsymbol{\mu}(\mathbf{r},\omega) = 1$.

Focusing our attention back to the Maxwell's equations, we will now derive the inhomogeneous wave equation for the electric and magnetic fields. The equations

[1]Fourier transform pairs are related by $f(\mathbf{r},t) = \int f(\mathbf{k},\omega)e^{\mathrm{i}(\mathbf{k}\cdot\mathbf{r}-\omega t)}\mathrm{d}\mathbf{k}\mathrm{d}\omega$.

(2.4) and (2.5) obviously represent a coupled set of equations, each of them being an equation of motion for both, the magnetic induction and the electric field. By applying curl on the equation (2.4), changing order of derivatives on the right hand side and substituting the curl of magnetic induction from equation (2.5), we readily find the inhomogeneous wave equation for the electric field

$$\nabla \times (\nabla \times \mathbf{E}) + \frac{1}{c^2}\frac{\partial^2 \mathbf{E}}{\partial t^2} = -\mu_0 \frac{\partial \mathbf{j}}{\partial t} \tag{2.20}$$

and following the same procedure, we find the inhomogeneous wave equation for the magnetic induction:

$$\nabla \times (\nabla \times \mathbf{B}) + \frac{1}{c^2}\frac{\partial^2 \mathbf{B}}{\partial t^2} = \mu_0 \nabla \times \mathbf{j}. \tag{2.21}$$

The pair of the wave equations (2.20) and (2.21) is fully equivalent to the set of coupled equations (2.4) and (2.5). Formulation of electrodynamics in terms of wave equations is advantageous for independent solution of the electric and the magnetic field evolution and is a starting point for development of the scattering theory based on the volume integral equation.

Now we will show that the solution of the inhomogeneous equations (2.20) and (2.21) can be found in the (time) frequency domain by application of a properly chosen frequency domain dyadic Green's function.

By time Fourier transforming the equations (2.20) and (2.21) we find

$$\nabla \times \nabla \times \mathbf{E}(\mathbf{r}, \omega) - \frac{\omega^2}{c^2}\mathbf{E}(\mathbf{r}, \omega) = \mathrm{i}\mu_0 \omega \mathbf{j}(\mathbf{r}, \omega) \tag{2.22}$$

$$\nabla \times \nabla \times \mathbf{B}(\mathbf{r}, \omega) - \frac{\omega^2}{c^2}\mathbf{B}(\mathbf{r}, \omega) = \mu_0 \nabla \times \mathbf{j}(\mathbf{r}, \omega). \tag{2.23}$$

The electric dyadic Green's function $\mathbf{G}(\mathbf{r}, \mathbf{r}', \omega)$ is defined by equation

$$\nabla \times \nabla \times \mathbf{G}(\mathbf{r}, \mathbf{r}', \omega) - \frac{\omega^2}{c^2}\mathbf{G}(\mathbf{r}, \mathbf{r}', \omega) = \mathbf{I}\delta(\mathbf{r} - \mathbf{r}') \tag{2.24}$$

and specific boundary conditions imposed on the electromagnetic fields. The right hand side of (2.24) consists of a unit dyadic $\mathbf{I}$ multiplied by a delta function $\delta(\mathbf{r} - \mathbf{r}')$ which, in other words, represents an elementary excitation at a point $\mathbf{r}'$ of all possible orientations. Recalling the linearity of the wave equation, we can sum up all the elementary excitations and write the particular solution of (2.20) and (2.21) in the form:

$$\mathbf{E}_{\mathrm{P}}(\mathbf{r}, \omega) = \mathrm{i}\mu_0 \omega \int \mathbf{G}(\mathbf{r}, \mathbf{r}', \omega) \cdot \mathbf{j}(\mathbf{r}', \omega) \mathrm{d}\mathbf{r}', \tag{2.25}$$

$$\mathbf{B}_{\mathrm{P}}(\mathbf{r}, \omega) = \int \nabla \times \mathbf{G}(\mathbf{r}, \mathbf{r}', \omega) \cdot \mathbf{j}(\mathbf{r}', \omega) \mathrm{d}\mathbf{r}'. \tag{2.26}$$

General solution of equations (2.20) and (2.21) is a sum of a homogeneous solution, which represents external fields, and the particular solution:

$$\mathbf{E}(\mathbf{r}, \omega) = \mathbf{E}_{\mathrm{ext}}(\mathbf{r}, \omega) + \mathrm{i}\mu_0 \omega \int \mathbf{G}(\mathbf{r}, \mathbf{r}', \omega) \cdot \mathbf{j}(\mathbf{r}', \omega) \mathrm{d}\mathbf{r}', \tag{2.27}$$

$$\mathbf{B}(\mathbf{r}, \omega) = \mathbf{B}_{\mathrm{ext}}(\mathbf{r}, \omega) + \int \nabla \times \mathbf{G}(\mathbf{r}, \mathbf{r}', \omega) \cdot \mathbf{j}(\mathbf{r}', \omega) \mathrm{d}\mathbf{r}'. \tag{2.28}$$

The sought volume integral equations which self-consistently relate the total electric (magnetic) field at position $\mathbf{r}$ to the total electric (magnetic) field in the rest of the space follow from equations (2.27) and (2.28) by considering dielectric environments free of external charges and currents. In this case, the source current densities in (2.27) and (2.28) are solely the polarization currents, which are related to the total electric field in the frequency domain by

$$\mathbf{j}_{\mathrm{b}}(\mathbf{r},\omega) = -\mathrm{i}\omega\mathbf{P}(\mathbf{r},\omega) = -\mathrm{i}\omega\varepsilon_0\left[\boldsymbol{\varepsilon}(\mathbf{r},\omega) - \mathbf{I}\right]\cdot\mathbf{E}(\mathbf{r},\omega).$$

By substituting into (2.27) and (2.28) we finally obtain the volume integral equations[2]

$$\mathbf{E}(\mathbf{r},\omega) = \mathbf{E}_{\mathrm{ext}}(\mathbf{r},\omega) + \frac{\omega^2}{c^2}\int \mathbf{G}(\mathbf{r},\mathbf{r}',\omega)\cdot\left[\boldsymbol{\varepsilon}(\mathbf{r},\omega) - \mathbf{I}\right]\cdot\mathbf{E}(\mathbf{r},\omega)\mathrm{d}\mathbf{r}', \tag{2.29}$$

$$\mathbf{B}(\mathbf{r},\omega) = \mathbf{B}_{\mathrm{ext}}(\mathbf{r},\omega) - \mathrm{i}\omega\int \nabla\times\mathbf{G}(\mathbf{r},\mathbf{r}',\omega)\cdot\left[\boldsymbol{\varepsilon}(\mathbf{r},\omega) - \mathbf{I}\right]\cdot\mathbf{E}(\mathbf{r},\omega)\mathrm{d}\mathbf{r}'. \tag{2.30}$$

The volume integral equation is a basis for numerical method called discrete dipole approximation (DDA) which, how the name suggests, treats the object as a manifold of point-like dipoles self consistently interacting with each other and with the incident electric field [19].

2.2 Dyadic Green's function

The kernel of the superposition integrals (2.29) and (2.30) represented by the dyadic Green's function plays an important role in the theory of electromagnetic scattering and in the theory of quantum electrodynamics. We will briefly discuss its most important properties and refer the interested reader for detailed discussion elsewhere [19, 34, 35]. The meaning of the dyadic Green's function as an electric field distribution of a point excitation immediately proposes an interpretation of the Green's dyadic as a field of harmonically oscillating electric dipole. In particular, we can find the field distribution of the electric dipole $\mathbf{p}$ radiating in vacuum with help of the dyadic Green's function as follows

$$\mathbf{E}(\mathbf{r},\omega) = \frac{\omega^2}{c^2\varepsilon_0}\mathbf{G}(\mathbf{r},\mathbf{r}',\omega)\cdot\mathbf{p}(\mathbf{r}',\omega),$$

where the Green's dyadic satisfying the Sommerfeld's radiation condition can be found [19, 34][3]

$$\mathbf{G}(\mathbf{r},\mathbf{r}',\omega) = \frac{e^{\mathrm{i}kR}}{4\pi R}\left[\left(1 + \frac{\mathrm{i}kR - 1}{k^2R^2}\right)\mathbf{I} + \frac{3 - 3\mathrm{i}kR - k^2R^2}{k^2R^2}\frac{\mathbf{RR}}{R^2}\right]. \tag{2.31}$$

[2] Throughout the literature, the volume integral equation is often called the Lippmann-Schwinger equation due to the direct analogy with similar formulation of scattering in quantum mechanics, which was developed by B. A. Lippmann and J. Schwinger [32, 33].

[3] Derivation of the Green's dyadic is rather lengthy and can be found in standard texts [19]. One possible strategy consists in calculation of scalar Green's function G for vector and scalar potentials (in Lorenz gauge) and subsequent derivation of relation $\mathbf{G} = \left[\mathbf{I} + \frac{c^2}{\omega^2}\nabla\nabla\right]G$, from which the Green's dyadic follows. Different approach has been proposed by Yaghjian [34], where the Green's dyadic was obtained by direct manipulations with inhomogeneous wave equations – without the necessity of introducing the scalar and vector potentials.

Here $k = \omega/c$ denotes the vacuum wavenumber and $\mathbf{R} = \mathbf{r} - \mathbf{r}'$ is a vector connecting the source position $\mathbf{r}'$ and observation point $\mathbf{r}$. Due to the direct connection with a radiating electric dipole, the Green's dyadic can be also divided into the so called near-field zone ($\mathbf{G}_{\mathrm{NF}}$), which closely resembles fields of electrostatic dipole, the intermediate-field zone ($\mathbf{G}_{\mathrm{IF}}$) and the far-field (radiation) zone ($\mathbf{G}_{\mathrm{FF}}$)

$$\mathbf{G}_{\mathrm{NF}} = \frac{e^{\mathrm{i}kR}}{4\pi R}\frac{1}{k^2R^2}\left[\frac{3\mathbf{RR}}{R^2} - \mathbf{I}\right], \tag{2.32}$$

$$\mathbf{G}_{\mathrm{IF}} = \frac{e^{\mathrm{i}kR}}{4\pi R}\frac{\mathrm{i}}{kR}\left[-\frac{3\mathbf{RR}}{R^2} + \mathbf{I}\right], \tag{2.33}$$

$$\mathbf{G}_{\mathrm{FF}} = \frac{e^{\mathrm{i}kR}}{4\pi R}\left[-\frac{\mathbf{RR}}{R^2} + \mathbf{I}\right]. \tag{2.34}$$

Let us first investigate behaviour of the Green's dyadic in the vicinity of the origin (i.e. the source point). The exponential factor standing in front of the bracket can be expanded for $kR \to 0$ to yield $e^{\mathrm{i}kR} \sim 1 + \mathrm{i}kR + ...$ and by a inspection of the relations (2.32) to (2.34) we discover that the imaginary part of the Green's dyadic is regular, having the value

$$\Im\left\{\mathbf{G}(\mathbf{r}, \mathbf{r}, \omega)\right\} = \frac{k}{6\pi}\mathbf{I}. \tag{2.35}$$

The result in (2.35) therefore represents a self field induced by the radiating dipole at its own position. The self field term, as we will see later, is responsible for radiation damping. The imaginary part of the dyadic Green's function also plays an important role in semi-classical treatment of quantum optical phenomena such as spontaneous emission of atoms or molecules.

The real part of the near-field dyadic (2.32) possesses a strong singularity at the origin and special care must be taken when the Green's function appears as an integral kernel. Different regularization procedures have been employed to deal with the singular behaviour [36]. In 1980 Yaghjian [34] presented a rigorous mathematical treatment leading to a conclusion that the particular solution given in equation (2.25) must be understood as follows

$$\mathbf{E}_{\mathrm{P}}(\mathbf{r}, \omega) = \mathrm{i}\mu_0\omega \int_{\mathrm{reg}} \mathbf{G}(\mathbf{r}, \mathbf{r}', \omega) \cdot \mathbf{j}(\mathbf{r}', \omega)\mathrm{d}\mathbf{r}' + \frac{\mathbf{L} \cdot \mathbf{j}(\mathbf{r}, \omega)}{\mathrm{i}\omega\varepsilon_0}. \tag{2.36}$$

The integration in (2.36) is performed over the regular part of the Green's dyadic where the singularity is excluded by infinitesimal volume of some specific shape. The remaining, singular, part of the integral in (2.25) is now expressed with help of the depolarization dyadic $\mathbf{L}$ which is related to the shape of the exclusion volume via

$$\mathbf{L} = \frac{1}{4\pi}\int_{\partial V_{\mathrm{exc}}} \frac{\mathbf{n}\mathbf{e}_{\mathrm{R}}}{R^2}\mathrm{d}S, \tag{2.37}$$

where the integration is performed over the surface of the exclusion volume with the outer normal $\mathbf{n}$ and $\mathbf{e}_{\mathrm{R}} = \mathbf{R}/R$ being an unit vector pointing in the radial direction. The integral (2.37) does not depend on the exclusion volume size, but solely on its shape. Moreover, it can be shown that the depolarization dyadic $\mathbf{L}$ exhibits the

symmetry property $\mathbf{L} = \mathbf{L}^{\mathrm{T}}$ and its trace fulfils $\mathrm{Tr}\{\mathbf{L}\} = 1$ [34]. The source dyadic has been calculated for various geometries and an elaborate list of its particular forms can be found in reference [34]. The dyadic $\mathbf{L}$ gains a special importance in calculations of a point-like particle polarizability. It is instructive to show how the widely employed quasi-static scattering approach can be recovered from the volume integral equation with help of $\mathbf{L}$.

Consider a point-like particle (a characteristic dimension of the particle meets $l_{\mathrm{char}}k \ll 1$) in vacuum which is excited by an incident electromagnetic plane wave. The volume integral equation for the electric field in the particle position reads

$$\mathbf{E}(\mathbf{r}_{\mathrm{part}}) = \mathbf{E}^{\mathrm{ext}}(\mathbf{r}_{\mathrm{part}}) - [\boldsymbol{\varepsilon}(\mathbf{r}_{\mathrm{part}}) - 1] \cdot \mathbf{L} \cdot \mathbf{E}(\mathbf{r}_{\mathrm{part}}), \tag{2.38}$$

where regular part of the integral was neglected and the electric field at the particle position was extracted from the integral. By expressing the electric field from (2.38) and using

$$\mathbf{p} = V\varepsilon_0 (\boldsymbol{\varepsilon} - 1) \cdot \mathbf{E}(\mathbf{r}_{\mathrm{part}}) = \boldsymbol{\alpha}_0 \cdot \mathbf{E}^{\mathrm{ext}}(\mathbf{r}_{\mathrm{part}}),$$

with V being the particle volume, we can find the quasi-static polarizability for a point-like particle of an arbitrary shape:

$$\alpha_0 = V\varepsilon_0 (\boldsymbol{\varepsilon} - 1) \cdot [1 + (\boldsymbol{\varepsilon} - 1) \cdot \mathbf{L}]^{-1}. \tag{2.39}$$

In particular, for spherical particle, $\mathbf{L}$ is diagonal, having in Cartesian coordinates $L_{xx} = L_{yy} = L_{zz} = 1/3$, and we obtain the well known quasi-static polarizability of a sphere:

$$\alpha_0^{\mathrm{sphere}} = 3V\varepsilon_0 \frac{\varepsilon - 1}{\varepsilon + 2}.$$

During the derivation we disregarded the regular part of the self-integral (2.36) and we validated the approximation by a vanishingly small volume of the particle. However, in practice, the scatter volume has some finite value and the integration over the regular part is essential for correctness of the resultant polarizability, namely, for obtaining a polarizability consistent with the energy conservation law. Retaining the regular part of the integral, we can receive in the first order approximation for the point-like particle:

$$\boldsymbol{\alpha}_{\mathrm{eff}} = \frac{\boldsymbol{\alpha}_0}{1 - \mathrm{i}\frac{k^3}{6\pi\varepsilon_0}\boldsymbol{\alpha}_0}, \tag{2.40}$$

which is valid for point-like particles of an arbitrary shape and is known as the radiation corrected polarizability. The correction for polarizability $\boldsymbol{\alpha}_{\mathrm{eff}}$ can be equivalently obtained from the Abraham-Lorentz formula which follows directly from considerations based on the energy conservation.

So far we have discussed properties of the vacuum Green's dyadic satisfying the radiation boundary conditions. The results obtained in this chapter can be generalized for arbitrary environments (hence, arbitrary boundary conditions) with a little amount of modifications. The singular part of the Green's dyadic remains untouched even in arbitrary environments and the exclusion volume approach remains

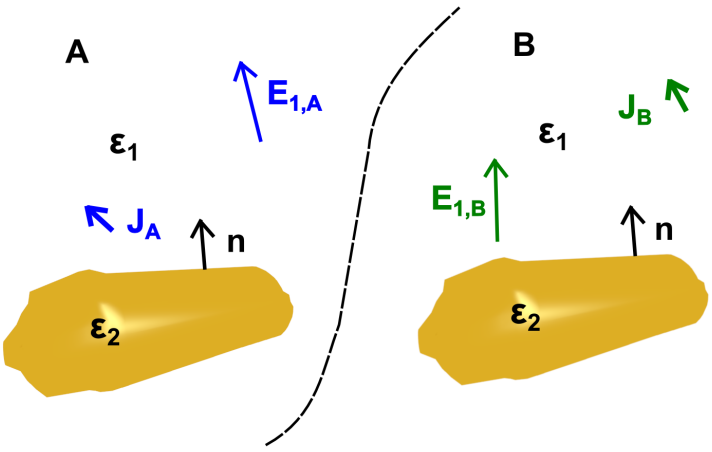

Figure 2.1: The geometry used for derivation of the reciprocity theorem. The external current density $\mathbf{J}_{\mathrm{A(B)}}$ embedded in the medium with permittivity ε_1 excites an electric field $\mathbf{E}_{1,\mathrm{A(B)}}$ around an object with permittivity ε_2 in two different configurations denoted by A and B.

valid. However, the regular part of the Green's function evaluated at the origin will generally contain contribution from the electric field scattered by the environment. The perspective of the scattered fields also immediately proposes a way how to obtain a Green's dyadic for general inhomogeneous environments by means of the vacuum Green's dyadic (2.31) and the volume integral equation (2.29) [19]:

$$\mathbf{G}_{\mathrm{tot}}(\mathbf{r},\mathbf{r}',\omega) = \mathbf{G}(\mathbf{r},\mathbf{r}',\omega) + k^2 \int \mathbf{G}(\mathbf{r},\mathbf{r}'',\omega)\cdot[\varepsilon(\mathbf{r}'',\omega)-\mathbf{I}]\cdot\mathbf{G}_{\mathrm{tot}}(\mathbf{r}'',\mathbf{r}',\omega)\mathrm{d}\mathbf{r}''. \tag{2.41}$$

Equation (2.41) is also called Dyson's equation by analogy with the quantum mechanical Dyson's equation. The equation 2.41 is a general formula for obtaining the total dyadic Green's function.

2.3 Reciprocity theorem

The reciprocity theorem is one of the most important symmetries obtained in the theory of electromagnetic scattering for media which can be described by a symmetric dielectric tensor [37,38]. Let us assume that we have a scatterer which is defined by some permittivity ε_2 embedded in a surrounding medium which can be characterized by permittivity ε_1 (see figure 2.1). Let us further suppose that there are some free currents (sources) in the surrounding medium. Now we consider two situations characterized by two different distributions of free currents. The Maxwell's equations for medium 1 and situation A read:

$$\nabla\times\mathbf{E}_{1,\mathrm{A}} = \mathrm{i}\omega\mu_0\mathbf{H}_{1,\mathrm{A}}, \tag{2.42}$$

$$\nabla\times\mathbf{H}_{1,\mathrm{A}} = -\mathrm{i}\omega\varepsilon_1\mathbf{E}_{1,\mathrm{A}} + \mathbf{J}_{\mathrm{A}}, \tag{2.43}$$

for medium 2:

$$\nabla \times \mathbf{E}_{2,\mathrm{A}} = \mathrm{i}\omega\mu_0\mathbf{H}_{2,\mathrm{A}}, \tag{2.44}$$
$$\nabla \times \mathbf{H}_{2,\mathrm{A}} = -\mathrm{i}\omega\boldsymbol{\varepsilon}_2\mathbf{E}_{2,\mathrm{A}}. \tag{2.45}$$

The fields outside and inside of the scatterer are joined by the standard boundary conditions [19, 39]

$$\mathbf{n} \times (\mathbf{E}_{1,\mathrm{A}} - \mathbf{E}_{2,\mathrm{A}}) = \mathbf{0}, \tag{2.46}$$
$$\mathbf{n} \times (\mathbf{H}_{1,\mathrm{A}} - \mathbf{H}_{2,\mathrm{A}}) = \mathbf{0}, \tag{2.47}$$

where $\mathbf{n}$ denotes the outer normal of the scatterer surface.

The same relations can be equally defined for the situation B by simply changing the index A to B. Let us consider the following identity [38]

$$\begin{aligned}\nabla \cdot (\mathbf{E}_{1,\mathrm{B}} \times \mathbf{H}_{1,\mathrm{A}}) &= \mathbf{H}_{1,\mathrm{A}} \cdot (\nabla \times \mathbf{E}_{1,\mathrm{B}}) - \mathbf{E}_{1,\mathrm{B}} \cdot (\nabla \times \mathbf{H}_{1,\mathrm{A}}) = \\ &= \mathrm{i}\omega\mu_0\mathbf{H}_{1,\mathrm{A}} \cdot \mathbf{H}_{1,\mathrm{B}} + \mathrm{i}\omega\mathbf{E}_{1,\mathrm{B}} \cdot \boldsymbol{\varepsilon}_1 \cdot \mathbf{E}_{1,\mathrm{A}} - \mathbf{E}_{1,\mathrm{B}} \cdot \mathbf{J}_{\mathrm{A}},\end{aligned} \tag{2.48}$$

where the second equality follows directly from the Maxwell's equations. The identity can be similarly stated for the remaining combinations of cross products:

$$\nabla \cdot (\mathbf{E}_{1,\mathrm{A}} \times \mathbf{H}_{1,\mathrm{B}}) = \mathrm{i}\omega\mu_0\mathbf{H}_{1,\mathrm{B}} \cdot \mathbf{H}_{1,\mathrm{A}} + \mathrm{i}\omega\mathbf{E}_{1,\mathrm{A}} \cdot \boldsymbol{\varepsilon}_1 \cdot \mathbf{E}_{1,\mathrm{B}} - \mathbf{E}_{1,\mathrm{A}} \cdot \mathbf{J}_{\mathrm{B}}, \tag{2.49}$$
$$\nabla \cdot (\mathbf{E}_{1,\mathrm{B}} \times \mathbf{H}_{1,\mathrm{A}}) = \mathrm{i}\omega\mu_0\mathbf{H}_{1,\mathrm{A}} \cdot \mathbf{H}_{1,\mathrm{B}} + \mathrm{i}\omega\mathbf{E}_{1,\mathrm{B}} \cdot \boldsymbol{\varepsilon}_1 \cdot \mathbf{E}_{1,\mathrm{A}} - \mathbf{E}_{1,\mathrm{B}} \cdot \mathbf{J}_{\mathrm{A}}, \tag{2.50}$$
$$\nabla \cdot (\mathbf{E}_{2,\mathrm{B}} \times \mathbf{H}_{2,\mathrm{A}}) = \mathrm{i}\omega\mu_0\mathbf{H}_{2,\mathrm{A}} \cdot \mathbf{H}_{2,\mathrm{B}} + \mathrm{i}\omega\mathbf{E}_{2,\mathrm{B}} \cdot \boldsymbol{\varepsilon}_2(\mathbf{r}) \cdot \mathbf{E}_{2,\mathrm{A}}, \tag{2.51}$$
$$\nabla \cdot (\mathbf{E}_{2,\mathrm{A}} \times \mathbf{H}_{2,\mathrm{B}}) = \mathrm{i}\omega\mu_0\mathbf{H}_{2,\mathrm{B}} \cdot \mathbf{H}_{2,\mathrm{A}} + \mathrm{i}\omega\mathbf{E}_{2,\mathrm{A}} \cdot \boldsymbol{\varepsilon}_2(\mathbf{r}) \cdot \mathbf{E}_{2,\mathrm{B}}. \tag{2.52}$$

Respective equations ((2.48) to (2.52)) can be subtracted, using the symmetry of the permittivity, some of the terms disappear, and the result can be (with the help of the Gauss's identity) integrated:

$$\int_{\partial V} (\mathbf{E}_{1,\mathrm{A}} \times \mathbf{H}_{1,\mathrm{B}} - \mathbf{E}_{1,\mathrm{B}} \times \mathbf{H}_{1,\mathrm{A}}) \cdot \mathbf{n}\mathrm{d}S = \int_V (\mathbf{E}_{1,\mathrm{B}} \cdot \mathbf{J}_{\mathrm{A}} - \mathbf{E}_{1,\mathrm{A}} \cdot \mathbf{J}_{\mathrm{B}})\,\mathrm{d}\mathbf{r}, \tag{2.53}$$
$$\int_{\partial V_{scat}} (\mathbf{E}_{2,\mathrm{A}} \times \mathbf{H}_{2,\mathrm{B}} - \mathbf{E}_{2,\mathrm{B}} \times \mathbf{H}_{2,\mathrm{A}}) \cdot \mathbf{n}\mathrm{d}S = 0. \tag{2.54}$$

The surface integral is performed over the scatterer boundary and an infinite sphere in case of the region 1 and over a scatterer surface in case of the region 2 [37]. The integral over the infinite sphere vanishes because in the far field the solutions for electric and magnetic field are related via $\mu_0\mathbf{H} = \mathbf{E}/c$ being constituents of the outgoing spherical electromagnetic wave. The left hand side of the equations (2.53) and (2.54) shows up to be equal after a slight manipulation with use of the boundary conditions. This altogether gives:

$$\int_V (\mathbf{E}_{1,\mathrm{B}} \cdot \mathbf{J}_{\mathrm{A}} - \mathbf{E}_{1,\mathrm{A}} \cdot \mathbf{J}_{\mathrm{B}})\,\mathrm{d}\mathbf{r} = 0, \tag{2.55}$$

which is the celebrated reciprocity theorem of electromagnetism, valid for media which can be characterized by a symmetric dielectric tensor. We will see later that the reciprocity theorem can be exploited in a very elegant way for solution

of otherwise hardly tractable scattering problems. The reciprocity theorem also directly applies for the dyadic Green's function. If we consider the source currents as point-like dipoles of orientation given by an arbitrary unit vectors $\mathbf{e}_\mathrm{A}$ and $\mathbf{e}_\mathrm{B}$, the electric field in (2.55) will be directly given by the Green's dyadic multiplied by the appropriate unit vector and the integration can be performed to yield

$$\mathbf{e}_\mathrm{A} \cdot \mathbf{G}(\mathbf{r}_\mathrm{A}, \mathbf{r}_\mathrm{B}) \cdot \mathbf{e}_\mathrm{B} = \mathbf{e}_\mathrm{B} \cdot \mathbf{G}(\mathbf{r}_\mathrm{B}, \mathbf{r}_\mathrm{A}) \cdot \mathbf{e}_\mathrm{A}. \tag{2.56}$$

Since the vectors $\mathbf{e}_1$ and $\mathbf{e}_2$ are arbitrary, we obtain [38]

$$\mathbf{G}(\mathbf{r}_\mathrm{A}, \mathbf{r}_\mathrm{B}) = \mathbf{G}^\tau(\mathbf{r}_\mathrm{B}, \mathbf{r}_\mathrm{A}), \tag{2.57}$$

where τ denotes the transposition. The symmetry property of dyadic Green's function (2.57) states that the energy transfer from dipole A to dipole B equals to the energy transfer from dipole B to dipole A. The reciprocity theorem in either the general form (2.55) or (2.57) is widely exploited in the theory of near-field interaction.

3 | Interaction of s-SNOM probe with metallic structures

Infrared antennas gained a large significance in the near-field optics because of their ability to squeeze the electromagnetic field from the infrared part of the spectrum to the nanometer-sized space. Thanks to this, they provide a large near-field enhancement and open the path to a variety of applications, among others, to the surface enhanced infrared spectroscopy. Mapping of their near-field properties therefore gained a significant importance for development of state-of-the-art applications based on engineering of metallic nano- and micro structures.

A wide spectrum of methods which are able to access the metallic structure near-field properties has been developed so far. Among others, the high resolution electron energy loss spectroscopy (HREELS) succeeded in mapping of the quantity closely related to the local density of electromagnetic states (LDOS) [40–42].

A different approach, often called the aperture scanning near-field optical microscopy (a-SNOM) [43], which utilizes various kinds of aperture probes, has also proven useful in the near-field detection. In a-SNOM, the aperture probe can either deliver the electromagnetic field into the antenna's close proximity, exciting the antenna, which radiation is subsequently collected in the far field, or directly collect the antenna electromagnetic near-field excited by an external (macroscopic) illumination [44]. The a-SNOM approach is mostly suitable for detection of light in the visible part of the electromagnetic spectrum, since the light wavelength is short enough to be squeezed into the tiny aperture ($\sim$50 nm) of the metal coated probe (usually tapered fibre tip). Thanks to proceeding development in nano-technology, the drawback of the low frequency cut-off can be in principle overcome by modification of the a-SNOM probe into the form of a coaxial waveguide and even the infrared radiation could be in principle handled by means of the tapered fibre tips, while retaining the nanometer resolution of the microscope.

In this work we will focus on a technique called the scattering type scanning near-field optical microscopy (s-SNOM) [45, 46]. S-SNOM utilizes an oscillating apertureless probe to access the sample near-fields induced by an external illumination and scatter them into the far-field where they are detected. Oscillation of the tip is exploited for modulation of the scattered signal which is demodulated with the help of a sophisticated interferometric set-up [47]. Since the scattered and demodulated signal originates merely from an interaction of the sharp probing tip (usually an AFM tip) and the sample, resolution of the s-SNOM is predominantly given by the tip geometrical size regardless of the incident light wavelength.

The most challenging task for the near-field microscopy remains a nano-resolution

characterization of a full polarization state of the electromagnetic antenna near-field [48, 49]. S-SNOM reaches the nano-resolution requirements even in infrared region and enables the phase-sensitive detection. The possibility of polarization resolved measurements makes the s-SNOM a perfect candidate for detection of the near-field polarization state. We will show in this chapter that the exact relationship between the near-field polarization state and the actual detected polarization-resolved signal is not fairly straightforward and that a special care must be taken for the signal interpretation. A simple analytical formula connecting the antenna near-field polarization state and the detected signal will be provided for a configuration with a weakly scattering tip. Theoretical predictions rising from the analytical model will be compared to actual experimental results based on a single and dimer antenna s-SNOM measurements.

3.1 Principle of s-SNOM

S-SNOM is in principle an usual AFM device equipped with an additional optical apparatus for laser illumination and simultaneous signal detection and processing [45, 47]. The tip used for the s-SNOM is also commonly found in conventional AFM devices. The tip can either interact weakly with the sample and provide information about the sample unperturbed near-fields, or offer a strong near-field interaction and enhancement of the scattered signal, conveniently utilized for detection of the sample material properties [45, 50–52]. The core of the phase resolved detection obtained by s-SNOM resides in interferometric processing of the signal scattered by the tip [47].

The processing of measured signal aims on successful separation of the signal originating from the near-field interaction of the tip with a sample and a signal coming from background contributions. These background contributions contain reflections of incident laser beam directly from the sample, from the surrounding substrate or from the oscillating cantilever of the AFM tip. The background usually strongly overwhelms the desired tip-sample interaction signal and must be therefore excluded from the detection. Possible experimental solution exploits the oscillations of the AFM cantilever on its well defined eigenfrequency and utilizes an interferometric detection scheme.

In recent years, a new trend appeared in the field of near-field microscopy operating in the visible spectrum. The novel approach profits from a phenomenon of the metal photo-luminescence, where the tip acts as a nanometer-sized stable source of a luminescent radiation [53]. The background contributions are therefore spectrally shifted with respect to the incident and elastically scattered light which allows for a simple background elimination without use of any complex detection set-up. We will refer to the promising technique of the metal-luminescent s-SNOM in the next chapter. The solution relying on the luminescence is, however, restricted to the region of a strong metal luminescence and is not capable of spectroscopic measurements. Additionally, a strong near-field enhancement of the detected structure is vital for sufficient signal yield in the gold-luminescence microscopy. In practice, the interferometric detection keeps its irreplaceable position in the field of scanning near-field optical microscopy.

A variety of interferometric detection techniques has been developed, including the homodyne, the heterodyne or the pseudo-heterodyne detection [54]. The field of the near-field detection is still a hot topic for researchers in nano-optics and plasmonics. There is still an ongoing development in the area of the detection methods which recently led to the invention of a novel holographic near-field detection scheme [55]. We will briefly describe the three most usual ones which can be commonly found in recent experimental equipment.

The homodyne detection belongs to one of the simplest implementations of the interferometric signal detection techniques, relying on interference between the modulated signal scattered by the tip and the background contribution itself [56]. A more technically complex detection scheme, the heterodyne detection technique, utilizes an interference of the measured signal with a reference beam of slightly different frequency, exploiting usually the crystal of the acousto-optical modulator. The resulting interference pattern is varying in time with frequency equal to the frequency difference of the reference and the measured signal. Presence of the crystal in the optical path sets a constraint for spectroscopic measurements performed using the heterodyne demodulation. An alternative method to the heterodyne demodulation, overcoming the spectral dispersion of the acousto-optical modulator, is the pseudo-heterodyne demodulation. Here an oscillating dispersion-less mirror is placed into the reference branch of a Michelson interferometer. In the following text, we will focus on description of the last mentioned, pseudo-heterodyne detection scheme principle.

Schematics of the Michelson interferometer used for the pseudo-heterodyne detection is depicted in Figure 3.1 [57]. The laser light entering the interferometer is divided into two beams – one entering the detection branch and the other one propagating to the reference branch. The reference branch is equipped with a mirror attached to a piesoelectric crystal, oscillating with a given amplitude on a precisely defined frequency M. As it will be shown later, the oscillation amplitude of the mirror must be chosen properly in order to achieve the phase resolved results directly. The s-SNOM tip oscillating at the eigenfrequency Ω is placed into the detection branch, scattering the incident light towards the detector. Both beams going through the interferometer finally meet at the detector where they interfere. The measured interference signal is further demodulated with the help of a lock-in amplifier at frequencies equal to the higher harmonic frequency of the cantilever oscillation, shifted by a multiple of the mirror frequency. In the most common set-up, the signal is demodulated at frequencies $n\Omega + M$ and $n\Omega + 2M$ (here n is an integer representing the order of a higher harmonic frequency).

In the language of mathematics, the signal entering the detector can be described by means of interference of two plane waves. The beam reflected from the oscillating mirror represents a phase modulated plane wave with a complex amplitude

$$E_{\mathrm{R}} = \rho \exp\left[\mathrm{i}\gamma \sin(Mt) + \mathrm{i}\psi\right], \tag{3.1}$$

where $\gamma = 2\pi A/\lambda$ is the phase modulation amplitude with A being the physical amplitude of the mirror oscillation, λ being the wavelength of the laser light, ψ is a constant phase shift related to adjustment of the interferometer. The signal plane

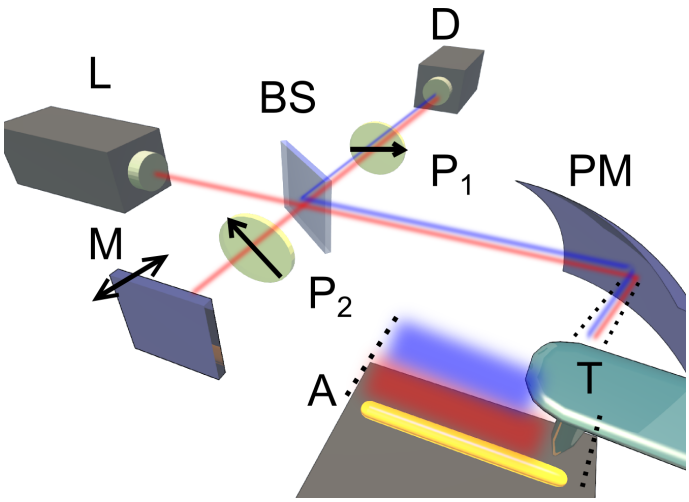

Figure 3.1: Experimental set-up of back scattering s-SNOM utilizing pseudo-heterodyne detection scheme adapted from [57]. Laser beam emitted by source (L) is passing through a beam splitter (BS) and is entering the two branches of the Michelson interferometer. In one branch, the laser is reflected by a parabolic mirror (PM) to the AFM device with the oscillating tip (T) (frequency Ω), where the sample antenna (A) is situated. The tip scatters the light back towards the beam-splitter and the detector (D). The second branch (reference branch) is equipped with a mirror (M) oscillating on a frequency M. The resulting signal coming to the photodetector is therefore given by interference of the reference beam and the scattered light. The signal is demodulated by a lock-in amplifier on frequencies $n\Omega + M$ a $n\Omega + 2M$. For purposes of polarization resolved measurements, two polarizers (P_1 and P_2) are inserted into the interferometer.

wave scattered by the tip will undergo amplitude modulation

$$E_{\mathrm{S}} = \sum_{n=-\infty}^{\infty} \tau_n \exp(\mathrm{i}n\Omega t). \tag{3.2}$$

The detected signal is given by interference of the reference beam E_{R} reflected from the oscillating mirror and the beam scattered by the tip E_{S}

$$I = (E_{\mathrm{S}} + E_{\mathrm{R}})\,(E_{\mathrm{S}} + E_{\mathrm{R}})^{*}\,, \tag{3.3}$$

where $*$ denotes complex conjugate. It can be straightforwardly shown that the signal modulated on the frequency $(n\Omega + mM)$ comes solely from the contribution

$$I_{\mathrm{MIXED}} = E_{\mathrm{S}}E_{\mathrm{R}}^{*} + E_{\mathrm{S}}^{*}E_{\mathrm{R}}, \tag{3.4}$$

which can be rewritten as

$$I_{\mathrm{MIXED}} = 2\left(\Re\left\{E_{\mathrm{R}}\right\}\Re\left\{E_{\mathrm{S}}\right\} + \Im\left\{E_{\mathrm{R}}\right\}\Im\left\{E_{\mathrm{S}}\right\}\right), \tag{3.5}$$

where $\Re$ ($\Im$) denotes real (imaginary) part of a complex function. The complex Fourier series representing the modulated signal can be decomposed into the real and the imaginary part

$$\Re\{E_{\mathrm{S}}\} = \tau_0' + \sum_{n=1}^{\infty}\left\{\left(\tau_n' + \tau_{-n}'\right)\cos(n\Omega t) - \left(\tau_n'' - \tau_{-n}''\right)\sin(n\Omega t)\right\}, \tag{3.6}$$

$$\Im\{E_{\mathrm{S}}\} = \tau_0'' + \sum_{n=1}^{\infty}\left\{\left(\tau_n'' + \tau_{-n}''\right)\cos(n\Omega t) - \left(\tau_n' - \tau_{-n}'\right)\sin(n\Omega t)\right\}. \tag{3.7}$$

The complex function describing the light reflected from the oscillating mirror can be expanded into a series [47]

$$E_{\mathrm{R}} = \exp(\mathrm{i}\psi)\sum_{m=-\infty}^{\infty}\mathrm{J}_m(\gamma)\exp(\mathrm{i}mMt) \tag{3.8}$$

or equivalently

$$\begin{aligned} E_{\mathrm{R}} = \exp(\mathrm{i}\psi)\Bigg\{&\rho\mathrm{J}_0(\gamma) + 2\rho\sum_{k=1}^{\infty}\mathrm{J}_{2k}(\gamma)\cos(2kMt) + \\ &+\mathrm{i}2\rho\sum_{k=0}^{\infty}\mathrm{J}_{2k+1}(\gamma)\sin[(2k+1)Mt]\Bigg\}, \end{aligned} \tag{3.9}$$

where J_n is the Bessel function of the first kind and of order n. It is easy to show that the function (3.9) can be separated into the real and the imaginary part as follows

$$\begin{aligned} \Re\{E_{\mathrm{R}}\} = \cos\psi&\left\{\rho\mathrm{J}_0(\gamma) + 2\rho\sum_{k=1}^{\infty}\mathrm{J}_{2k}(\gamma)\cos(2kMt)\right\} - \\ &-\sin\psi\left\{2\rho\sum_{k=0}^{\infty}\mathrm{J}_{2k+1}(\gamma)\sin[(2k+1)Mt]\right\}, \end{aligned} \tag{3.10}$$

$$\begin{aligned} \Im\{E_{\mathrm{R}}\} = \sin\psi&\left\{\rho\mathrm{J}_0(\gamma) + 2\rho\sum_{k=1}^{\infty}\mathrm{J}_{2k}(\gamma)\cos(2kMt)\right\} + \\ &+\cos\psi\left\{2\rho\sum_{k=0}^{\infty}\mathrm{J}_{2k+1}(\gamma)\sin[(2k+1)Mt]\right\}. \end{aligned} \tag{3.11}$$

Thus, for given side bands of n-th harmonic of the tip oscillation, (3.5) together with the decomposition of the functions into their real and the imaginary parts (3.6), (3.7), (3.10) and (3.11) leads to:

$$\begin{aligned} I_{n;2k,2l+1} = &(\cos\psi E'_n + \sin\psi E''_n)\, 2\rho \mathrm{J}_{2k}(\gamma)\cos(n\Omega t)\cos(2kMt) + \\ &+ (-\sin\psi E'_n + \cos\psi E''_n)\, 2\rho \mathrm{J}_{2l+1}(\gamma)\cos(n\Omega t)\cos[(2l+1)Mt], \end{aligned} \tag{3.12}$$

where k and l are integers. It was assumed, without loss of generality[1], that the scattered signal is an even function of time and the notation $E_n = \tau_n + \tau_{-n}$ was used. Using the goniometric relations

$$\begin{aligned} \sin\alpha\cos\beta &= \frac{1}{2}\left[\sin(\alpha+\beta) - \sin(\alpha-\beta)\right], \\ \cos\alpha\cos\beta &= \frac{1}{2}\left[\cos(\alpha+\beta) + \cos(\alpha-\beta)\right], \end{aligned}$$

it can be shown that the coefficients standing in front of the respective products of the goniometric functions are proportional to the coefficients of sines (cosines) with the argument being sum and difference of the respective frequencies.

The resulting expression also explains the necessity to adjust the amplitude of the mirror oscillations in the reference branch properly. If $\gamma = 2.63$ is set, the equality of the Bessel function values $\mathrm{J}_1(2.63) = \mathrm{J}_2(2.63)$ is established. Hence, if the signal on frequencies $n\Omega + M$ and $n\Omega + 2M$ is detected, the disproportion caused by the presence of the Bessel functions in the coefficients of respective higher harmonic side bands disappears.

The constant phase shift ψ caused by the interferometer alignment contributes to the resulting signal only as an angle of constant phase shift, here represented by components of a rotation matrix in the complex plane. The phase shift ψ can therefore be safely disregarded in relative measurements.

Let us sum up the obtained results. By measurement of amplitudes on frequencies corresponding to higher harmonic frequency of cantilever plus M or $2M$, it is possible to reconstruct both the real E'_n and the imaginary part E''_n of the signal and therefore also the signal amplitude $|E_n|$ and the phase $\varphi = \arg(E_n)$

$$E'_n \propto I(n\Omega + 2M), \tag{3.13}$$

$$E''_n \propto I(n\Omega + M), \tag{3.14}$$

$$\varphi \propto \arctan\left(\frac{E''_n}{E'_n}\right), \tag{3.15}$$

$$|E_n| \propto \sqrt{E'^2_n + E''^2_n}. \tag{3.16}$$

We are therefore able to access the phase information on the local field distribution. The demodulation procedure however provides only information on the higher order coefficients of the scattered signal. In order to clarify the physical essence of the higher order coefficients, we have to return to the actual experimental set-up, where the tip is relatively slowly scanned above the sample in the lateral direction,

[1] Any constant phase shift can be comprised in the variable ψ of the reference beam.

meanwhile oscillating at a high frequency Ω in the vertical direction. The time dependence rising from the lateral movement of the tip is slow enough with respect to its fast vertical oscillations, so that the tip can be treated as a vertically oscillating object, which is subsequently positioned into different lateral positions of the sample.

A general function expressing the scattered signal $E_{\mathrm{S}}(\mathbf{r}_{\parallel}, z)$ must be therefore dependent on a lateral position of the tip $\mathbf{r}_{\parallel}$ and a vertical time dependent position $z(t)$. The function can be expanded in the vertical direction about some given equilibrium point z_0 into the Taylor series:

$$E_{\mathrm{S}}(\mathbf{r}_{\parallel}, z) = \sum_{n=0}^{\infty} \frac{1}{n!} E_S^{(n)}(z_0) \Delta z^n.$$

Let the displacement from the position z_0 have a time dependence representing the harmonic oscillations of the tip with an amplitude u:

$$\Delta z(t) = u \cos(\Omega t). \tag{3.17}$$

The time dependence can be inserted into the original Taylor series and powers of goniometric functions can be expressed in terms of goniometric functions of argument multiples. This is a straightforward way of how to determine the coefficients standing in front of the respective higher harmonic terms in the time dependent Fourier series (3.2). The scattered signal can thus be expressed as:

$$\begin{aligned}
E_{\mathrm{S}}(\mathbf{r}_{\parallel}, t) &= \sum_{n=0}^{\infty} \frac{1}{n!} E_{\mathrm{S}}^{(n)}(\mathbf{r}_{\parallel}, z_0) u^n \cos^n(\Omega t) = \\
&= E_{\mathrm{S}}^{(0)}(\mathbf{r}_{\parallel}, z_0) + \left[u E_{\mathrm{S}}^{(1)}(\mathbf{r}_{\parallel}, z_0) + ... \right] \cos(\Omega t) + \\
&+ \left[\frac{u^2 E_{\mathrm{S}}^{(2)}(\mathbf{r}_{\parallel}, z_0)}{4} + \frac{u^4 E_{\mathrm{S}}^{(4)}(\mathbf{r}_{\parallel}, z_0)}{48} + ... \right] \cos(2\Omega t) + \\
&+ \left[\frac{u^3 E_{\mathrm{S}}^{(3)}(\mathbf{r}_{\parallel}, z_0)}{24} + \frac{u^5 E_{\mathrm{S}}^{(5)}(\mathbf{r}_{\parallel}, z_0)}{384} + ... \right] \cos(3\Omega t) + \\
&+ \left[\frac{u^4 E_{\mathrm{S}}^{(4)}(\mathbf{r}_{\parallel}, z_0)}{192} + \frac{u^6 E_{\mathrm{S}}^{(6)}(\mathbf{r}_{\parallel}, z_0)}{3840} + ... \right] \cos(4\Omega t) + ...,
\end{aligned}$$

where the higher order derivative terms of the coefficients can be neglected. Coefficients of higher harmonic terms can therefore be interpreted for small amplitudes of the tip oscillation as spatial derivatives of higher orders, evaluated at the equilibrium position of the tip. That interpretation also explains decreasing magnitude of the higher harmonic coefficients. From the practical point of view this means that the signal is usually demodulated on the third or the fourth harmonic frequency of the tip. Lower orders of demodulation usually insufficiently remove influence of the background signal, rising from the tip direct reflections and experimental imperfections. On the other hand, it is almost impossible to measure higher order coefficients, because their magnitude reaches the experimental noise level.

3.2 Infrared antenna characterization

So far, we have briefly described the basic s-SNOM signal detection and processing principles. We concluded that the final measured signal reflects a mutual interaction of the tip and the measured object in some, yet unspecified, way. A general description of the interaction is a rather challenging issue which can be only hardly treated in general. First of all, we have to distinguish between the two different operational modes of s-SNOM. When material properties and spectroscopic information of the sample are required, strong scattering tips (usually metallic) are used. They interact with the sample via their image charge, providing therefore information about material properties of the sample. However, when the access to the near-field distribution around a sample (for example a nanoantenna) is desired, a weakly-scattering tip is usually utilized to access the near-field without distortion.

We will stick here to description of the latter mentioned, weak scattering detection mode. Description of the s-SNOM signal yields a direct scattering problem determined by the pair of scatterers: the tip (T) and the sample antenna (A). The mutual scattering process can be in the most general case described by means of the volume integral equation for electric field (2.29):

$$\mathbf{E}(\mathbf{r}) = \mathbf{E}^{\mathrm{I}}(\mathbf{r}) + k^2 \int \mathbf{G}(\mathbf{r}, \mathbf{r}') \cdot \boldsymbol{\chi}(\mathbf{r}') \cdot \mathbf{E}(\mathbf{r}') \mathrm{d}\mathbf{r}'. \tag{3.18}$$

Here $\mathbf{E}^{\mathrm{I}}$ is the incident electric field and $\boldsymbol{\chi}(\mathbf{r}') = \boldsymbol{\varepsilon}(\mathbf{r}') - 1$ is the spatially varying susceptibility of the dielectric environment which, in our case, is fully characterized by positions and material of the pair of the scatterers. We can formally split the integration in (3.18) into integration over the two distinct objects, the antenna and the tip:

$$\mathbf{E}(\mathbf{r}_{\mathrm{A}}) = \mathbf{E}^{\mathrm{I}}(\mathbf{r}_{\mathrm{A}}) + k^2 \mathbf{G}^{\mathrm{T}\to\mathrm{A}} \mathbf{E}(\mathbf{r}_{\mathrm{T}}) + k^2 \mathbf{G}^{\mathrm{A}\to\mathrm{A}} \mathbf{E}(\mathbf{r}_{\mathrm{A}}), \tag{3.19}$$

$$\mathbf{E}(\mathbf{r}_{\mathrm{T}}) = \mathbf{E}^{\mathrm{I}}(\mathbf{r}_{\mathrm{T}}) + k^2 \mathbf{G}^{\mathrm{A}\to\mathrm{T}} \mathbf{E}(\mathbf{r}_{\mathrm{A}}) + k^2 \mathbf{G}^{\mathrm{T}\to\mathrm{T}} \mathbf{E}(\mathbf{r}_{T}), \tag{3.20}$$

where the subscripts and superscripts T (A) denote the event taking place on the tip (antenna) and where the Green's scattering integral operator $\mathbf{G}^{\mathbf{r}'\to\mathbf{r}}\mathbf{E}(\mathbf{r}') \equiv \int \mathbf{G}(\mathbf{r}, \mathbf{r}') \cdot \boldsymbol{\chi}(\mathbf{r}') \cdot \mathbf{E}(\mathbf{r}')\mathrm{d}\mathbf{r}'$ has been introduced. Now we can calculate the field in the position of the antenna and in the position of the tip respectively. This might be formally done by subtracting the self term $k^2 \mathbf{G}^{\mathrm{A(T)}\to\mathrm{A(T)}} \mathbf{E}(\mathbf{r}_{\mathrm{A(T)}})$ and multiplying the equations (3.19) and (3.20) by an inverse operator from the left:

$$\mathbf{E}(\mathbf{r}_{\mathrm{A(T)}}) = \left[\mathbf{I} - k^2 \mathbf{G}^{\mathrm{A(T)}\to\mathrm{A(T)}}\right]^{-1} \left[\mathbf{E}^{\mathrm{I}}(\mathbf{r}_{\mathrm{A(T)}}) + k^2 \mathbf{G}^{\mathrm{T(A)}\to\mathrm{A(T)}} \mathbf{E}(\mathbf{r}_{\mathrm{T(A)}})\right]. \tag{3.21}$$

Here we condensed the equations for the antenna and the tip into a single expression, because both of them are formally identical. Now, substituting the electric field $\mathbf{E}(\mathbf{r}_{\mathrm{T(A)}})$ into the expression for the electric field $\mathbf{E}(\mathbf{r}_{\mathrm{A(T)}})$ yields the set of equations

$$\begin{aligned} \mathbf{E}(\mathbf{r}_{\mathrm{A(T)}}) = &\left[\mathbf{I} - k^4 \mathbf{S}_{\mathrm{A(T)}}{}^{-1} \mathbf{G}^{\mathrm{T(A)}\to\mathrm{A(T)}} \mathbf{S}_{\mathrm{T(A)}}{}^{-1} \mathbf{G}^{\mathrm{A(T)}\to\mathrm{T(A)}}\right]^{-1} \times \\ &\times \left[\mathbf{S}_{\mathrm{A(T)}}{}^{-1} \mathbf{E}^{\mathrm{I}}(\mathbf{r}_{\mathrm{A(T)}}) + k^2 \mathbf{S}_{\mathrm{A(T)}}{}^{-1} \mathbf{G}^{\mathrm{T(A)}\to\mathrm{A(T)}} \mathbf{S}_{\mathrm{T(A)}}{}^{-1} \mathbf{E}^{\mathrm{I}}(\mathbf{r}_{\mathrm{T(A)}})\right], \end{aligned} \tag{3.22}$$

where the operator $\mathbf{S}_{\mathrm{A(T)}} = \mathbf{I} - k^2\mathbf{G}^{\mathrm{A(T)}\to\mathrm{A(T)}}$ was defined. The inverse operator in brackets which appears at the beginning of the right hand side of (3.22) can be expanded into a Taylor series using an assumption that the operator norm of $k^4{\mathbf{S}_{\mathrm{A(T)}}}^{-1}\mathbf{G}^{\mathrm{T(A)}\to\mathrm{A(T)}}{\mathbf{S}_{\mathrm{T(A)}}}^{-1}\mathbf{G}^{\mathrm{A(T)}\to\mathrm{T(A)}}$ is less than unity [58]. This assumption can be validated by considering that the norm of the operator should roughly correspond to the product of the field enhancements of the antenna and the tip in the respective positions. An estimation considering an equivalent tip dipole represented by a silicon sphere with the diameter of the order of $\sim (10-100)$ nm and the antenna field enhancement of the order ~ 10 yields a value of the norm[2] $\sim 10^{-2} - 10^{-1}$, hence, relatively close to the limit of the expansion validity.

The Taylor series expansion is a key step for our further analysis. Its validity can be alternatively considered as a criterion for distinction between the strong interaction mode and the weak interaction mode. By definition, if the weak interaction mode occurs, the Taylor expansion of (3.22) is possible and the following discussion and signal interpretation applies. For the strong interaction regime, the results derived further on in this chapter cease validity and some different approach must be employed. In practice, both of the two regimes are found and special care must be taken for interpretation of particular measurements.

After expanding the expressions (3.22) into the Taylor series in accordance with the weak interaction regime, the appropriate scattering operator which projects the fields to the infinity can be applied. The total scattered far-field $\mathbf{E}$ can be accordingly expressed as a coherent sum of all the contributions of the different multiple scattering events as [59, 60]:

$$\mathbf{E} = \underbrace{\mathbf{F}^{\mathrm{A}}\mathbf{E}^{\mathrm{I}}}_{\mathbf{E}^{\mathrm{A}}} + \underbrace{\mathbf{F}^{\mathrm{T}}\mathbf{E}^{\mathrm{I}}}_{\mathbf{E}^{\mathrm{T}}} + \underbrace{\mathbf{F}^{\mathrm{A}}\mathbf{F}^{\mathrm{T}}\mathbf{E}^{\mathrm{I}}}_{\mathbf{E}^{\mathrm{AT}}} + \underbrace{\mathbf{F}^{\mathrm{T}}\mathbf{F}^{\mathrm{A}}\mathbf{E}^{\mathrm{I}}}_{\mathbf{E}^{\mathrm{TA}}} + \underbrace{\mathbf{F}^{\mathrm{A}}\mathbf{F}^{\mathrm{T}}\mathbf{F}^{\mathrm{A}}\mathbf{E}^{\mathrm{I}}}_{\mathbf{E}^{\mathrm{ATA}}} + \ldots, \tag{3.23}$$

where $\mathbf{E}^{\mathrm{I}}$ is the incident light and $\mathbf{F}^{\mathrm{T(A)}}$ is the scattering operator of the tip (antenna) relating the field distribution in the tip (antenna) surrounding to external fields evaluated at the position of the tip (antenna). One should notice that the scattering operators do not include only the Green's scattering operator $\mathbf{G}$ but also the self interaction operator $\mathbf{S}$. This implies that the scattering has to be calculated with use of the complete scattering operator; that is the operator which includes all the multiple scattering events taking place on a single object. By comparison with (3.22), the operator $\mathbf{F}^{\mathrm{T(A)}}$ has to be defined as:

$$\begin{aligned}\mathbf{F}^{\mathrm{A(T)}}\mathbf{E} &\equiv k^2\mathbf{G}^{\mathrm{A(T)}\to\mathbf{r}}{\mathbf{S}_{\mathrm{A(T)}}}^{-1}\mathbf{E} = \\ &= k^2\int_{\mathrm{A(T)}}\mathbf{G}(\mathbf{r},\mathbf{r}')\cdot\boldsymbol{\chi}_{\mathrm{A(T)}}\cdot\left[\mathbf{E}(\mathbf{r}') - k^2\int_{\mathrm{A(T)}}\mathbf{G}(\mathbf{r}',\mathbf{r}'')\cdot\boldsymbol{\chi}_{\mathrm{A(T)}}\cdot\mathbf{E}(\mathbf{r}'')\mathrm{d}\mathbf{r}''\right]^{-1}\mathrm{d}\mathbf{r}'.\end{aligned} \tag{3.24}$$

Where the integration is performed over the volume of the respective scatterer and the $[]^{-1}$ denotes the operator inverse. At this stage, it is suitable to shed light on the definition 3.24 by considering a scattering taking place on point-like objects. We

[2]The effective distance of the tip to the antenna was taken as a half of the antenna length. The estimation very roughly follows from consideration of two point-like objects interacting by their scattered fields.

can write the total scattering operator for the point-like object by means of the total radiation corrected polarizability 2.40 and the Green's dyadic:

$$\mathbf{F}^{\mathrm{A(T)}}\mathbf{E} = \frac{k^2}{\varepsilon_0}\mathbf{G}(\mathbf{r},\mathbf{r}')\cdot\boldsymbol{\alpha}\cdot\mathbf{E}(\mathbf{r}'),$$

which is nothing else but the field radiated by a dipole $\mathbf{p} = \boldsymbol{\alpha}\cdot\mathbf{E}$. In case of spatially extended objects, however, we must consider the spatial field distribution throughout the antenna and execute the integration over the antenna volume, which is the actual meaning of the definition (3.24).

By now we have derived the scattered field in terms of an infinite operator series of multiple scattering events taking place alternately on the tip and the antenna (3.23). The individual terms in series (3.23) can therefore be interpreted as scattering events of multiple orders. Terms denoted by $\mathbf{E}^{\mathrm{A}}$ and $\mathbf{E}^{\mathrm{T}}$ represent a direct scattering of the incident light from the antenna and the tip. We can also define two double scattering events. First, when the incident radiation interacts with the antenna, inducing an antenna scattered field which subsequently interacts with the tip, re-radiating the electromagnetic field back towards the detector ($\mathbf{E}^{\mathrm{TA}}$), and second, when the scattering event takes place first on the tip and subsequently on the antenna ($\mathbf{E}^{\mathrm{AT}}$) in a similar way as described above. By following the same logic, we can continue in definition of multiple scattering events of higher orders, but because we have supposed that the tip scatters the light only weakly, higher order contributions from the tip will become negligible with respect to the scattering events, where the tip participates mostly once [59]. We can therefore neglect these higher order tip scattering events and obtain the truncated scattering series:

$$\mathbf{E} = \mathbf{E}^{\mathrm{A}} + \mathbf{E}^{\mathrm{T}} + \mathbf{E}^{\mathrm{AT}} + \mathbf{E}^{\mathrm{TA}} + \mathbf{E}^{\mathrm{ATA}}. \tag{3.25}$$

The multiple scattering expressed by equation (3.25) is schematically depicted in Figure 3.2. The truncated series (3.25) basically represents the signal which arrives to the detector from the detection branch of the s-SNOM interferometric set-up. We realize that only terms including the mutual interaction of the tip and of the antenna will be anharmonically modulated, contributing thus to the final measured higher harmonic signal. This leads us to the conclusion that it is fully sufficient for the detected signal to consider only the three interaction terms of (3.25), and we write

$$\mathbf{E} \sim \mathbf{E}^{\mathrm{AT}} + \mathbf{E}^{\mathrm{TA}} + \mathbf{E}^{\mathrm{ATA}}, \tag{3.26}$$

which is our final formula for signal detected by s-SNOM equipped with a weakly scattering tip.

3.2.1 Signal interpretation

Our main goal is to unravel the relationship of the signal with the local antenna components. So far, we are only able to obtain a phase resolved signal, which is proportional to the antenna scattering properties by (3.26). To obtain an information on the electromagnetic near-field components of the antenna, one has to insert

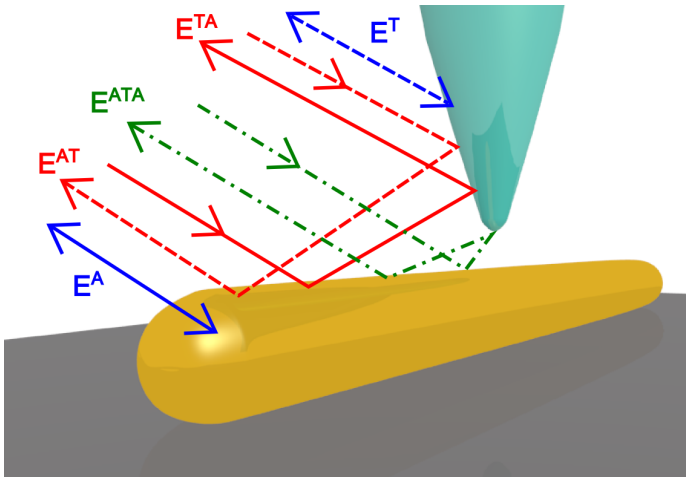

Figure 3.2: The gold antenna and the weakly scattering silicon tip are illuminated by external coherent source. The field scattered towards the detector can be obtained as a coherent sum of multiple scattering events, here schematically denoted by coloured arrows, up to the first order of a scattering on the tip. Higher order scattering events can be neglected for a weakly scattering tip.

a polarizer into the optical path between the antenna-tip system and the detector. The polarizer is usually set for detecting one of the orthogonal light polarizations – the light polarized perpendicularly to the plane of incidence, denoted by S, and the light polarized parallel to the plane of incidence, denoted by P.

As we pointed out in the last section, the signal scattered to the detector from the antenna-tip system is proportional to the multiple scattering events up to the first order of scattering taking place on the tip. This scattering process can alternatively be viewed from a slightly different perspective. Let us focus solely on a scattering of the incident light from the tip. Instead of the vacuum Green's function (or more generally the Green's function of the bare substrate) $\mathbf{G}$, we use now a Green's function $\boldsymbol{\mathcal{G}}$ of the total system, where the antenna becomes an integral part of the surrounding environment. The main idea of the alternative approach consists in the following consideration: the tip is inserted into the electromagnetic field produced by some external source, it is polarized by the external field and therefore it becomes a source of radiation. Since the s-SNOM is sensitive solely to the signal emerging from the mutual tip-antenna interaction, the field radiated by the polarized tip includes under the weak scattering approximation a complete information available to the experimentalist, hence, all the scattering events included in (3.26).

We can convince ourselves of it by tracking the above described scattering process. First the external field meets the antenna and polarizes it. In our new perspective, the external field already contains the whole scattering process taking place on the bare antenna. Therefore, the near-field of the antenna becomes a part of the external field. Now, we introduce the tip into the system and look at the radiation scattered towards the detector. Because the tip radiates in the vicinity of the antenna, the scattered field must clearly contain a directly scattered part, identifying the $\mathbf{E}^{\mathrm{T}}$ and $\mathbf{E}^{\mathrm{TA}}$ terms of (3.26), and a part which is reflected from the antenna, being

consequently found as the contributions $\mathbf{E}^{\mathrm{AT}}$ and $\mathbf{E}^{\mathrm{ATA}}$ of (3.26). We came to the conclusion that the field radiated by the polarized tip can be written as

$$\mathbf{E} = \mathbf{E}^{\mathrm{T}} + \mathbf{E}^{\mathrm{TA}} + \mathbf{E}^{\mathrm{AT}} + \mathbf{E}^{\mathrm{ATA}}. \tag{3.27}$$

The tip is in general an extended polarizable object, however, with a sharp apex having a curvature ranging in the order of tens of nanometers. In a reasonable approximation, we can treat the tip effectively as a point-like polarizable object, characterized by a polarizability $\boldsymbol{\alpha}_{\mathrm{T}}$. Once the tip is polarized by the antenna, it radiates as a point dipole towards the detector and its field can be described by means of our new Green's dyadic $\boldsymbol{\mathcal{G}}(\mathbf{r}, \mathbf{r}')$ for environment containing both the substrate and the antenna

$$\mathbf{E}(\mathbf{r}_{\mathrm{D}}) = \frac{k^2}{\varepsilon_0} \boldsymbol{\mathcal{G}}(\mathbf{r}_{\mathrm{D}}, \mathbf{r}_{\mathrm{T}}) \cdot \mathbf{p}_{\mathrm{T}}, \tag{3.28}$$

where $\mathbf{p}_{\mathrm{T}} = \boldsymbol{\alpha}_{\mathrm{T}} \cdot \mathbf{E}^{\mathrm{I}}(\mathbf{r}_{\mathrm{T}})$ is the dipole moment of the radiating tip induced by an incident field $\mathbf{E}^{\mathrm{I}}(\mathbf{r}_{\mathrm{T}})$. Furthermore, the incident light, inducing the sought antenna near-fields, can be considered as a field of a distant radiating external dipole source $\mathbf{p}_{\mathrm{D}}$. The dyadic Green's function formalism immediately yields the solution for the incident light distribution:

$$\mathbf{E}^{\mathrm{I}}(\mathbf{r}) = \frac{k^2}{\varepsilon_0} \boldsymbol{\mathcal{G}}(\mathbf{r}, \mathbf{r}_{\mathrm{D}}) \cdot \mathbf{p}_{\mathrm{D}}. \tag{3.29}$$

We can put the two situations together and write the field scattered by the tip into the position of the detector (3.28) with help of the expression for the incident field (3.29)

$$\mathbf{E}(\mathbf{r}_{\mathrm{D}}) = \frac{k^2}{\varepsilon_0} \boldsymbol{\mathcal{G}}(\mathbf{r}_{\mathrm{D}}, \mathbf{r}_{\mathrm{T}}) \cdot \boldsymbol{\alpha}_{\mathrm{T}} \cdot \frac{k^2}{\varepsilon_0} \boldsymbol{\mathcal{G}}(\mathbf{r}_{\mathrm{T}}, \mathbf{r}_{\mathrm{D}}) \cdot \mathbf{p}_{\mathrm{D}}. \tag{3.30}$$

But we are interested in the polarization resolved signals. The linear polarizer (analyzer) inserted into the optical set-up will select only the projection of the scattered field into its axis oriented along some vector $\mathbf{D}$. Mathematically:

$$E_{\mathrm{D}} = \mathbf{D} \cdot \mathbf{E}(\mathbf{r}_{\mathrm{D}}) = \mathbf{D} \cdot \frac{k^2}{\varepsilon_0} \boldsymbol{\mathcal{G}}(\mathbf{r}_{\mathrm{D}}, \mathbf{r}_{\mathrm{T}}) \cdot \boldsymbol{\alpha}_{\mathrm{T}} \cdot \frac{k^2}{\varepsilon_0} \boldsymbol{\mathcal{G}}(\mathbf{r}_{\mathrm{T}}, \mathbf{r}_{\mathrm{D}}) \cdot \mathbf{p}_{\mathrm{D}}. \tag{3.31}$$

We can exploit the symmetry property of the dyadic Green's function $\boldsymbol{\mathcal{G}}(\mathbf{r}_{\mathrm{T}}, \mathbf{r}_{\mathrm{D}}) = \boldsymbol{\mathcal{G}}^{\tau}(\mathbf{r}_{\mathrm{D}}, \mathbf{r}_{\mathrm{T}})$ (superscript τ denoting transposition) and change the order of $\mathbf{D}$ and $\boldsymbol{\mathcal{G}}$ to get

$$E_{\mathrm{D}}(\mathbf{r}_{\mathrm{T}}) = \frac{k^2}{\varepsilon_0} \boldsymbol{\mathcal{G}}(\mathbf{r}_{\mathrm{T}}, \mathbf{r}_{\mathrm{D}}) \cdot \mathbf{D} \cdot \boldsymbol{\alpha}_{\mathrm{T}} \cdot \frac{k^2}{\varepsilon_0} \boldsymbol{\mathcal{G}}(\mathbf{r}_{\mathrm{T}}, \mathbf{r}_{\mathrm{D}}) \cdot \mathbf{p}_{\mathrm{D}}. \tag{3.32}$$

The expression $\mathbf{E}^{\mathrm{D}}(\mathbf{r}_{\mathrm{T}}) = \frac{k^2}{\varepsilon_0} \boldsymbol{\mathcal{G}}(\mathbf{r}_{\mathrm{T}}, \mathbf{r}_{\mathrm{D}}) \cdot \mathbf{D}$ can be interpreted as a field of the dipole which is placed into the position of the detector and has the same orientation as the analyser. Hence, we can conclude that the measured polarization resolved signal is proportional to

$$E_{\mathrm{D}}(\mathbf{r}_{\mathrm{T}}) = \mathbf{E}^{\mathrm{D}}(\mathbf{r}_{\mathrm{T}}) \cdot \boldsymbol{\alpha}_{\mathrm{T}} \cdot \mathbf{E}^{\mathrm{I}}(\mathbf{r}_{\mathrm{T}}). \tag{3.33}$$

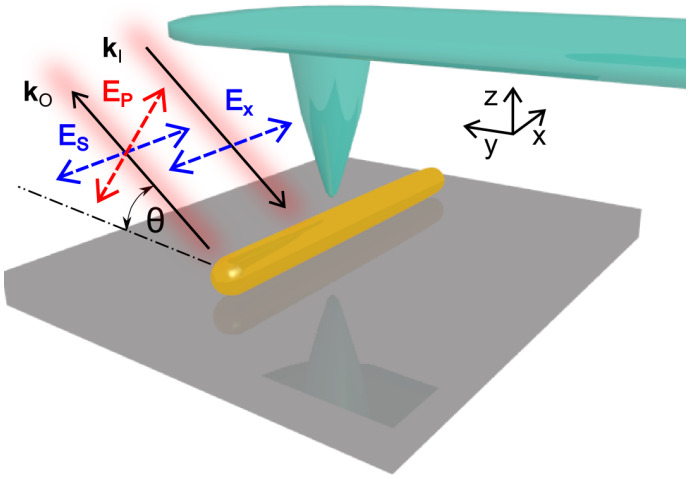

Figure 3.3: Experimental set-up for single linear antenna near-field measurement. The antenna is illuminated under $\theta = 45°$ angle of incidence and the signal is collected in the back scattering geometry. The incident light is polarized along the antenna longitudinal axis which coincides with the x axis of the Cartesian coordinate system. Two polarization resolved signals denoted by E_{S} and E_{P} are measured in the far field.

The polarization resolved signal can therefore be obtained as a scalar product of the tip induced dipole moment calculated directly from the antenna near-field and the field which would be excited around the antenna, if the antenna was illuminated by an incident light emitted by a dipole aligned with the analyser orientation. The expression (3.33) is actually a recipe how to calculate the s-SNOM signal for arbitrary geometry and for arbitrary illumination and detection polarization and direction. For the calculation of the sample near-fields one can easily employ any conventional Maxwell's equations solver, such as the FDTD Lumerical Solutions software. The major advantage of the developed approach is that one does not have to calculate the scattered signal for each position of the tip, which is a rather lengthy calculation procedure, but it is sufficient to solve the Maxwell's equations only twice. Moreover, the expression (3.33) applied to simple geometries allows for interpretation of the measured signal in terms of the antenna near-field components.

Let us consider in particular a single linear antenna in the back scattering set-up using an illumination and detection angle of $\theta = 45°$ as depicted in Figure 3.3. The antenna is illuminated by the S polarized light and the back scattering signal is measured in both the S and P polarizations. Intuitively we expect that the light incident in the S polarization excites the antenna dipole mode. Once we place the s-SNOM tip close to the antenna, the back scattering signal can be obtained by combining the field attributed to the existing electric field of the antenna dipole mode and the field which would be excited by illumination with polarization of the detected signals – S and P. Equation (3.33) gives results for the respective signals:

$$E_{\mathrm{S}}(\mathbf{r}_{\mathrm{T}}) = \mathbf{E}^{\mathrm{S}}(\mathbf{r}_{\mathrm{T}}) \cdot \boldsymbol{\alpha}_{\mathrm{T}} \cdot \mathbf{E}^{\mathrm{S}}(\mathbf{r}_{\mathrm{T}}), \tag{3.34}$$

$$E_{\mathrm{P}}(\mathbf{r}_{\mathrm{T}}) = \mathbf{E}^{\mathrm{P}}(\mathbf{r}_{\mathrm{T}}) \cdot \boldsymbol{\alpha}_{\mathrm{T}} \cdot \mathbf{E}^{\mathrm{S}}(\mathbf{r}_{\mathrm{T}}). \tag{3.35}$$

The tip polarizability tensor yields in the Cartesian coordinates defined in Figure 3.3 a diagonal form, remaining, however, generally anisotropic

$$\boldsymbol{\alpha}_{\mathrm{T}} = \begin{pmatrix} \alpha_{xx} & 0 & 0 \\ 0 & \alpha_{yy} & 0 \\ 0 & 0 & \alpha_{zz} \end{pmatrix}. \tag{3.36}$$

The $S-$polarized signal obviously rises merely from the field distribution induced by the incident $S-$polarized light and leads to the interpretation of the signal in terms of the antenna near-field components:

$$E_{\mathrm{S}}(\mathbf{r}_{\mathrm{T}}) \sim \alpha_{xx} E_x^2(\mathbf{r}_{\mathrm{T}}) + \alpha_{yy} E_y^2(\mathbf{r}_{\mathrm{T}}) + \alpha_{yy} E_z^2(\mathbf{r}_{\mathrm{T}}). \tag{3.37}$$

Before we try to interpret the P-polarized signal, we have to consider how the P-polarized incident light interacts with the linear antenna. The electric field of the incident light will be perpendicular to the antenna axis. From the defined geometry we immediately recognize that the illuminating light has only two non-zero Cartesian components, E_y and E_z. In case that we consider the interaction of the incident light with the antenna as weak, we can, in the first approximation, neglect the influence of the antenna induced fields. In other words, we disregard the antenna polarizability in the yz direction, considering the antenna polarizability tensor:

$$\boldsymbol{\alpha}_{\mathrm{A}} = \begin{pmatrix} \alpha_{xx}^{\mathrm{A}} & 0 & 0 \\ 0 & \alpha_{yy}^{\mathrm{A}} & 0 \\ 0 & 0 & \alpha_{zz}^{\mathrm{A}} \end{pmatrix} \sim \begin{pmatrix} \alpha_{xx}^{\mathrm{A}} & 0 & 0 \\ 0 & 0 & 0 \\ 0 & 0 & 0 \end{pmatrix}. \tag{3.38}$$

The interpretation of the P-polarized signal emerges as a projection of the antenna dipole mode near-field components into the incident light components E_y and E_z with appropriately chosen signs (see the Figure 3.3)

$$E_{\mathrm{P}}(\mathbf{r}_{\mathrm{T}}) \sim \alpha_{zz} E_z(\mathbf{r}_{\mathrm{T}}) - \alpha_{yy} E_y(\mathbf{r}_{\mathrm{T}}). \tag{3.39}$$

Hence, the P-polarized signal is proportional to the linear combination of the antenna near-field components E_y and E_z. The results in (3.37) and (3.39) provide a novel view of the s-SNOM signal in terms of the detected near-field components. A striking consequence of the signal interpretation is that the signal detected in S-polarization not only depends on all of the antenna near-field components, but it depends on their square. This conclusion is in disagreement with the commonly accepted interpretation of the S-polarized signal in terms of only the component E_x [61, 62]. The squaring of components comes here as a direct result of the double scattering event taking place on the antenna, which has been reported in the surface enhanced Raman spectroscopy [7, 63], surface enhanced infrared spectroscopy [64] and recently also experimentally observed in the s-SNOM measurements of infrared antennas [65].

In the following section we will provide an experimental proof of our signal interpretation on examples of a single and a dimer linear antenna, which both have a high application potential in the surface enhanced infrared spectroscopy. Especially the dimer antennas provide a huge near-field enhancement in the central gap region, which might lead to enormous signal enhancements leading up to single molecule detection sensitivities.

3.2.2 Comparison with experiment

Before we introduce the experimental results, we need to discuss another aspect of the experimental signal formation, the oscillations of the tip. We have already stated that the signal detected by s-SNOM on higher harmonic frequencies corresponds to the higher order derivative of the signal obtained along the vertical trajectory of the tip oscillations. In our considerations we used a harmonically oscillating tip. However, there are a few physical reasons why the tip oscillation does not necessarily need to exhibit a harmonic movement. The anharmonically oscillating tip can be commonly found in the tapping mode AFM microscopy, on top of it, the anharmonic oscillations of the tip have already been exploited for material characterization and obtaining of AFM chemical contrast [66].

Another argument which supports the idea of anharmonically oscillating tip rises from the physics of the antenna-tip interaction. We considered the tip to be a point-like scatterer which effectively reflects the interaction of the tip with the surrounding environment. This definition, however, does not necessarily mean that the equivalent point-like scatterer strictly copies the tip trajectory during the oscillation. In the highly variable near-fields, the effective tip interaction volume and the equivalent scatterer position with respect to the tip apex might slightly differ during the detection process.

The idea of the anharmonically oscillating tip is not entirely new in s-SNOM. It has already been considered for calculations of the s-SNOM signal of buried objects [67]. Here, we do not want to extend the idea of anharmonic oscillations, even though we believe that it deserves a serious theoretical and experimental treatment, and we adopt the tip anharmonic oscillations in a simplified phenomenological form [67]

$$\mathbf{r} = \mathbf{r}_{\parallel} + \mathbf{e}_z \left\{ z_{\min}(\mathbf{r}_{\parallel}) + \Delta + \frac{\Delta}{\Delta + \delta} \left[\Delta \cos(\Omega t) + \delta \cos(3\Omega t) \right] \right\}, \tag{3.40}$$

where δ represents an anharmonicity parameter, Δ is the amplitude of the tip oscillation. In the following, we will consider only the signal demodulated on the third harmonic frequency of the tip ($n = 3$) oscillation and we, therefore, expect that the strongest contribution of the tip anharmonic oscillation also originates in the third harmonic of the tip base frequency. The signal obtained by s-SNOM higher harmonic interferometric detection can be subsequently obtained by applying standard procedures of Fourier analysis [67].

The experimental results which will be presented further in this section were obtained in CIC nanoGUNE[3] by the nanooptics group led by Prof. Rainer Hillenbrand. The experimental set-up used for measurement of both the single and the dimer gold linear antennas was the same as described in the previous section and as depicted in Figure 3.3. The pseudo-heterodyne detection has been employed on the third harmonic frequency of demodulation in order to eliminate the background contributions. The antennas were designed to be resonant on wavelength of 11.06 µm produced by a CO_2 laser. The antennas were fabricated by e-beam lithography on a

[3]Nanooptics Laboratory, CIC nanoGUNE, 20018 Donostia - San Sebastián, Spain.

CaF_2 substrate and their dimensions were selected as follows. The single linear antennas were 3.8 µm long with diameter of 150 nm and the arms of the dimer antennas had length of 3.35 µm and a gap of 30 nm separating them.

Single linear antenna

The single linear antenna is a typical example of a plasmonic structure which has been subject of a great scientific interest for years especially with respect to an application potential in enhanced spectroscopy. Here we demonstrate, how it is possible to directly access its near-field properties with use of a s-SNOM probe. The experimental images of the polarization resolved s-SNOM measurement on the third harmonic frequency are depicted in Figure 3.4. Figure 3.4 a) shows the antenna topography obtained from the standard AFM signal of the s-SNOM. For our theoretical calculations we considered an idealized model of a smooth dipole antenna having dimensions closely corresponding to the experiment [Figure 3.4 b)]. The signal depicted in Figure 3.4 b) left shows a distribution of a P- polarized signal amplitude and phase scanned above and around the antenna and demodulated on the third harmonic frequency. We can observe regions of a strong signal amplitude above the antenna apexes which reflect the expected field enhancement of the antenna dipole mode excited by the incident light polarized along the antenna longitudinal axis. The phase of the P-polarized signal exhibits areas of a constant value depicted in red and blue color respectively, which assigns the areas of phase differing by a π, hence, areas of the signal of opposite sign. Exactly this phase jump in the x direction would be expected for near-fields of the antenna dipole mode. However, we can also clearly observe a phase jump in the y direction situated along the antenna border. This feature can be explained with help of theoretically calculated near-field distribution of the antenna near-fields which is depicted in Figure 3.4 c)[4].

The measured phase pattern of the P-polarized signal resembles the phase image obtained for the y component of the near-field with the slight difference of the y direction phase jump position. While the P-polarized experimental signal depicts the phase jump taking place close to the antenna edge, the y component obviously changes the phase exactly in the center of the antenna. If we, on top of that, consider influence of the z component of the near-field on the measured signal, we can finally explain the y direction phase jump by a simple linear combination of the near-field components E_y and E_z.

Once the tip is scanned above the antenna along the y axis, it obviously starts to detect the E_y component of the near-field in the region beside the antenna. The situation changes dramatically when the tip reaches the antenna itself, where the near-field pointing in the radial direction out of the antenna surface gradually rotates into the z direction, and the detected signal starts to sense merely the E_z component of the antenna near-field which has, in our case, the phase opposite to the previously felt E_y component of the electric field. Further y movement of the tip again restores the dominance of the E_y component contribution. Importantly,

[4]The theoretical calculations were performed using the FDTD Lumerical Solutions software, fully including influence of the CaF_2 substrate.

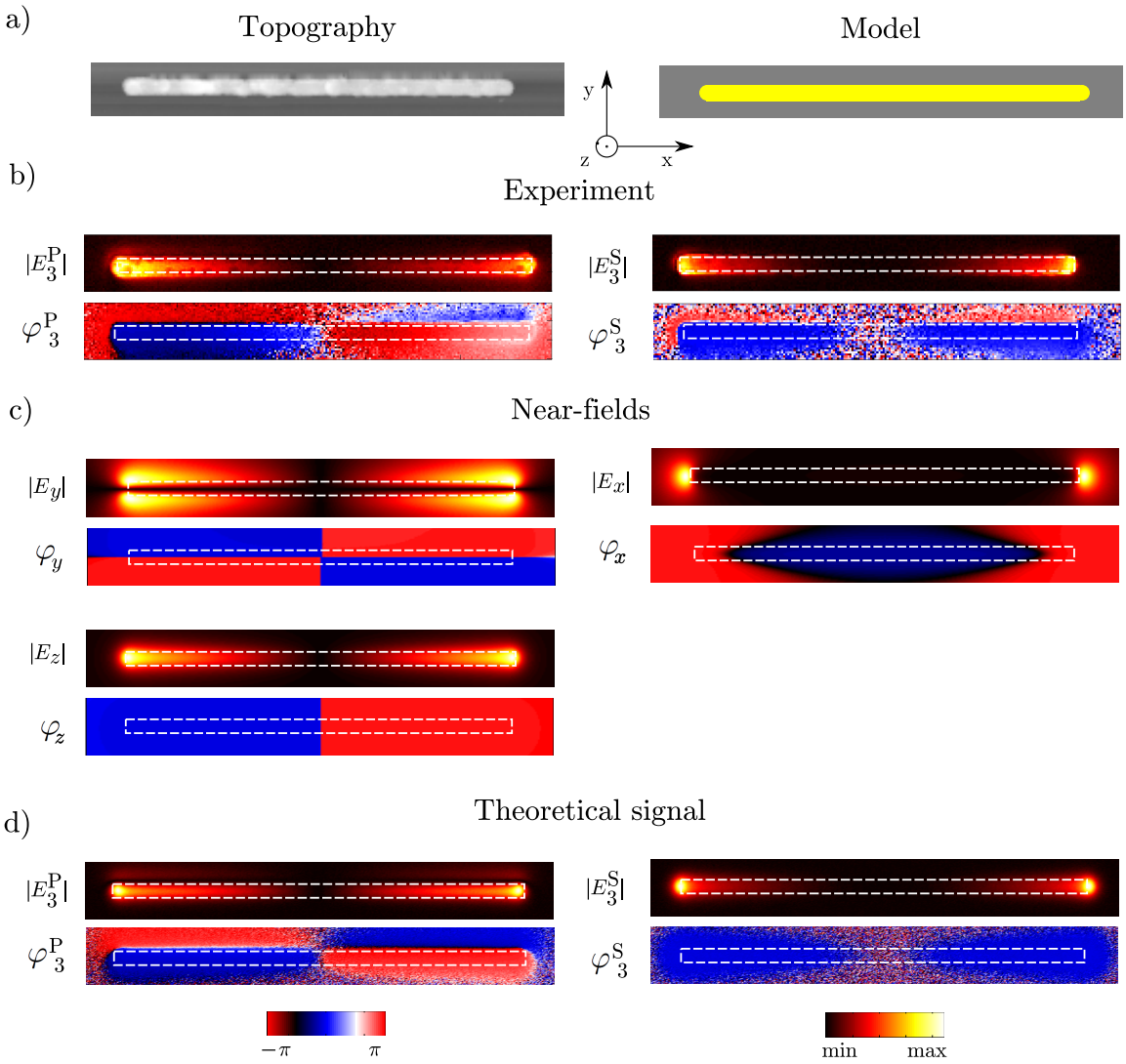

Figure 3.4: Comparison of an experimental signal and theoretical results obtained for the single linear antenna described in the text. Figure a) depicts the topography image as a result of the AFM signal of the s-SNOM tip and a model topography which has been used for calculations. Experimental signals are shown in b), the P-polarized signal on the left and the S-polarized signal on the right part of the figure. Section c) shows numerically calculated near-field component amplitudes and phases. The experimental images are compared with the respective theoretically calculated signals in d). The theoretical signals were demodulated on the third harmonic frequency and anharmonic tip motion has been considered. We added an artificial noise to the theoretical signal to account for the experimental conditions. The noise was generated with normal distribution centred at zero and standard deviation equal to 1 % of the signal maximum value. We considered $\alpha_{zz} = \alpha_{xx} = \alpha_{yy}$.

the interplay between the E_y and E_z component will be balanced somewhere close to the antenna edge, where the vector of electric near-field changes its direction.

We are still left with one unanswered question consisting in determination of the linear superposition constants standing in front of the respective near-field components, E_y and E_z. The geometry of the scattering in the 45° angle dictates the superposition of exactly the same form as obtained in (3.39). For completion of our discussion, the theoretical signal distribution obtained for constant height scan with help of the equation (3.35) is depicted in Figure 3.4 d) left. Both signals in Figure 3.4 d) were obtained for anharmonic tip oscillations with $\delta = 0.05\Delta$ and for better comparison with experiment, an artificial noise was added[5]. The theoretically calculated image is in an almost perfect match with the experiment, hence, the designed signal interpretation succeeds in description of the P-polarized signal. The theoretical model correctly predicts even the asymmetry of the signal amplitude measured along the y axis, when the tip ranges through areas where the signal is dominated by different contributions of the components E_y and E_z.

Interestingly, we were able to reconstruct the P-polarized signal amplitude and phase simply with help of the considerations based on the antenna local field distribution and possible superposition effects connected with the detection geometry. The above discussion and obvious correct interpretation of the signal assured the experimentalists about the formerly used interpretation of the signal directly in terms of the near-field components. However, in case of the linear dipole antenna, this is just a lucky coincidence that the P-polarized signal emerges as the intuitively predicted linear combination of the near-field components. We will see later that the signal must be treated with help of the expressions (3.34) and (3.35) in generality.

Consider now the third harmonic experimental S-polarized signal which is depicted in Figure 3.4 b) right. The signal amplitude peaks strongly in areas of the antenna extremities, where the near-fields reach the maximum enhancement. Closer comparison of the P-polarized and the S-polarized signal reveals stronger confinement of the S-polarized signal amplitude to the antenna apexes than in the previous case. The S-polarized signal phase distribution image depicts an extended blue area stretching above the whole antenna length, marking the constant phase of the signal detected right above the antenna. In the y direction, the phase also undergoes a jump from the blue color towards the red.

If we make an attempt to interpret the measured signal again solely with help of the linear combination of the near-field components, we must obviously fail. None of the near-field components resembles the observed behaviour of the signal. We can see in Figure 3.4 c) that the component E_x of the antenna near-field exhibits a field of constant phase right above the antenna, but its amplitude distribution is very far from observed results. The maximum enhancement of the component E_x takes place outside of the antenna (in the x direction) and almost no signal is found above the antenna itself, which is in contradiction with the experiment. We can interpret the signal by considering that the s-SNOM measures squares of the near-field components in the S-polarized signal. If it was so, the phase above both antenna extremities would be the same, since we observe in the linear case

[5]We used addition of a complex signal noise having a normal distribution with standard deviation being 1 % of the signal maximum value.

a difference of sign between different regions of the signal which would obviously disappear after the squaring.

The theoretical signal calculated with help of equation (3.34) is depicted in Figure 3.4 d) right. The theoretical signal manages to explain the constant phase above the whole antenna, however, it fails to provide an interpretation of the phase jump taking place in the y direction. We did not manage to provide any satisfactory explanation for this experimental feature so far and we believe that this might be a result of some experimental detail which has not been taken into consideration for our calculations, such as some kind of mechanical interaction between the tip and the sample during the scan along the antenna border or even effect of a strong interaction between the tip and the antenna.

We might bring further insight into the results by plotting the amplitude profile captured along the antenna longitudinal axis in Figure 3.5. The Figure 3.5 left (black line) shows experimental P-polarized line profile which is compared with profiles obtained by means of the theoretical description – the non-demodulated signal and the demodulated signal with use of the harmonically and anharmonically oscillating tip, together with equation (3.35). The P-polarized signal must obviously reflect the spatial dependence of the near-field component E_z. We are now especially interested in behaviour of the signal in the area close to the antenna centre, where the P-polarized signal resembles graph of the absolute value function, hence, a function which corresponds to linear increase of the signal. We can see that all of the calculated signals manage to copy the experimental signal function dependence in the centre of the antenna, exhibiting a clear V-shaped profile.

Let us turn our attention to the S-polarized signal which is depicted in Figure 3.5 right. The line plots depict the experimental and theoretical signals in analogy with the P-polarized signal, where only the use of equation (3.34) was made. By inspecting the central region of the plot, we can observe a U-shaped profile for all of the measured and calculated signals which indicates a parabolic dependence. We can conclude by putting together the results obtained for the P-polarized signal and the S-polarized signal that the S-polarized signal emerges as a square of the near-field component distribution, which provides a significant support for the model and the interpretation developed herein.

One might notice that there are a few discrepancies between the experimental signal and the signal calculated theoretically according to (3.33) in Figure 3.5. First of all, the fully demodulated signal always peaks sharper around the antenna extremities than the non-demodulated or the experimental signal. This is a direct result of the higher harmonic signal interpretation in terms of the higher order derivatives in the z direction. It is well known that the signal tends to sharpen on higher harmonic frequencies and it is even considered as one of mechanisms for the lateral resolution improvement. Possible explanation of the mentioned phenomenon might rest in the tip anharmonic motion. We see that the signal amplitude converges back to the non-demodulated amplitude with increasing tip anharmonicity.

Another discrepancy can be found between the P-polarized detected and theoretical signal. The theoretical signal possesses steeper slope in the proximity of the antenna center than the experimental signal and undergoes a gradual slope decrease towards the antenna apexes where it again finally peaks. The distorted theoretical

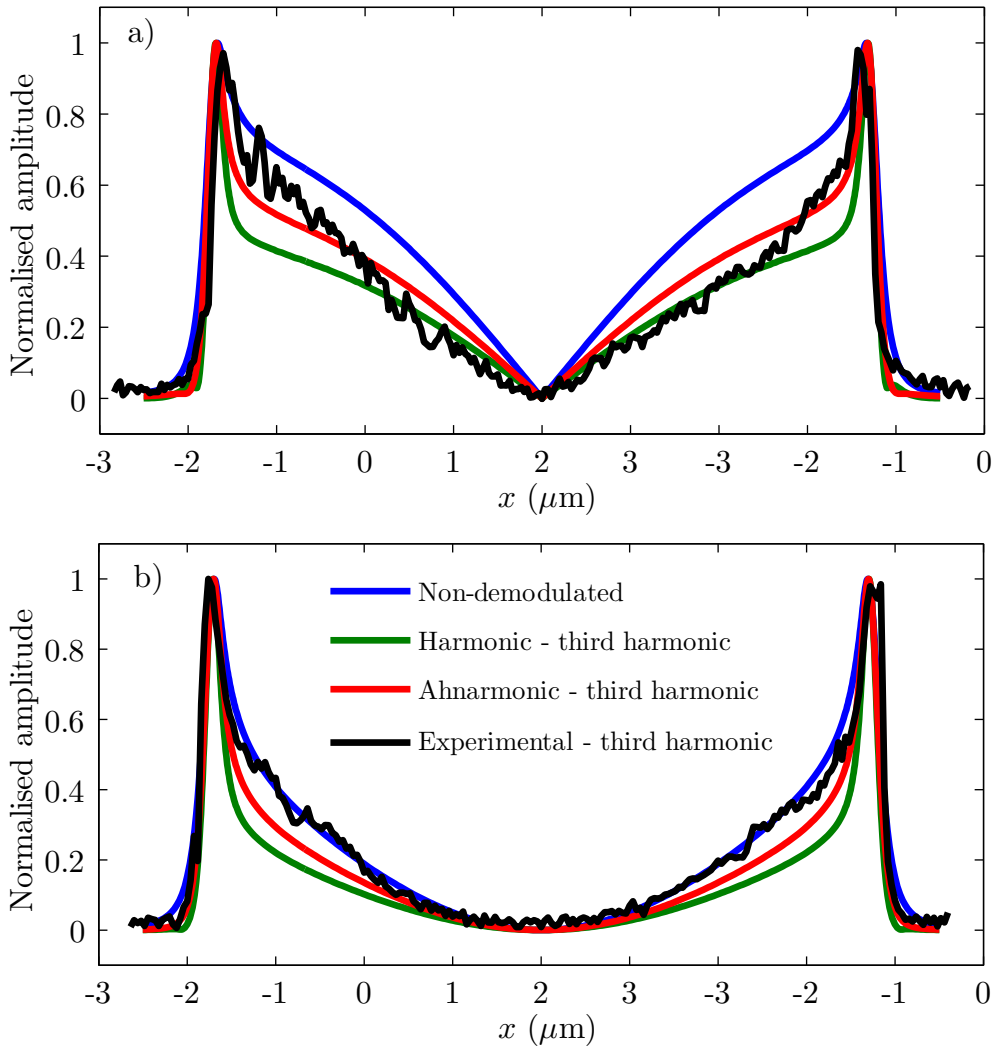

Figure 3.5: Line profiles of the a) P-polarized signal and b) S-polarized signal taken along the antenna center. The images depict Theoretical non-demodulated signal (blue), theoretical signal considering harmonic tip oscillations (green) and anharmonic tip oscillations (red) demodulated of the third harmonic frequency compared with the experimentally obtained signal demodulated on the third harmonic frequency (black). In calculation of anharmonic signals we used the formula (3.40) with $\delta = 0.05\Delta$. We considered $\alpha_{zz} = \alpha_{xx} = \alpha_{yy}$.

profile might be a result of an inaccuracy of the simulation set-up with respect to the real experiment. In the simulation, we consider that the antenna is placed into the focus of a Gaussian laser beam while the tip is scanned around the antenna. In reality, however, the antenna is scanned with respect to the stationary system of the tip and the laser focus. Illumination by the Gaussian beam therefore increases the field amplitude in the antenna center, which does not happen in the experiment. This enhancement in the antenna center is especially significant for calculation of near-field distribution resulting from illumination by the P-polarized light which we perform to obtain the resulting signal [see expression (3.35)]. We may therefore expect a smoother linear dependence of the theoretical signal for more realistic simulation arrangements.

In conclusion, we have managed to interpret the main features observed in the near-field detection of the antenna components of the electric field with help of our theoretical model. We have successfully interpreted the signal measured in the P-polarization as a linear combination of near-field components E_x and E_y. It has been shown that interpretation of the S-polarized signal cannot be achieved by solely considering the linear dependence on the local field components and that double scattering event taking place on the antenna leads to squaring of the S-polarized signal.

We will apply now our formalism on an example of a simple metallic structure which provides enormous field enhancements in a narrow spatial region. The structure consists of two linear arms placed close together in order to form a nanometer-sized gap region. Structure of this kind is ordinarily called a dimer antenna. Due to the capacitive coupling of the two antenna arms [68], the gap region provides a huge field enhancements, making of the antenna an efficient nano-focusing device for infrared radiation. In the following section, we will present measurement and interpretation of the S- and P-polarized s-SNOM signal detection of the antenna near-fields with special interest in the regions with high concentration of the electromagnetic field energy, the so called hot spots.

Dimer antenna – hot spots

Experimental images of the dimer antennas are depicted in Figure 3.6. They share most of the details with the single linear antennas, which have already been discussed in the previous section. We can consider that the dimer antenna is an object with one dominant axis of polarizability being identical with the longitudinal axis, and therefore, the interpretation in terms of linear combination of near-field components or the component squaring developed so far should apply equally for the dimer antennas.

The basic bright mode of the linear dimer antenna is resonantly excited by the incident infrared radiation polarized along the longitudinal antenna axis. The experimental image of the P-polarized signal shown in Figure 3.6 exhibits enhancement of the signal amplitude in areas above the antenna extremities. The phase of the signal alternates along the antenna axis, exhibiting lobes of constant phase depicted in blue and red color, hence, differing by a sign. The sign of the signal changes across the gap region, which obviously means that the gap is surrounded by oppositely charged antenna arms. Such a situation might be compared to the well known

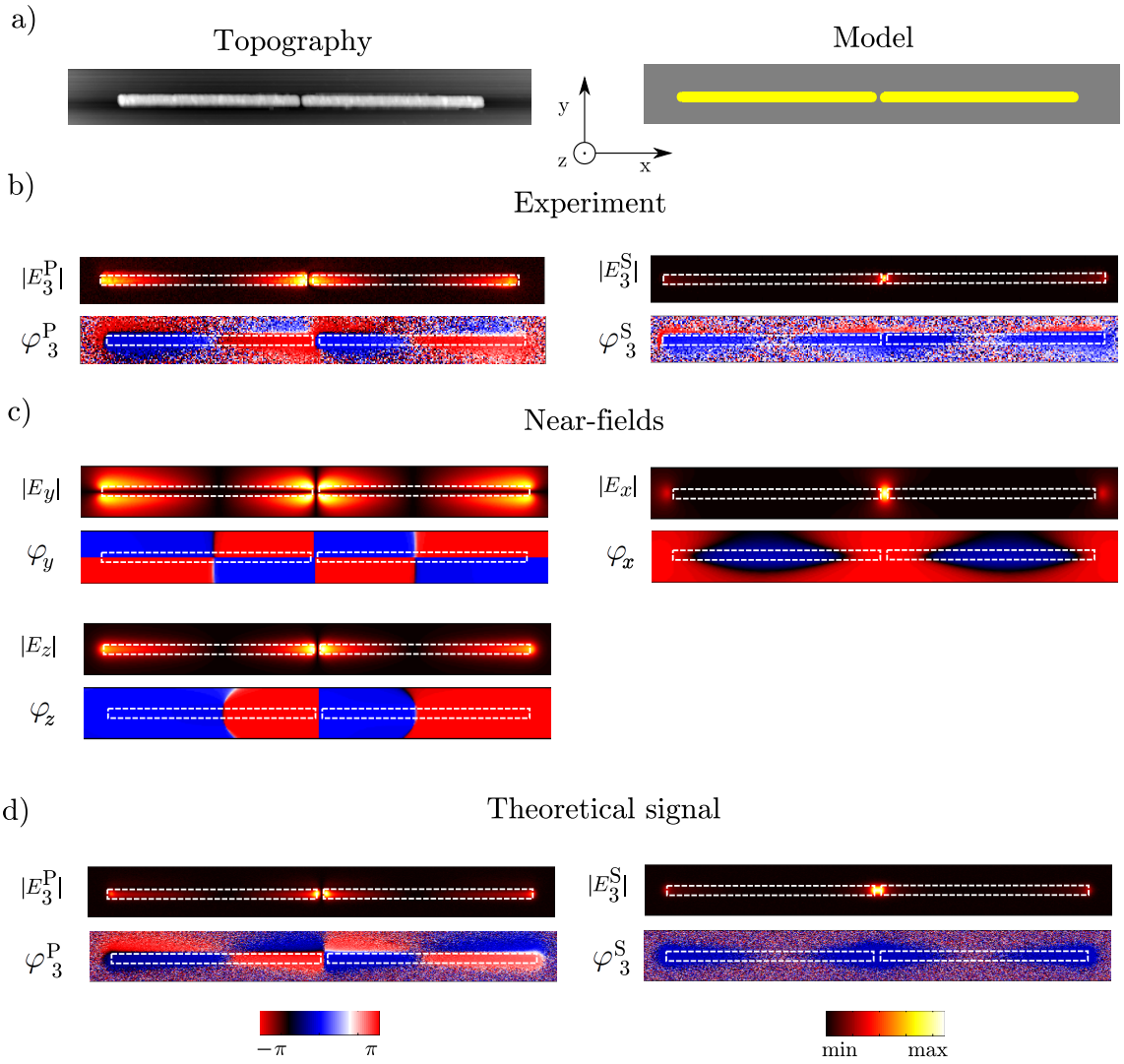

Figure 3.6: Comparison of an experimental signal and theoretical results obtained for the dimer linear antenna. Experimental signals and theoretical calculations are depicted in analogy with 3.4. Figures a) depict the topography image and a model topography used in calculations. Experimental signals are shown in b), the $P-$polarized signal on the left and the $S-$polarized signal on the right part of the figure. The calculated near-field components in c) are compared to both the experiment and the theoretical signals which are displayed in d). The theoretical signals were demodulated on the third harmonic frequency and anharmonic tip motion has been considered. We added an artificial noise to the theoretical signal to account for the experimental conditions. The noise was generated with normal distribution centred at zero ad standard deviation equal to 1 % of the signal maximum value. We considered $\alpha_{zz} = \alpha_{xx} = \alpha_{yy}$.

case of a slab capacitor, where two electrodes held on opposite potential produce a relatively strong electric field in the central region. The so called capacitive coupling, which occurs in case of the linear dipole antenna bright mode, therefore leads to similarly strong enhancement of the near-field component E_x in the gap region. The components of the near-field E_z and E_x, on the other hand, undergo an abrupt phase change across the gap which implies that the amplitudes of the components E_y and E_z must vanish here. This is exactly what we can observe on the P-polarized signal amplitude image. The signal is enhanced in the close proximity of the gap, however, there is a dark spot in the gap center.

Information on behaviour of the near-field component E_x can be reached by the $S-$polarized s-SNOM signal which is depicted in Figure 3.6 b) right. Both amplitude and phase of the signal are triggered by the near-field component squaring process, leading to signal higher values in areas above antenna apexes and blue lobes of constant phase above the whole antenna. We must not be confused by appearance of the high signal values above the antenna arms which are formed mainly by contribution of the component E_z to the signal, appearing here moreover in the form of the second power. The S-polarized signal indeed provides information about the near-field component E_x, but in most instances, the signal resulting solely from the E_x component is overshadowed by influence of the remaining near-field components. Very often, such as in case of the antenna extremities, the S-polarized signal provides even information solely about the remaining near-field components.

In the antenna gap, we see a strong signal rising from the capacitively enhanced component E_x of the antenna near-field. We can conclusively claim that we observe the component E_x of the near-field because we already know that the P-polarized signal consisting of contributions from the components E_y and E_z shows a vanishing amplitude in the gap region which can not follow from superposition of the components E_y and E_z for the symmetry reasons. The only component which might therefore contribute to the S-polarized signal in the center of the antenna gap is the remaining one, E_x. The component E_x appears in the S-polarized signal in the form of a square which is a natural consequence of our formalism. The squaring of the S-polarized signal in the dimer antenna gap was published in reference [65] and became also inspiration for development of more complex description of the antenna-tip scattering process presented here. Interestingly, in reference [65] it was noted that the s-SNOM S-polarized signal reveals the double scattering enhancement process predicted in the surface enhanced Raman scattering [63]. In Chapter 5 we will also establish the connection of the measured signal with the surface enhanced infrared spectroscopy. The s-SNOM signal, therefore, in some situations provides more information about the antenna enhancement properties for spectroscopic purposes, rather than simply the near-field map, as it was considered before.

Even the case of the dimer linear antenna gives support to the theoretical approach developed here and emphasizes the main result obtained in this chapter; the s-SNOM signal must be treated in generality with care and in case, when weakly scattering probe is used, the signal provides information generally on a quadratic expression consisting of the near-field components.

3.2.3 Further experimental investigation

The results of this chapter clearly indicate that the near-field microscopy provides rather surprising information about the studied sample. We found a good match between experiment and theoretical prediction for a linear dipole antenna and a dimer linear antenna in most aspects, including the predicted squaring of components. Throughout the literature, one can find a wide spectrum of experimental results obtained by s-SNOM operated in both infrared and visible regime, where the interpretation of the results in terms of near-field components alone has led to a good agreement with experiment even for complex geometries [69].

We see that even though we presented a theory of weakly interacting s-SNOM interpretation, the question of signal interpretation remains unanswered in general. The theory of weakly interacting tips is based on an assumption that the expression (3.22) can be expanded into the Taylor series, which in turn shows up to be the series of the multiple scattering events. Validity of the Taylor expansion remains, however, questionable in practical situations and the border between the weak scattering regime and the strong scattering regime is not obvious from simple considerations. We therefore propose further experimental investigation of the antenna-tip interaction, with special aim on distinction of the s-SNOM operating regimes, the weak scattering regime and the strong scattering regime. For this purpose, it is necessary to design a suitable infrared resonant structure which would have a well known and distinct resonant modes, allowing for simple determination of the scattered signal and its comparison to the experimental results.

We propose an experimental investigation on a metallic structure having a shape of letter 'T'. The T-shaped antenna together with its basic resonant modes is schematically depicted in Figure 3.7 a), b). We can distinguish two characteristic dipole resonances of the antenna, one which is antisymmetric and which can be excited by radiation polarized parallel with the horizontal bar of the antenna, and a dipole resonance which interacts with radiation polarized along the horizontal bar of the antenna, being a symmetric mode of the antenna. The T-shaped antenna can be studied in four distinct experimental configurations, combining the polarizations of incident light and the detected signal in the so called transmission mode. The experimental configuration is depicted in Figure 3.7 c) together with considered illumination and detection polarizations.

Major advantage of the proposed experimental configuration resides in interpretation of the detected signal in the weak interaction regime simply as products of the two basic antenna modes. This can be seen by realizing that the auxiliary illumination fields representing the detected signals will interact with the antenna in almost the same way as the illuminating radiation. We will focus now solely on fields and signals detected in the vicinity of the horizontal part of the T-shaped antenna. The antenna can be viewed alternatively as a dipole antenna, when the illumination is set along its longitudinal axis, or a monopole supplied by an electron reservoir of the perpendicular arm for illumination polarized perpendicularly to the horizontal bar.

The four possible results of the experiment in principle fall into two different classes. The first class, when cross polarization detection is used gives antisymmetric resulting signal, almost identical for both realizations of the cross-polarized

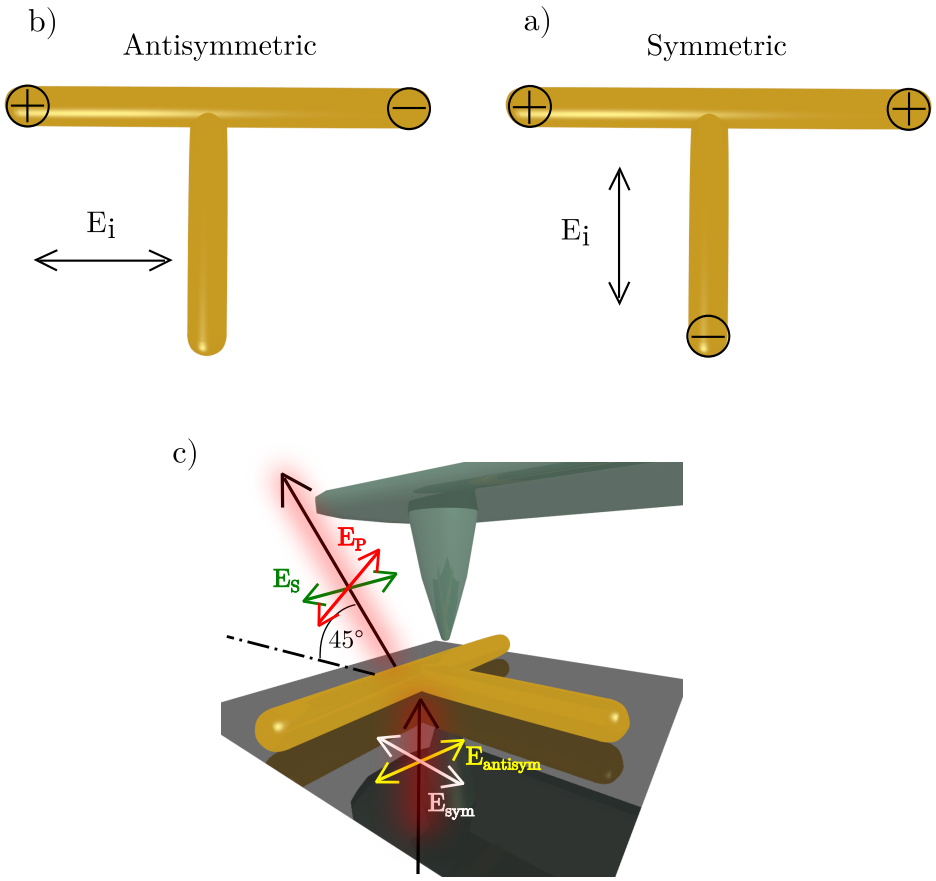

Figure 3.7: Schematic image of the T-shaped antenna illuminated by the incident light perpendicularly to the plain of the image with polarization exciting a) the antisymmetric mode and b) the symmetric mode. The pluses and minuses at the antenna apexes denote a sign of the surface charge distribution characteristic for each mode. Figure c) depicts experimental configuration for s-SNOM measurement of the antenna. Four possible combinations of incident light and detection polarizations are possible in principle, combining the illumination for symmetric and antisymmetric mode excitation with S- and P-polarized light detection. The detection angle is 45° as depicted in c).

detection. The remaining two cases should provide symmetric signal. The only difference between the symmetric signal obtained using the symmetric and antisymmetric incident light polarization will be qualitatively in the signal above the vertical antenna bar. For antisymmetric illumination and S-polarized detection, the signal will come almost exclusively from the area above the horizontal antenna bar. When the antenna will be illuminated by symmetric illumination and the P-polarized signal will be detected, the signal will be significant in the position of the vertical antenna bar.

The proposed analytical model further predicts for the measured signal in all of the considered configurations non-linear dependence on distance from the antenna center measured along the horizontal bar. The non-linearity comes as a result of the signal formation as a product of field distributions of the two modes. We therefore expect quadratic dependence for the signal amplitude, since we predict in accordance with results obtained on the linear antenna a linear dependence of the near-field amplitude on the distance from the center of the horizontal bar.

The systematic experimental investigation using different kinds of probes, starting with weakly interacting tips carrying a single carbon nanotube similarly as in reference [46], using dielectric (silicon) tips with gradually increasing apex radius towards huge strongly interacting metallic tips, should help to resolve the problem of practical validity of the weak interaction approximation. The proposed structure and subsequent simple signal interpretation will serve here as a valuable tool for distinction between the investigated regimes.

4 | Photoluminescence in near-field microscopy

In the previous chapter we have studied mutual interaction of a s-SNOM probe and the analysed sample antenna. We have implicitly presumed, that the mutual tip-antenna scattering is of an elastic character and the scattered light is therefore spectrally only hardly distinguishable from the huge background signal. The sophisticated interferometric detection mechanisms must have been employed for the scattered signal separation which made the actual experimental set-up vastly complicated. The interaction between the antenna and the tip does not, however, always need to realize on the frequency of the incident light. This can happen, when inelastic processes come to the scene. One of the most prominent inelastic processes studied in the field of optics and plasmonics is, aside of the Raman scattering, the photoluminescence.

Photoluminescence is an incoherent process of absorption and subsequent reemission of a photon, different from thermal emission. An important distinction between the scattering processes and the photoluminescence consists in the coherence. Unlike the inelastic scattering processes, the photoluminescence exhibits a stochastic emission behaviour which is characterized by a specific emission lifetime and loss of radiation coherence. Even the polarization of the emitted photon is randomized if the system allows for radiative transitions with different orientation of the transition dipole moment. The long lived excited states (10^{-4} s and more) set a basis for so called phosphorescence, where the final radiative transition violates selection rules and is therefore denoted as forbidden (transition between triplet and singlet states). Short lived excited states result in fluorescence ($10^{-8} - 10^{-5}$ s).

In this chapter, we will first shortly review the basic properties of photoluminescence and interaction of spontaneous emitters with plasmonic particles. Core of this chapter will reside in introduction of the state-of-the-art near-field microscopy techniques, exploiting properties of the photoluminescence. We will see, how photoluminescence can be utilized for mapping of local density of optical states (LDOS) in the vicinity of metallic nano- and microstructures and how the metal photoluminescence finds the application as an efficient tip-sample signal separation technique.

4.1 Plasmon enhanced spontaneous emission

The process of photoluminescence can be divided into three basic steps. At the beginning, an incident photon is absorbed by the photoluminescent structure. The

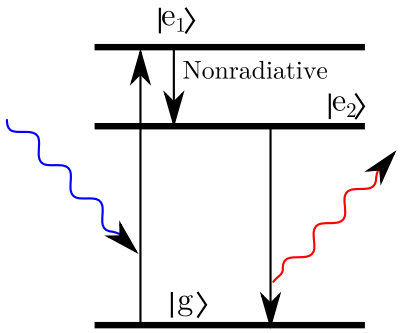

Figure 4.1: The three level diagram of photoluminescence. The photon of higher energy is absorbed and excites an electron from the ground state to the excited state. The electron relaxes by interaction with thermal excitations and after that decays to the ground state emitting a photon of lower energy.

absorption of the incident photon goes along with an electronic transition inside of the structure between some ground electronic state and an excited state.

The interaction of the excited state with phonons or molecular collisions and other mechanisms give rise to the so called dephasing. The dephasing leads to the loss of memory of the excited state and subsequently, the photon emission is independent on the absorption event. During the dephasing, the electron undergoes a fast relaxation to slightly different excited state associated with lower energies. The final transition to the ground state subsequently overcomes narrower energy gap. This phenomenon is a reason for the so called Stokes shift, where a red shift of the emitted photon is observed with respect to the excitation. The process consisting of the absorption, excited state relaxation and spontaneous emission is the so called photoluminescence (as schematically depicted in Figure 4.1).

Once we have a structure prepared in the excited state, we naturally ask, what the reason for the spontaneous emission of the photon is. There is not a simple answer to this question, actually, there is no answer at all in the framework of the classical physics. The quantum electrodynamics states that the spontaneous emission emerges as an interaction of the electronic system with vacuum fluctuations of the electromagnetic field. Once the fluctuations are present, they contribute to the transition element of the system Hamiltonian and enable the emission. For point-like emitters, it is possible to derive a formula for the spontaneous decay rate γ in general environment [19]

$$\gamma = \frac{\pi\omega|\mu|^2}{3\varepsilon_0\hbar}\rho(\mathbf{r},\omega), \tag{4.1}$$

where ω is the frequency of the transition, μ is the transition dipole moment, ε_0 is the vacuum permittivity, $\hbar$ is the reduced Planck's constant and ρ is the partial local density of photonic states (LDOS). It can be shown [19], that the LDOS is connected to the dyadic Green's function $\mathbf{G}(\mathbf{r},\mathbf{r},\omega)$ via

$$\rho(\mathbf{r},\omega) = \frac{6\omega}{\pi c^2}\Im\left\{\mathbf{n}\cdot\mathbf{G}(\mathbf{r},\mathbf{r},\omega)\cdot\mathbf{n}\right\}. \tag{4.2}$$

Here c is the vacuum speed of light and $\mathbf{n}$ is the orientation of the transition dipole. The formula (4.2) together with (4.1) is valid for arbitrary environments in the weak coupling regime. We note that the derivation can not employ simple electromagnetic eigenmode expansion for lossy environments, where the fluctuation-dissipation theorem is used instead [19].

The LDOS is directly proportional to the imaginary part of the dyadic Green's function, evaluated at the position of the source. We have shown in Chapter 2, that the free space dyadic Green's function imaginary part is regular at the origin and has value $k/6\pi$ ($k = \omega/c$). With use of this, the free space spontaneous decay rate is obtained

$$\gamma_0 = \frac{k^3|\mu|^2}{3\varepsilon_0\hbar\pi}. \tag{4.3}$$

Now it is straightforward to see, that the decay rate can be modified by adjustment of the dyadic Green's function. Simplest possible way of doing it is to embed the emitter into the dielectric environment. Indeed, the LDOS is modified by presence of the medium. However we note that local field effects can play here a considerable role on the final form of the LDOS and that the correct way of the local field effect calculation is not trivial [70]. Similarly, the LDOS is modified in the inhomogeneous environment, such as the metallic resonant structure in the vacuum [71–73]. Here, the dyadic Green's function consists of the vacuum part plus a contribution rising from scattering on the inhomogeneities. Depending on the geometrical arrangement, the environment can both increase or decrease the LDOS due to constructive (destructive) interference effects. Simplest possible example of this is a LDOS dependence on height above a perfect metal surface, where a clear interference of the scattered dyadic Green's function with the vacuum part leads to modulation with period corresponding to the light wavelength [19, 74].

The LDOS and its modification by means of metallic structure nano-fabrication has application potential in enhancement of weakly luminescent object's mission, such as quantum dots [75], or increase of sensor sensitivity to biomolecules with photoluminescent labels. In the following, we will continue in our discussion of the near-field scanning probe imaging techniques and focus on two selected state-of-the-art methods employing the photoluminescence.

4.2 Scanning probe imaging techniques based on photoluminescence

The fluorescent imaging of surface plasmons belongs to one of oldest methods exploited in nano-optics. We will focus in this section on two of the most prominent novel methods which are combining advantages of the scanning probe and spontaneous emission for mapping of near-field properties of metallic structures.

4.2.1 Scanning fluorescence lifetime imaging

In order to understand better the influence of LDOS on spontaneous emission it is important to have an experimental tool capable of LDOS spatial mapping. One of

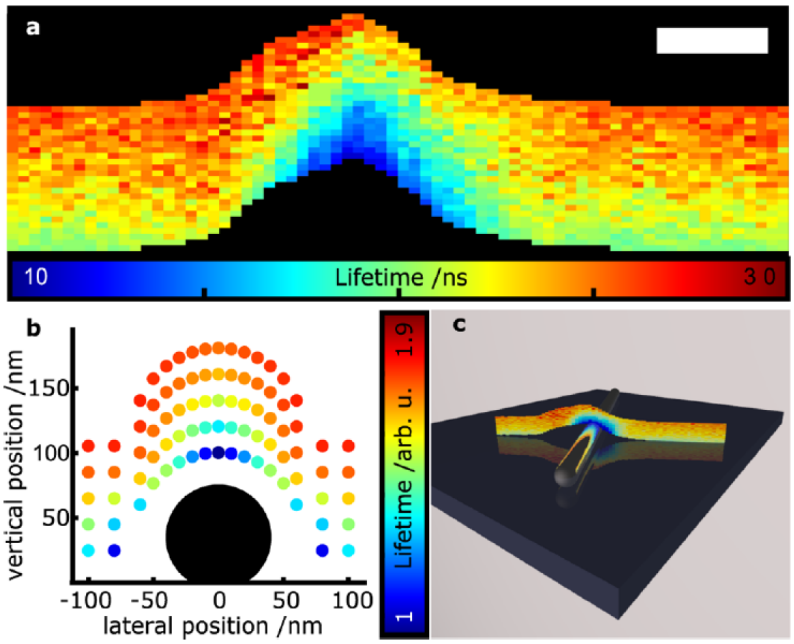

Figure 4.2: Fluorescence lifetime map in the vicinity of a metallic (silver) wire captured in position marked in c). Figure a) shows an experimental image obtained from a scan over the wire. The image exhibits short lifetimes, hence huge decay rate, in the vicinity of the wire. The scalebar is 100 nm. b) Theoretical calculation utilizing formula (4.1) in slightly modified form accounting for presence of the tip is in a good agreement with the experiment. Figure taken from [76].

such tools is a high resolution scanning transmission electron microscope equipped with electron energy analyser and monochromator – the HREELS [40–42]. The interpretation of the HREELS measurements is not that straightforward, as was shown by Hohenester [41], and the electron loss maps generally slightly differ from the LDOS. A direct way of LDOS mapping utilizes the enhancement of the spontaneous emitter radiative decay rate as described by equation (4.1). In the recent paper Schell et al. [76] presented a method for measurement of the single nitrogen vacancy lifetime $\tau = 1/\gamma$ in nanodiamond. The vacancy was glued to the apex of an AFM tip and scanned over a silver nanowire.

The fluorescence lifetime of the vacancy was measured by a synchronous pulsed detection scheme simultaneously in all vertical positions of the tip oscillations. The tapping mode of scanning was used to cover sufficient height above the wire. The fluorescent lifetime was fitted to the measured data during the scan. More details of the detection scheme are described in the original paper. The results of reference [76] are depicted in Figure 4.2. The measured lifetime strongly varies in the vicinity of the measured nanowire. In the close proximity of the wire, short lifetimes are observed. The shorter lifetime results here due to increased LDOS close to the nanowire surface which is triggered by available higher order nanowire plasmonic modes.

This effect is well known and is related to the so called electromagnetic photoluminescence quenching. The electromagnetic quenching emerges as rapid decrease of the

far-field molecular fluorescent radiation due to presence of higher order non-radiative (dark) electromagnetic modes of the metallic structure. Once the molecule decays close to the metal surface, most of the radiated energy flows to the dark modes, being absorbed in the metal and converted to heat. This leads to strong decrease of the radiation signal in the far-field. The lifetime imaging, however, overcomes the quenching, because the measured quantity is not directly the electromagnetic field intensity, but its time profile which is after the excitation given by the rate equation [19]

$$\frac{\mathrm{d}N_{\mathrm{ex}}}{\mathrm{d}t} = -\gamma N_{\mathrm{ex}}, \tag{4.4}$$

Where N_{ex} denotes the occupancy of the vacancy excited state and $\gamma = 1/\tau$ is the decay rate. The detected intensity is proportional to the occupancy of excited state N_{ex} by a factor of the so called quantum yield Q defined as a ratio of the energy flow to the far-field to the total energy dissipation of the emitter. The rate equation must be understood in the statistical sense, where an ensemble of identical systems is studied, hence, the N_{ex} is averaged occupancy of the excited state over a large set of samples or identical successive measurements and can have non-integral values.

The mapping of the LDOS is important not only for validation of the considered physical model for the spontaneous emission of molecules and atoms in the vicinity of metallic structures, but also for practical applications in the field of enhanced fluorescent spectroscopy.

In the next section, we will mention another method based on photoluminescece, this time the photoluminescence of metals.

4.2.2 Gold photoluminescence SNOM

The SNOM technique utilizing the photoluminescence has been introduced in reference [53]. The authors present here a gold tip of SNOM as a tool for generation of the photoluminescent signal that is spectrally red shifted away from the elastically scattered light. The spectrally shifted light is exploited for separation of the signal coming solely from interaction of the tip with the metallic structures and the directly scattered light as depicted in Figure 4.3.

The key principle driving this method is the ability of the gold structures to produce the luminescent radiation enhanced by surface plasmons. Such structure is in this case the very apex of the microscope tip. The process of the metal photoluminescence enhanced by plasmon excitation is not well understood so far. A huge amount of papers, especially experimental ones, has been written about the plasmon enhanced gold single photon and two photon induced photoluminescence [77–84]. A strongly enhanced photoluminescent signal has been observed which overwhelms the signal from flat gold interfaces in many orders of magnitude. The spectral response of the metal nanoparticles that support localized plasmon modes showed photoluminescence spectrum strongly pronounced in the region close to the frequency of the plasmon resonance. This experimental observation led to conclusion that the plasmon resonance mediates the interband radiative transition in the metal.

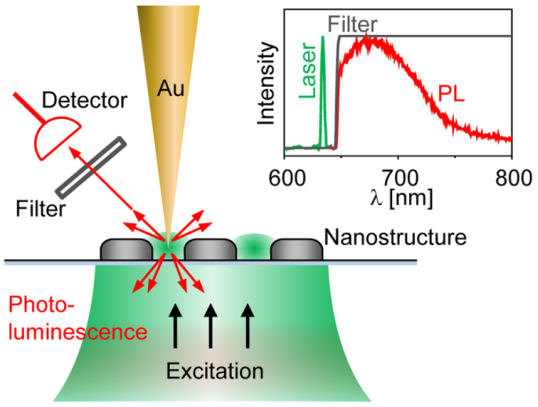

Figure 4.3: Schematic of the SNOM based on the photoluminescence of gold. The gold tip is illuminated by the incident radiation enhanced by the detected structure. The tip emits the spectrally shifted light which is separated from the elastic light by the optical edge filter. The tip emission is enhanced by presence of the detected metallic structure. The sample metallic structure plays a double role in the ehancement of the tip photoluminescence which enables the detection of the weak tip photoluminescence signal. The image is taken from reference [53].

Following the experimental findings including the loss of light polarization and coherence, a theoretical formulation of a possible enhancement mechanism was proposed. According to references [83,84], the photluminescent signal should emerge as stochastic absorption and emission of point-like centres all over the metallic particle. The emission connected with the localized transition takes place under influence of the vacuum fluctuation of the plasmonic and photonic modes whose impact is condensed in the LDOS. The rate of photons emitted to the far-field will then be found as the absorption rate multiplied by the quantum efficiency of emission (the radiative decay rate divided by the total non-radiative rate) averaged over the volume of the particle. The quantum efficiency also follows from the energy considerations as a ratio of corresponding radiated power to the total power released by the transition. The far-fields will emerge dominantly from emission of the particle dipole mode, hence, the dipole resonance is of a special importance for the far-field observations. A surprisingly good agreement of theory with experiment was found in reference [82], where the single photon photoluminescence of gold nanorods was studied. The authors considered the emission signal as a bulk gold photoluminescence spectrum (intrinsic property of the metal) multiplied by the frequency dependent anisotropic polarisability of the antenna and the incident electric field. Even though the microscopic mechanism of the gold photoluminescence is still unclear, the proposed simple model sufficiently grasps the resulting effects of plasmon resonances.

In the gold photoluminescence SNOM, the tip serves as the photoluminescent center which is embedded in the environment formed by the sample. The sample can be any metallic structure which does not exhibit photoluminescence in the gold photoluminescence spectrum (which is approximately in the region between 500 nm to 700 nm). The tip is supposed to have a relatively flat resonance in the desired

region and the enhancement of the emission is mediated dominantly by the sample in a twofold way. First, the incident light is enhanced by the sample resonances, increasing the absorption of the tip, and second, the emission of the tip takes place in the environment with enhanced LDOS. The spectral range of the gold photoluminescence allows the use of illumination light with wavelength 633 nm, which is the conventional He-Ne laser wavelength.

This mechanism has been successfully exploited for near-field mapping of metallic structures illuminated by beams of different polarization. The results of the near-field measurement performed in reference [53] are depicted in Figure 4.4. The SNOM technique based on the gold photoluminescence is able to map the hot spots of the metallic structures in accordance with theoretical predictions. The appropriate patterns are obtained for both of the different polarization illuminations, one when the polarization of the incident beam is circulating around the beam center (azimuthal light polarization) and the other one when the beam is polarized radially.

The photoluminescence of gold was able to replace the technically challenging method of interferometric detection an map the near-field of the metallic structures. The incoherent process of photoluminescence, on which the technique is based, unfortunately disables the phase resolved experiments. This is a serious drawback of the method restricting its practical use in comparison with methods based on coherent scattering.

In conclusion, we showed in this chapter that the phenomenon of photoluminescence is suitable for imaging of near-field properties of metallic nano-structures. The mechanism of photoluminescence serves either as a tool for mapping of a different near-field quantity, the LDOS, or simply as a tool for separation of the signal scattered by the tip towards the detector from the overall elastically scattered background light.

Even though the novel near-field microscopy techniques are promising in applications, the conventional s-SNOM utilizing interferometric detection, which was discussed in the previous chapter in detail, holds irreplaceable position among other imaging techniques. Especially the applications of metallic structures in infrared and ability of phase resolution make of the conventional s-SNOM an important tool for the near-field mapping and engineering of infrared antenna's near-field properties. We will end here our excursion to the field of scanning probe imaging techniques and return to the studied linear infrared antennas in the following chapter. We will present their practical application in the prominent field of surface enhanced vibrational spectroscopy. Our attention will focus mostly to the surface enhanced infrared spectroscopy, where the properties of the linear antennas are widely exploited.

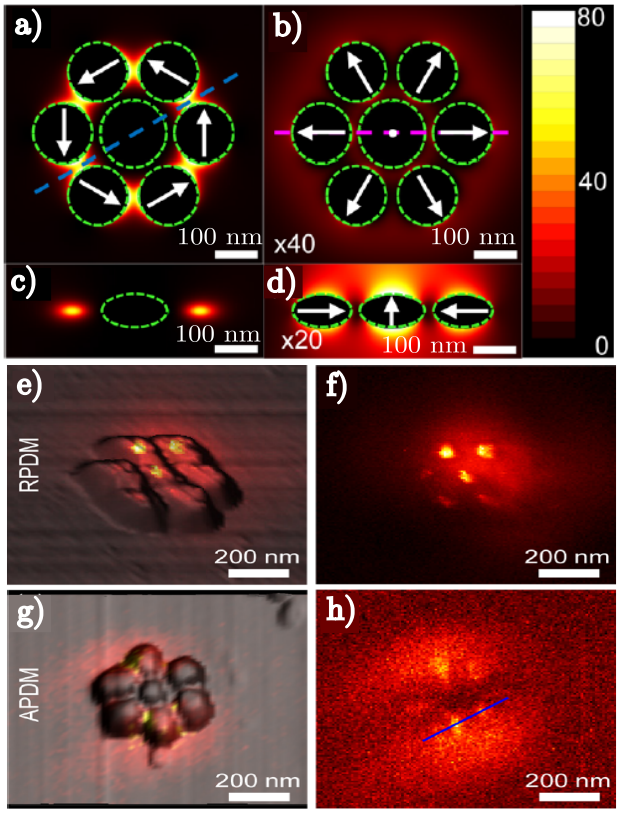

Figure 4.4: The results of reference [53]. Figures a) and b) depict the simulated near-field enhancement in a horizontal cross-section through the metallic disc structures illuminated by light polarized according to the white arrows. In d) and c) the vertical simulated field enhancement profiles marked by the dashed lines in figures above [a) pairs with c) and b) with d)] are depicted. Figures e) to h) depict experimental results. The results obtained with the radial polarization of the incident beam (RPDM) are shown in figures e) and f). The results for illumination by azimuthally polarized beam (APDM) are depicted in g) and h). In e) the experimental signal is matched with the topography image as well as in g). A laser illumination of wavelength 633 nm has been utilized.

5 | Surface enhanced vibrational spectroscopy

One of the most prominent applications of the electromagnetic near-field enhancement achieved in the proximity of the micro- and nano-scale metallic objects is the all optical detection and analysis of different chemical substances in even attomolar concentrations [7, 10, 85]. The incredibly high sensitivity of the spectroscopies enhanced by the metallic structures is a potential gate towards the early diagnosis methods and is of high importance in the field of chemical and biological analysis in general (e.g. [86]).

Historically, the enhancement effect was first observed in the Raman spectroscopy taking place on the rough surfaces [17, 63, 87], which led to immediate investigation of the enhancement mechanism and its potential tailoring possibilities. Nevertheless, even though the effect of surface enhanced spectroscopy is known for long years, only recently the nano-fabrication technologies reached sufficiently high level to enable intentional modification of metallic structures on nano-scale. Nowadays, it is possible to manufacture structures providing large near-field enhancement in the desired region of electromagnetic spectrum which leads to the controlled role of the electromagnetic enhancement effects in the interaction between the analyte and the metallic structure. The improvement of the technology enables one to perform experiments under precisely defined conditions, which opens the path towards quantitative evaluation of the surface enhanced spectroscopies.

The quantitative characterization, however, will never be possible without deeper understanding of the enhancement mechanism. Here we need to distinguish between basically two realizations of the surface enhanced vibrational spectroscopy, the surface enhanced Raman spectroscopy (SERS) and the surface enhanced infrared spectroscopy (SEIRS) [12]. The latter one can be found throughout the literature under different name, the surface enhanced infrared absorption (SEIRA). In this thesis, we will refer to the spectroscopy as to SEIRS, because the name does not implicitly infer any microscopic mechanism of enhancement.

Surface enhanced Raman scattering

SERS is basically just a modification of the well known inelastic coherent process called the Raman scattering. The probing incident electromagnetic radiation is usually set in the visible part of the spectrum and once it arrives to the molecule, it scatters either elastically in the form of the Rayleigh scattering or inelastically as the Stokes and the anti-Stokes scattering. The Rayleigh scattering forms the wast

majority of the signal, however, it does not carry the sample vibrational fingerprint. The characteristic information about the analysed sample, namely its vibrational properties, is hidden in the inelastically scattered light. The frequency of the Stokes and anti-Stokes lines are shifted with respect to the elastic light by a frequency which reflect the vibrational states of the analysed molecule. From the quantum mechanical perspective, the inelastic scattering process may be treated in the second order of the perturbation theory, which includes transition from the initial state possessing n_i phonons (hence quanta of vibrations) to the final state, which differs from the initial state just by the number of phonons by $\Delta n = n_\mathrm{f} - n_\mathrm{i} = \pm 1$, through all possible intermediate vibronic[1] states.

If the phonon is lost during the process[2] ($\Delta n = -1$), one obtains the anti-Stokes scattering which results in photon of slightly higher frequency than the elastic photon. The Stokes line emerges from the process, where one phonon is created during the scattering, hence the scattered photon frequency must be decreased by the amount of the vibrational frequency of the created phonon. An important note is that the Raman scattering is in principle a scattering on the electronic structure of the analysed molecule. The vibrational modes of the molecule enter the scattering process only indirectly. This can be seen by considering the Raman scattering process from the classical point of view, where the polarizabiliy of the molecule depends on the generalized coordinates of the nuclei. We can generally write the scattered signal by means of the molecular polarizability in virtue of the dipole radiation formula:

$$E_\mathrm{sca}(t) \sim \alpha\left(Q(t)\right) E_\mathrm{inc} \cos \omega_\mathrm{inc} t, \tag{5.1}$$

where the scattered light E_sca is connected to the incident light E_inc by a slowly varying polarizability $\alpha\left(Q(t)\right)$, which is a function of the time dependent generalized coordinate of the nuclei $Q(t)$. By employing the Taylor expansion of the polarizability $\alpha\left(Q(t)\right)$ with respect to the generalized coordinate $Q(t)$ and considering the time harmonic dependence of the molecular oscillation $Q(t) = Q_0 \cos \Omega t$ we get

$$E_\mathrm{sca}(t) \sim \alpha(0) E_\mathrm{inc} \cos \omega_\mathrm{inc} t + \left.\frac{\partial \alpha}{\partial Q}\right|_{Q=0} Q_0 E_\mathrm{inc} \cos \Omega t \cos \omega_\mathrm{inc} t + ... \tag{5.2}$$

Here the product of the two cosines yields the terms corresponding to the inelastic processes, which have amplitude proportional to the derivative of the polarizability α with respect to the generalized nuclear coordinate Q. The selection rules for the Raman spectroscopy can be derived accordingly. We obviously see that the vibrational modes contributing to the Raman signal have to cause change in the electronic polarizability. This is basically the main criterion which decides about realization of the usual Raman process.

In SERS, however, the situation is slightly different. The molecule does not interact solely with the travelling incident wave, but the interaction with the incident light is mediated by scattering on the metallic structure. The near-field enhancement caused by the scattering of the incident plane wave on the nano-structure,

[1] Vibronic states comprise both the electronic and the vibrational state.

[2] Generally one or more.

together with enhancement of the radiation scattered from the molecule, is known in the literature as the electromagnetic enhancement effect [15, 16, 88]. Quantitative evaluation of the electromagnetic enhancement is not a simple task, because one has to know precisely the scatterer geometry on the microscopic level, including the slight surface roughness on the molecular scale. The precise knowledge of the local field enhancement is, however, crucial for correct quantitative analysis. Very roughly, we can estimate the effect of the double enhancement by considering the measured Raman signal enhancement as a product of the field enhancement connected with the scattering of the incident light and the enhancement calculated for the slightly frequency-shifted outgoing signal. In a good approximation, the enhancement at the two distinct frequencies can be considered as equal and we get the well known fourth power formula for the electromagnetic Raman enhancement [15–17, 63]

$$I_{\mathrm{Raman}} \sim \left| \frac{E_{\mathrm{sca}}}{E_{\mathrm{inc}}} \right|^4 . \tag{5.3}$$

Usual values of the near-field enhancement $|E_{\mathrm{sca}}|/|E_{\mathrm{inc}}|$ can be found in the order of 10-100. The Raman electromagnetic enhancement factors can be therefore roughly estimated to be of the order of $10^4 - 10^8$. The above described mechanism of Raman signal enhancement did not succeed in interpretation of even much higher experimentally obtained enhancements for molecules directly adsorbed to the metal surface. Here, another mechanism which originates in the electronic interaction of the molecule and the metal must be taken into account. The so called electronic mechanism[3] is similar to the resonant Raman scattering [89], where the incident light has frequency close to the internal molecular electronic transition. In SERS, the resonant transition does not originate simply from the electronic structure of a single molecule, but it appears as a mutual interaction of the molecular electronic states and the electronic states of the metallic structure [15, 16]. The electronic mechanism generally leads to different selection rules than the non-resonant Raman scattering and because of its origin in electronic interaction between the molecule and the metal, it can be seriously influenced by the surface chemical modification [15, 16].

The SERS and its scanning probe modification TERS (tip enhanced Raman spectroscopy) attained a variety of practical applications [90–92] and especially in the detection sensitivity overwhelmed a current performances of SEIRS.

Surface enhanced infrared spectroscopy

The SEIRS takes advantage of the infrared electromagnetic near-field enhancement close to a micrometer-sized metallic objects, relying on an elastic scattering between the probing metallic object and the analysed sample [65]. On the way towards the single molecule detection, a lot of effort has been spent on improvement of the SEIRS sensitivity by utilizing innovative infrared antenna shapes possessing high near-field enhancements in the hot spots, which provide strong interaction between the antenna and the sample. The concept of the linear infrared antennas has proven

[3] The mechanism is also called the charge transfer mechanism, the electronic mechanism or the chemical mechanism and sometimes even the first layer enhancement mechanism, since it mostly affects only the first monolayer of the analyte.

useful for its simplicity and possibility of constructing structures such as the linear dimer antennas [11, 13]. As we have shown in section 3.2.2, the antenna dimer provides a strong field enhancement in the gap regions which might even reach a value over 100 [65]. In a close analogy to the single linear antenna, the linear antenna cross [14] provides similar field enhancements in the central gap regardless of the incident light polarization.

Mechanism of the SEIRS is rather different from SERS. The SEIRS is triggered by direct interaction of the infrared light and the vibrational modes of the sample. Due to a spectral overlap of the metallic structure (infrared antenna) resonance and the sample vibrational resonance, the spectral line shapes of SEIRS exhibit interference features very similar to those known from quantum physics, such as an electromagnetically induced transparency (EIT) or absorption (EIA). Following the quantum mechanical analogue [93], the SEIRS spectra are also often described in terms of the Fano-like resonances, where a pseudo-continuum of electromagnetic modes, represented by a broad dipole resonance of the infrared antenna, interferes with a narrow vibrational resonance of the analyte [12, 85, 94, 95].

The essential mechanism of SEIRS, an elastic interaction between the antenna mode and the mode of the sample, also implies dependence of the SEIRS spectral features on the sample geometrical shape. The sample formed in a shape of a sphere might interact with the antenna through different electromagnetic modes than for example a thin layer closely attached to the antenna surface. Such peculiarities must be carefully taken into account for correct interpretation of the SEIRS spectra. Recently, it has been shown that the interference behaviour observed in SEIRS can be modelled by a set of coupled oscillators (a classical forced damped mechanical oscillator analogue) under radiation conditions [96]. It was pointed out that different ratios of a radiative to a non-radiative (intrinsic) damping can lead to either EIT or EIA effects.

In this thesis, we will exploit properties of the infrared antennas presented in section 3.2.2 and their application in the field of infrared spectroscopy. We will present a theoretical description of the purely electromagnetic effect responsible for SEIRS signal enhancement and formation of Fano-like interference. Our conclusions will be supported by a simple example of a linear dipole antenna interacting with a material with well known vibrational properties – the SiO_2.

In the next section, we will briefly review the concept of the Fano-like resonances which is widely used in plasmonics. Our analytical model will result in section 5.2 as a generalization of the concept of the coupled harmonic oscillators, naturally extended by the interaction with radiation through the general electromagnetic theory of scattering. In section 5.3 we will apply our model to the particular examples.

5.1 Fano-like resonances

When in 1961 Ugo Fano presented his theory of *Effects of Configuration Interaction on Intensities and Phase Shifts* [93], he set a general base for treatment of spectral line shapes commonly found in different disciplines of physics, among others also the electromagnetic response of structures belonging to the field of nano-optics and plasmonics. It is the obvious similarity between the theory of quantum mechanics

and the classical electromagnetism which allowed the application of the so called Fano-resonances on interacting system of optical modes.

The original paper by Fano deals with the problem of inelastic electron scattering on a helium atom. The effect of the asymmetric line shape of the scattering spectrum is then explained by interference effect between a discrete state, which is responsible for resonant interaction of the incident electron with the atom, and a continuum of states, which gives rise to the background scattering. The amplitude of the scattering attributed to the interaction with the discrete state varies abruptly around the discrete state eigenenergy in both phase and amplitude. On the other hand, the continuum spectrum is slowly varying and its phase remains constant over the region where its spectrum overlaps with the discrete state. Once the two scattering amplitudes are combined, the asymmetric scattering spectral profile is obtained. Fano derived a general formula for spectral line shape of this class of interactions, which can be generally written in form

$$\sigma = \frac{(q+\epsilon)^2}{1+\epsilon^2}, \tag{5.4}$$

where q is the so called asymmetry parameter and ϵ is the reduced energy variable defined by

$$\epsilon = \frac{E - E_\mathrm{d} - F}{\frac{1}{2}\Gamma}.$$

Here E is the energy where the expression is evaluated, E_d is the energy of the discrete state, F is the correction for the discrete state energy due to the coupling with the continuum and Γ is the linewidth of the discrete state [93]. The model parameters can be obtained for some particular situation from calculation according to formulas given in the paper [93] or can be fitted to experimental data and serve as a tool for quantitative analysis.

The problem of electromagnetic scattering on systems where two electromagnetic modes interact with the incident light and whose spectra mutually overlap can be dealt along similar lines as the quantum mechanical case. In a standard configuration, one of the interacting modes is a bright mode of the resonant structure, hence the mode which strongly interacts with the incident light, by which its characteristic wide absorption spectrum is triggered. The bright mode therefore effectively plays the role of the quantum mechanical state continuum. The discrete state is in the electromagnetic analogy substituted by a narrow resonance of the so called dark mode, which only weakly interacts with the incident light, but which couples with the bright mode. Mathematical treatment of such a scattering problem yields a formula which resembles the form of the Fano spectrum. By means of a rigorous description of the scattering via Feshbach formalism, Gallinet and Martin derived the spectral line shape [94]

$$\sigma = a\frac{(\kappa+q)^2 + b}{1+\kappa^2}, \tag{5.5}$$

where the parameter κ plays a role of reduced frequency similarly as ϵ in the original Fano formula. Here q is the asymmetry parameter, which is given by ratio of

the optical response of the continuum, represented by the wide resonance, and the response of the narrow dark mode. Parameter a is an amplitude which is related to the intrinsic damping parameter and b is a parameter influencing contrast of the spectral resonance which also depends with the intrinsic damping of the system. More details about the parameters are provided in the original paper [94].

Here, we only focus on the influence of the parameters on the shape of the resulting Fano spectrum σ. Figure 5.1 shows normalized Fano-like lines calculated according to (5.9). The spectral dependence is obviously strongly influenced by the asymmetry parameter q, which changes the shape of the spectrum from a totally symmetric dip for $q = 0$ through a typical asymmetric Fano line shape for $q = 1$ to a symmetric peak when $q \to \infty$. The parameter b only affects the contrast of the spectrum, but does not play any role in formation of the asymmetry. We kept $b = 0.5$ in calculation of the spectral line shapes.

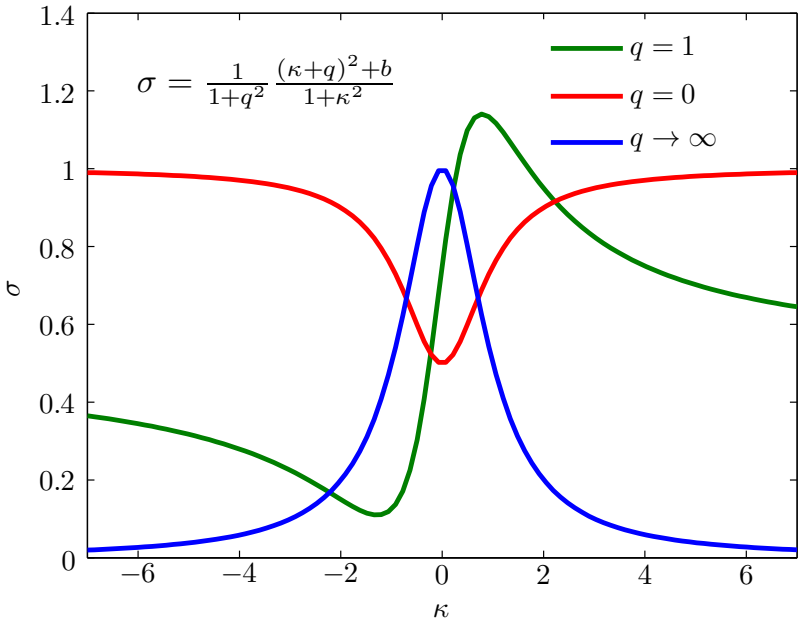

Figure 5.1: Normalized Fano-like profile plotted for different asymmetry parameters. $q = 1$, $q = 0$ and $q \to \infty$. In all cases the parameter $b = 0.5$ was set. For $q = 1$ the typical asymmetric spectrum is obtained. The extreme values of q yield either a symmetric dip in the continuum for $q = 0$ or a symmetric resonance of the discrete state with absence of the continuum for $q \to \infty$ ($q = 1000$ was used in the calculation).

Let us clarify the interference process described above on a simple example of two coupled harmonic oscillators which fulfil the conditions for appearance of the Fano-like resonance. One of the two oscillators must have a wide resonance spectrum which emulates properties of the bright electromagnetic mode of the resonant structures, the other one must be tightly peaked around its resonant frequency in analogy with the dark electromagnetic mode. The oscillator supplying the bright mode is furthermore driven by an external force (having spectral amplitude f), which in the

electromagnetic case represents the interaction with incident radiation. The situation is mathematically described by a set of coupled equations for displacements of the two oscillators $x_{\mathrm{b(d)}}$ characterized by resonant frequencies $\omega_{\mathrm{b(d)}}$, damping parameters $\gamma_{\mathrm{b(d)}}$ and coupling strength g, where indices b(d) denote the bright (dark) mode. The set of equations reads

$$\frac{\mathrm{d}^2 x_\mathrm{b}}{\mathrm{d}t^2} + \gamma_\mathrm{b}\frac{\mathrm{d}x_\mathrm{b}}{\mathrm{d}t} + \omega_\mathrm{b}^2 x_\mathrm{b} + g x_\mathrm{d} = f\exp\left(-\mathrm{i}\omega t\right), \tag{5.6}$$

$$\frac{\mathrm{d}^2 x_\mathrm{d}}{\mathrm{d}t^2} + \gamma_\mathrm{d}\frac{\mathrm{d}x_\mathrm{d}}{\mathrm{d}t} + \omega_\mathrm{d}^2 x_\mathrm{d} + g x_\mathrm{b} = 0. \tag{5.7}$$

Considering a time harmonic dependence of displacements $x_{\mathrm{b(d)}} = a_{\mathrm{b(d)}}\exp\left(-\mathrm{i}\omega t\right)$, the solution for the bright mode amplitude can be found

$$a_\mathrm{b} = \frac{\omega_\mathrm{d}^2 - \mathrm{i}\gamma_\mathrm{d}\omega - \omega^2}{\left(\omega_\mathrm{b}^2 - \mathrm{i}\gamma_\mathrm{b}\omega - \omega^2\right)\left(\omega_\mathrm{d}^2 - \mathrm{i}\gamma_\mathrm{d}\omega - \omega^2\right) - g^2} f. \tag{5.8}$$

By following the procedure of reference [94], parameters for the spectral line shape can be obtained from (5.8) by calculating

$$\frac{\left|a_\mathrm{b}\right|^2}{\left|A\right|^2} = \sigma = \frac{(\kappa+q)^2 + b}{1+\kappa^2},, \tag{5.9}$$

where $|A|^2 = |f|^2/|C|^2$ with $C = \omega_\mathrm{b}^2 - \mathrm{i}\gamma_\mathrm{b}\omega - \omega^2 \approx \omega_\mathrm{b}^2 - \mathrm{i}\gamma_\mathrm{b}\omega_\mathrm{d} - \omega_\mathrm{d}^2$ in the region close to the resonant frequency of the dark mode. The parameters can be evaluated by rearrangement of terms and neglecting second order contributions of the damping parameters [94]

$$\kappa = \frac{\omega^2 - \omega_\mathrm{d}^2 - \omega_\mathrm{d}\Delta}{\Gamma}, \tag{5.10}$$

$$q = \frac{\omega_\mathrm{d}^2 - \omega_\mathrm{b}^2}{\gamma_\mathrm{b}\omega_\mathrm{d}}, \tag{5.11}$$

$$b = \frac{\gamma_\mathrm{d}^2|C|^2}{\gamma_\mathrm{b}^2 g^4}, \tag{5.12}$$

where $\Delta = \left[(\omega_\mathrm{d}^2 - \omega_\mathrm{b}^2)g^2\right]/(|C|^2\omega_\mathrm{d})$ and $\Gamma = \gamma_\mathrm{b}\omega_\mathrm{d}g^2/|C|^2$. We see that the simple example of coupled harmonic oscillators yields the Fano-like spectrum, though the final formulas are not much transparent. In the following we will show, how the formalism of the coupled oscillators can be applied on a system of electromagnetically coupled objects, which is a situation commonly found in SEIRS. A notable difference between the simple coupled harmonic oscillator model and the electromagnetic case will arise from the coupling of the bright resonant modes with radiation.

5.2 Generalized polarizability in SEIRS

In practical applications, we always need to calculate the realistic response, such as the absorption, scattering or extinction spectrum [97, 98], which can be accessed by

different experimental techniques. For example, the extinction spectrum which corresponds to the energy drained away from the primary beam is commonly measured in most SEIRS transmission experiments. On the other hand, the scattering spectrum, being the total energy radiated by the induced dipole of the antenna, is mostly accessed in reflection experiments using the dark-field microscope objectives. Direct measurement of the absorption spectrum, hence ohmic losses in the antenna, is still possible only with difficulties, even thought some technique for similar measurement has been developed and applied in connection with s-SNOM set-up [99]. Especially for relatively large infrared antennas, these spectra are manifestly distinct and only calculating one of them does not provide full information on the resonant system response.

Complete picture of the antenna-sample scattering process can be obtained from a full electrodynamic treatment based on a formal solution of the volume integral equation in analogy with equations (3.19) and (3.20). The volume integral equation

$$\mathbf{E}(\mathbf{r}) = \mathbf{E}_{\text{ext}}(\mathbf{r}) + k^2 \int \mathbf{G}(\mathbf{r}, \mathbf{r}') \cdot \boldsymbol{\chi}(\mathbf{r}') \cdot \mathbf{E}(\mathbf{r}') \mathrm{d}\mathbf{r}' \tag{5.13}$$

self-consistently relates the electric field in an arbitrary point $\mathbf{r}$ of space to an external stimulation $\mathbf{E}_{\text{ext}}$ and a dielectric environment with electric susceptibility $\boldsymbol{\chi}(\mathbf{r})$ via electric dyadic Green's function $\mathbf{G}(\mathbf{r}, \mathbf{r}')$ and a vacuum wave number k. In SEIRS, we are left with two different dielectric bodies: the metallic antenna (A) and the probed sample (S). Hence, (5.13) can be written as a set of coupled integral equations

$$\mathbf{E}(\mathbf{r}_{\text{A}}) = \mathbf{E}_{\text{ext}}(\mathbf{r}_{\text{A}}) + k^2 \int \mathbf{G}(\mathbf{r}_{\text{A}}, \mathbf{r}') \cdot \boldsymbol{\chi}(\mathbf{r}') \cdot \mathbf{E}(\mathbf{r}') \mathrm{d}\mathbf{r}', \tag{5.14}$$

$$\mathbf{E}(\mathbf{r}_{\text{S}}) = \mathbf{E}_{\text{ext}}(\mathbf{r}_{\text{S}}) + k^2 \int \mathbf{G}(\mathbf{r}_{\text{S}}, \mathbf{r}') \cdot \boldsymbol{\chi}(\mathbf{r}') \cdot \mathbf{E}(\mathbf{r}') \mathrm{d}\mathbf{r}', \tag{5.15}$$

where $\mathbf{r}_{\text{A}}$ ($\mathbf{r}_{\text{S}}$) stands for positions inside of the antenna (the sample).

We will proceed by making an assumption that the Green's functions can be decomposed into the quasi-static part and a part which is responsible for the radiation damping. By this we seek the solution of the coupled equations in the radiation corrected quasi-static regime. We will rewrite the equations in a shorthand bra-ket operator notation following the treatment of reference [100]

$$|\mathbf{E}_{\text{A}}\rangle = |\mathbf{E}_{\text{ext}}\rangle + \hat{\mathbf{G}}^{\text{st}}_{\text{AA}}|\mathbf{E}_{\text{A}}\rangle + \hat{\mathbf{G}}^{\text{st}}_{\text{AS}}|\mathbf{E}_{\text{S}}\rangle + \hat{\mathbf{G}}^{\text{rad}}_{\text{AA}}|\mathbf{E}_{\text{A}}\rangle, \tag{5.16}$$

$$|\mathbf{E}_{\text{S}}\rangle = |\mathbf{E}_{\text{ext}}\rangle + \hat{\mathbf{G}}^{\text{st}}_{\text{SS}}|\mathbf{E}_{\text{S}}\rangle + \hat{\mathbf{G}}^{\text{st}}_{\text{SA}}|\mathbf{E}_{\text{A}}\rangle + \hat{\mathbf{G}}^{\text{rad}}_{\text{SS}}|\mathbf{E}_{\text{S}}\rangle. \tag{5.17}$$

The operators $\hat{\mathbf{G}}^{\text{st}}_{\text{AA(SS)}}$ stand for the self interaction part of the integral considering only the quasi-static Green's function, $\hat{\mathbf{G}}^{\text{st}}_{\text{AS(SA)}}$ are the operators mediating the mutual interaction between the antenna and the sample and $\hat{\mathbf{G}}^{\text{rad}}_{\text{AA(SS)}}$ is the operator which is responsible for the interaction of the antenna (sample) modes with the radiation fields. We make use of the hermiticity of the quasi-static self interaction operator when the complex susceptibility is excluded from the integral and define the eigenmodes of the two operators $\hat{\mathbf{G}}^{\text{st}}_{\text{AA(SS)}}$ on the volume occupied by the antenna or the sample as [100]

$$\hat{\mathbf{G}}^{\text{st}}_{\text{AA}}|\mathbf{e}_i\rangle = \chi_{\text{A}}\beta_i|\mathbf{e}_i\rangle, \tag{5.18}$$

$$\hat{\mathbf{G}}^{\text{st}}_{\text{SS}}|\mathbf{f}_i\rangle = \chi_{\text{S}}\gamma_i|\mathbf{f}_i\rangle. \tag{5.19}$$

We made use of the fact that the susceptibility is constant over the whole volume on which the integral is defined. The eignenmodes are supposed to fulfil the orthonormality conditions

$$\langle \mathbf{e}_i | \mathbf{e}_i \rangle = \int_{\mathrm{A}} \mathbf{e}_i^*(\mathbf{r}) \cdot \mathbf{e}_i(\mathbf{r}) \mathrm{d}\mathbf{r} = 1, \tag{5.20}$$

$$\langle \mathbf{e}_i | \mathbf{e}_j \rangle = 0, \; i \neq j. \tag{5.21}$$

With such definition of the eigenmodes, the solution of the electric fields inside of each object can be sought as a linear combination of the object eigenmodes $|\mathbf{E}_{\mathrm{A}}\rangle = \sum b_i |\mathbf{e}_i\rangle$ and $|\mathbf{E}_{\mathrm{S}}\rangle = \sum c_i |\mathbf{f}_i\rangle$ respectively. We further expect than only a single dipole mode will contribute to the antenna resonance. We will therefore consider only a single expansion term $|\mathbf{E}_{\mathrm{A}}\rangle = \sum b |\mathbf{e}\rangle$ for the antenna field. The coupled set of equations will reduce to the set of equations for respective coefficients

$$b = \langle \mathbf{e} | \mathbf{E}_{\mathrm{ext}} \rangle + \chi_{\mathrm{A}} \beta b + \sum_i c_i \langle \mathbf{e} | \hat{\mathbf{G}}^{\mathrm{st}}_{\mathrm{AS}} | \mathbf{f}_i \rangle + b \langle \mathbf{e} | \hat{\mathbf{G}}^{\mathrm{rad}}_{\mathrm{AA}} | \mathbf{e} \rangle, \tag{5.22}$$

$$c_i = \langle \mathbf{f}_i | \mathbf{E}_{\mathrm{ext}} \rangle + \chi_{\mathrm{S}} \gamma_i c_i + b \langle \mathbf{f}_i | \hat{\mathbf{G}}^{\mathrm{st}}_{\mathrm{SA}} | \mathbf{e} \rangle + \sum_j c_j \langle \mathbf{f}_i | \hat{\mathbf{G}}^{\mathrm{rad}}_{\mathrm{SS}} | \mathbf{f}_j \rangle. \tag{5.23}$$

Now, since we expect the sample modes which couple to the antenna to be dark modes, the coupling to the incident field $\langle \mathbf{f}_i | \mathbf{E}_{\mathrm{ext}} \rangle$ as well as the radiation correction term $\sum_j c_j \langle \mathbf{f}_i | \hat{\mathbf{G}}^{\mathrm{rad}}_{\mathrm{SS}} | \mathbf{f}_j \rangle$ will vanish (or at least will be small) in case of the sample modes and we will neglect them. We solve the set of equations (5.22) and (5.23) for the coefficient b by substituting the result for c_i from equation (5.23) to (5.22) and treating the antenna mode radiation correction term separately in the last step

$$b = \frac{\dfrac{\langle \mathbf{e} | \mathbf{E}_{\mathrm{ext}} \rangle}{1 - \beta \chi_{\mathrm{A}}} \dfrac{1}{1 - \sum\limits_i \dfrac{\langle \mathbf{e} | \hat{\mathbf{G}}^{\mathrm{st}}_{\mathrm{AS}} | \mathbf{f}_i \rangle}{1 - \beta \chi_{\mathrm{A}}} \dfrac{\langle \mathbf{f}_i | \hat{\mathbf{G}}^{\mathrm{st}}_{\mathrm{SA}} | \mathbf{e} \rangle}{1 - \gamma_i \chi_{\mathrm{S}}}}}{1 - \dfrac{\langle \mathbf{e} | \hat{\mathbf{G}}^{\mathrm{rad}}_{\mathrm{AA}} | \mathbf{e} \rangle}{1 - \beta \chi_{\mathrm{A}}} \dfrac{1}{1 - \sum\limits_i \dfrac{\langle \mathbf{e} | \hat{\mathbf{G}}^{\mathrm{st}}_{\mathrm{AS}} | \mathbf{f}_i \rangle}{1 - \beta \chi_{\mathrm{A}}} \dfrac{\langle \mathbf{f}_i | \hat{\mathbf{G}}^{\mathrm{st}}_{\mathrm{SA}} | \mathbf{e} \rangle}{1 - \gamma_i \chi_{\mathrm{S}}}}}. \tag{5.24}$$

We keep the formula in this form to stress the structure of the expression which will later result in the simple parametric coupled mode model. The electric field inside of the antenna will be in our approximation just the electric field of the antenna dipole mode multiplied by the constant b. The constant b is manifestly frequency dependent via the susceptibilities χ_{A}, χ_{S} and the radiation correction term $\langle \mathbf{e} | \hat{\mathbf{G}}^{\mathrm{rad}}_{\mathrm{AA}} | \mathbf{e} \rangle$. Before we interpret the result in (5.24) we must show how the generalized polarizability of a generic object O can be obtained. The generalized polarizability follows from equation of the type (5.22) when interaction with other objects is neglected. When the field is calculated following the lines of the previous derivation

$$|\mathbf{E}\rangle = c|\mathbf{e}\rangle = \frac{\dfrac{\langle \mathbf{e} | \mathbf{E}_{\mathrm{ext}} \rangle}{1 - \beta \chi_{\mathrm{O}}}}{1 - \dfrac{\langle \mathbf{e} | \hat{\mathbf{G}}^{\mathrm{rad}}_{\mathrm{OO}} | \mathbf{e} \rangle}{1 - \beta \chi_{\mathrm{O}}}} |\mathbf{e}\rangle, \tag{5.25}$$

the $i-$th dipole moment component of the particle mode is calculated by application of the dipole moment functional defined by

$$P_i\left[|\mathbf{E}\rangle\right] = \int_{\mathrm{O}} \varepsilon_0 \chi_{\mathrm{O}} \mathbf{n}_i(\mathbf{r}) \cdot \mathbf{E}(\mathbf{r}) \mathrm{d}\mathbf{r}. \tag{5.26}$$

The vector $\mathbf{n}_i(\mathbf{r})$ is a unit vector with direction of the probed dipole moment component. The integration, in other words, sums up all the elementary dipoles projected to the direction of the vector $\mathbf{n}_i(\mathbf{r})$ over the antenna volume. The total dipole moment is obtained by using the three orthogonal components of the dipole moment functional as coefficients of the electric field mode in the corresponding basis $\mathbf{n}_i$. The functional should be in generality applied to all possible modes of the antenna weighted by their respective coefficients. If we set the radiation correction term equal to zero, the expression (5.26) reduces to the quasi-static solution. In the point-like approximation and for a dipole mode with a constant internal field, such as the quasi-static sphere, the integration reduces to multiplication by the particle volume and the polarizability is obtained as

$$\alpha^{\mathrm{O}} \approx \frac{\langle \mathbf{e}|\mathbf{e}_{\mathrm{ext}}\rangle P\left[|\mathbf{e}\rangle\right]}{1-\beta\chi_{\mathrm{O}}} \approx \frac{\varepsilon_0 V_{\mathrm{O}} \chi_{\mathrm{O}}}{1-\beta\chi_{\mathrm{O}}}, \tag{5.27}$$

where $E_{\mathrm{ext}}|\mathbf{e}_{\mathrm{ext}}\rangle = |\mathbf{E}_{\mathrm{ext}}\rangle$ and the normalization condition for vector $|\mathbf{e}\rangle$ whose amplitude is proportional to $1/V_{\mathrm{O}}$ was used. The radiation corrected polarizability is afterwards straightforwardly derived using the value of the dyadic Green's function imaginary part at the origin and extracting the particle volume and susceptibility from the integration in a standard form [see expression (2.40)]

$$\alpha^{\mathrm{A}}_{\mathrm{rad}} = \frac{\alpha^{\mathrm{O}}}{1-\mathrm{i}\frac{k^3}{6\pi\varepsilon_0}\alpha^{\mathrm{O}}}. \tag{5.28}$$

Next we introduce the concept of the generalized polarizability. Obviously the integral which defines the polarizability functional can be simply extended to cases, when the object mode is not dipolar. The only difference is in the vector field $\mathbf{n}$ which now does not have to express the dipole field and can express any meaningful field distribution $\mathbf{n}(\mathbf{r})$ of the probing external field, fulfilling a proper normalization condition. For our further treatment, the particular normalization condition does not play a significant role since we are going to use the model as parametric. Only for completeness, we can state that the normalization condition can be of the form $\int_{\mathrm{O}} \mathbf{n}(\mathbf{r})\cdot\mathbf{n}(\mathbf{r})\mathrm{d}\mathbf{r} = V_{\mathrm{O}}$, which is fulfilled by the unit vector field used in the calculation of the usual dipole polarizability. The new vector field $\mathbf{n}(\mathbf{r})$ can be, for example, the external field of the antenna dipole mode, which is nothing else but the near-field distribution of the antenna. We make use of it to get a simplified parametric model expressing the total antenna polarizability[4] from the equation (5.24)

$$\alpha^{\mathrm{A}}_{\mathrm{tot}} = \frac{\alpha^{\mathrm{A}}_{\mathrm{non}}}{1-\mathrm{i}\frac{k^3}{6\pi\varepsilon_0}\,\alpha^{\mathrm{A}}_{\mathrm{non}}}, \tag{5.29}$$

[4]Equivalent relations can also be obtained for the sample generalized polarizability.

where the non-corrected resulting antenna polarizability $\alpha^{\mathrm{A}}_{\mathrm{non}}$ is defined by

$$\alpha^{\mathrm{A}}_{\mathrm{non}} = \frac{\alpha^{\mathrm{A}}}{1 - \alpha^{\mathrm{A}} G^{\mathrm{S}\to\mathrm{A}} \alpha^{\mathrm{S}} G^{\mathrm{A}\to\mathrm{S}}}. \tag{5.30}$$

Here α^{A} stands for the antenna polarizability without radiation corrections, α^{S} is the generalized polarizability of the sample, which reflects the intrinsic resonance of the sample mode as a response to the applied external field. Having the sample in a close proximity of the antenna, we introduced the coupling terms $G^{\mathrm{A}\to\mathrm{S}(\mathrm{S}\to\mathrm{A})}$, which are the model numerical parameters comprising the coupling effects between the sample modes and the antenna modes. The value of the coupling terms is closely related to the normalization of the external probing field $\mathbf{n}$. Using our normalization condition, we can estimate the value of the parameter with help of the effective coupling distance R_{eff} known from the interaction of two separate point dipoles as

$$G^{\mathrm{A}\to\mathrm{S}} = G^{\mathrm{S}\to\mathrm{A}} \approx \frac{1}{\varepsilon_0 R^3_{\mathrm{eff}}}. \tag{5.31}$$

Since the two parameters $G^{\mathrm{A}\to\mathrm{S}}$ and $G^{\mathrm{S}\to\mathrm{A}}$ appear in product, there is no necessity to distinguish their sign and it is possible to write the parameters in our model as real and positive.

The inclusion of the radiation damping [101] is the main difference of our model from the model of coupled harmonic oscillators used for description of the Fano-like resonances of metallic antennas resonant in the visible part of the spectrum (e.g. [102]). As the generalized polarizability can be reduced to usual frequency-dependent polarizabilities in the form of any physically meaningful function.

Once the polarizability of the antenna is known, the absorption, extinction and scattering spectra can be calculated from relations derived in references [98, 103]:

$$\sigma_{\mathrm{abs}} = \frac{k}{\varepsilon_0}\Im\{\alpha^{\mathrm{A}}_{\mathrm{non}}\}\left|\frac{\alpha^{\mathrm{A}}_{\mathrm{tot}}}{\alpha^{\mathrm{A}}_{\mathrm{non}}}\right|^2 + \frac{k}{\varepsilon_0}\Im\{\alpha^{\mathrm{S}}_{\mathrm{non}}\}\left|\frac{\alpha^{\mathrm{S}}_{\mathrm{tot}}}{\alpha^{\mathrm{S}}_{\mathrm{non}}}\right|^2 \approx \frac{k}{\varepsilon_0}\Im\{\alpha^{\mathrm{A}}_{\mathrm{non}}\}\left|\frac{\alpha^{\mathrm{A}}_{\mathrm{tot}}}{\alpha^{\mathrm{A}}_{\mathrm{non}}}\right|^2, \tag{5.32}$$

$$\sigma_{\mathrm{ext}} = \frac{k}{\varepsilon_0}\Im\{\alpha^{\mathrm{A}}_{\mathrm{tot}}\} + \frac{k}{\varepsilon_0}\Im\{\alpha^{\mathrm{S}}_{\mathrm{tot}}\} \approx \frac{k}{\varepsilon_0}\Im\{\alpha^{\mathrm{A}}_{\mathrm{tot}}\}, \tag{5.33}$$

$$\sigma_{\mathrm{sca}} = \sigma_{\mathrm{ext}} - \sigma_{\mathrm{abs}}, \tag{5.34}$$

where $\alpha^{\mathrm{S}}_{\mathrm{tot}}$ ($\alpha^{\mathrm{S}}_{\mathrm{non}}$) analogously to (5.29) [(5.30)] denotes the resulting generalized polarizability of the sample. The last approximation, neglecting the influence of the sample generalized polarizability, comes from the assumption that the antenna has much bigger polarizability than the sample, and therefore contributes to the absorption, scattering and extinction coefficients dominantly. This may not be always exactly true, but we will see that the effects of the antenna generalized polarizability are sufficient to describe the spectral behaviour. The definition of the scattering cross sections in equations (5.32) to (5.34) is strictly valid only for point-like polarizable objects, however, they can serve in our model as a good energy conserving approximation.

For purpose of practical calculations, it is necessary to determine the polarizabilities of the two interacting objects which is a rather difficult task in generality. We will use the polarizabilities of the objects entering our discussion in the form of

Lorentz oscillators. Similar approach has been successfully exploited for study of coupling between infrared antenna and substrate supporting phononic modes in reference [104]. This approximation may be, however, rather crude, especially in case of extended objects such as the linear dipole infrared antenna, where retardation effects cause a significant deviation of the antenna polarizability from quasi-static models. Here we note that in general, the object polarizabilities inserted into our model can be taken as results of a different and more accurate approach, such as the one developed in reference [4]. Another difficulty arises, when one wants to obtain the mutual coupling strengths among different sample and antenna modes. The mutual coupling is generally solution of a complex self-consistent problem which is hard to perform analytically. Instead of it, we will use the developed approach as a parametric model and show how the model can be applied for interpretation of realistic experimental situations.

In the next section, we will provide a practical example of the model application on a system of a single linear infrared antenna interacting with a sample made of silicon oxide (SiO_2) in different geometrical arrangements. We will show that the analytical model is capable of explaining features of the antenna-sample mutual interaction by comparing results from the analytical model with the numerical calculations.

5.3 Antennas interacting with model SiO_2

Interaction of an infrared antenna with a sample made of SiO_2 has been widely studied throughout the literature [12, 14, 105]. We have already discussed that the SEIRS spectrum results as an interference among resonant mode of the antenna and all resonant modes of the sample which are inseparably linked to the sample geometrical configuration. Hence, before we start to describe the mutually interacting system, we should identify the modes which take part in the interaction. To do so, we introduce the dielectric properties of an artificial strong oscillator SiO_2 which are in infrared region expressed by a Lorentz dielectric function

$$\varepsilon_{\mathrm{SiO_2}} = \varepsilon_\infty + \frac{\Omega^2}{\omega_{\mathrm{TO}}^2 - \omega^2 - \mathrm{i}\gamma\omega}, \tag{5.35}$$

with $\varepsilon_\infty = 2.14$, oscillator strength $\Omega = 950\ \mathrm{cm}^{-1}$, transverse phonon resonant frequency $\omega_{\mathrm{TO}} = 1064\ \mathrm{cm}^{-1}$ and damping $\gamma = 10\ \mathrm{cm}^{-1}$. The SiO_2 dielectric function plotted in Figure 5.2 exhibits a resonant behaviour of its imaginary part which is related to a transverse optical phonon (TO) resonance. We set the oscillator strength Ω large enough, so that the real part of the dielectric function crosses zero and therefore enables existence of longitudinal resonances. It is well known that a longitudinal phonon (LO) frequency is localized at the zero of the real part of the dielectric function, which can be observed in the bulk energy loss function $\Im\{-1/\varepsilon\}$ as a sharp peak corresponding to $\omega_{\mathrm{LO}} = 1247\ \mathrm{cm}^{-1}$. We note here that the second zero of the dielectric function real part does not yield the LO mode, because it is strongly damped by resonantly increased dielectric function imaginary part close to the TO frequency. Finally, a surface phonon polariton (SPP) frequency for a semi-infinite interface with vacuum is located at the resonant maximum of the surface

energy loss function $\Im\{-1/(\varepsilon+1)\}$, reflecting the condition $\Re\{\varepsilon\} = -1$. Since the SiO_2 layer does not represent a semi-infinite interface, the surface phonon excitation frequency is positioned in the range between ω_{SPP} and ω_{LO} (depending on the layer geometry) due to dispersion of the SPP modes [105–107].

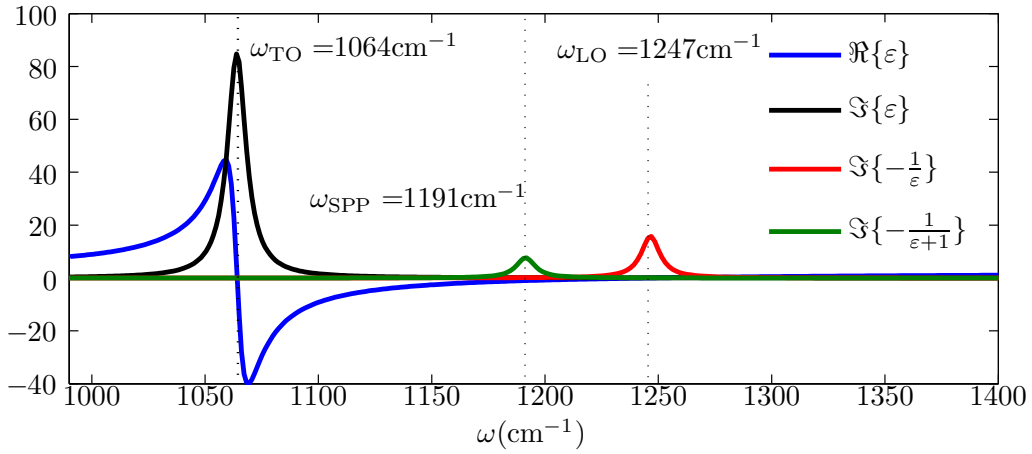

Figure 5.2: Lorentz model dielectric function of SiO_2. Peak of $\mathrm{Im}\{\varepsilon\}$ appears at ω_{TO} frequency, peak of $\mathrm{Im}\{-1/\varepsilon\}$ corresponds to ω_{LO} and peak of $\mathrm{Im}\{-1/(\varepsilon+1)\}$ corresponds to ω_{SPP} frequency.

The sample modes are obtained as a combination of the material dielectric properties and the shape of the container in which the material is placed. We will consider two distinct geometrical configurations of the sample. First, the probing linear infrared antenna will be covered by a homogeneous layer of SiO_2, having variable thickness, and second, a ring of SiO_2 will be placed into different positions along the antenna analogously to reference [64].

We tune the linear antenna to have a known basic dipole resonance centred at the frequency ω_{LO} of the SiO_2. In the analytical model, we describe the antenna resonance by generalized polarizability

$$\alpha^{A} = \frac{f_A}{\omega_A^2 - \omega^2 - \mathrm{i}\gamma_A\omega}, \tag{5.36}$$

with γ_A and f_A being fit parameters. Parameters of the model are adjusted by fitting the analytical scattering spectrum to the scattering spectrum obtained by numerical FDTD simulations. The linear antenna geometry is optimized for the simulation to have an overall length of $L = 3.2\,\mu\mathrm{m}$ with a radius $a = 50$ nm and a material properties modelled by the Palik gold dielectric function [108]. Parameters for the antenna mode were fitted as $f_A \doteq 1.008 \times 10^{-22}\ \mathrm{F\,m^2\,cm^{-2}}$, $\omega_A \doteq 1260\ \mathrm{cm^{-1}}$ and $\gamma_A \doteq 60\ \mathrm{cm^{-1}}$.

The modes of the SiO_2 sample will be more challenging to identify, especially because we need to take into account the sample geometry. In the following, we will identify the modes which couple with the dipole antenna for the considered geometry and assign them to the model oscillators which will subsequently yield the interference spectrum.

5.3.1 Antenna covered by SiO_2 layer

Following the reference [109], we seek three classes of solutions for the SiO_2 modes: the transverse modes, the longitudinal modes and the surface modes. The transverse modes, as well as the longitudinal modes, will have the resonant frequency well defined by the material properties, hence their resonant frequencies will equal ω_{LO} and ω_{TO} respectively. The geometrical factor will, however, strongly influence the resonant frequencies of the surface modes, which will show up to be the modes of our interest. The SiO_2 layer is basically a hollow cylinder with two spherical shell lids on both ends. We can expect that one class of the surface modes will be similar to the modes of a hollow cylindrical shell. Inner radius a of the shell will be the radius of the linear cylindrical antenna which is encapsulated in the SiO_2 layer, and outer radius will be related to the layer thickness. For simplicity, a quasi-static model will be employed for solution of the cylinder surface mode dispersion relation.

We will start with a standard set-up for solution of the Laplace equation in regions inside of the cylinder, inside of the SiO_2 shell and outside of the cylinder. The fields will be sought as a linear combination of functions solving the Laplace equation in cylindrical coordinates (ρ, ϕ, z) [109]

$$f_1 = \mathrm{K}_m(\kappa\rho)\exp(\mathrm{i}\kappa z)\exp(\mathrm{i}m\phi), \tag{5.37}$$

$$f_2 = \mathrm{I}_m(\kappa\rho)\exp(\mathrm{i}\kappa z)\exp(\mathrm{i}m\phi), \tag{5.38}$$

where $\mathrm{K}_m(x)$ and $\mathrm{I}_m(x)$ are modified Bessel functions of the first and second kind [110]. We impose on the solutions a standard set of boundary conditions and obtain the secular determinant, from which the quasi-static dispersion relation follows. Details of the calculation are left to the Appendix A. We plot the dispersion relation of the rotationally symmetric surface phonon ($m = 0$) for three cylindrical layers of increasing thickness (10 nm, 30 nm and 100 nm, having inner radius $a = 50$ nm) in Figure 5.3. The dispersion relations consist of two branches, the high frequency branch and the low frequency branch, which start for $\kappa = 0$ at the frequencies of the longitudinal and transverse modes regardless of the layer geometrical parameters. All of the branches are approaching the limit of the surface phonon frequency ω_{SPP} for high values of κ and their derivative with respect to the wave number κ tends to zero ($\mathrm{d}\omega(\kappa)/\mathrm{d}\kappa \to 0$). As a result, a high density of surface phonon modes emerges close to the surface phonon frequency ω_{SPP}. We can therefore expect relatively strong coupling between the cylindrical shell surface modes and the antenna basic mode close to the frequency ω_{SPP}. We use the conclusion and include a model oscillator with resonant frequency ω_{SPP} in our coupled oscillator model.

We can seek another surface mode as a dipole mode of the hollow SiO_2 phononic antenna, oscillating along the antenna longitudinal axis. Solution of the Laplace equation for this geometry might be a rather challenging task, we perform therefore a numerical simulation of the hollow shell by method of finite differences in time domain and calculate the spectral response of such shell. The absorption, scattering and extinction spectra resulting from the numerical calculation of scattering on a 30 nm thick shell are shown in Figure 5.4. The spectra sharply peak around the transverse phonon frequency ω_{TO}. The absolute values of the cross sections indicate a weak coupling of the mode to the incident radiation. The values of the spectra

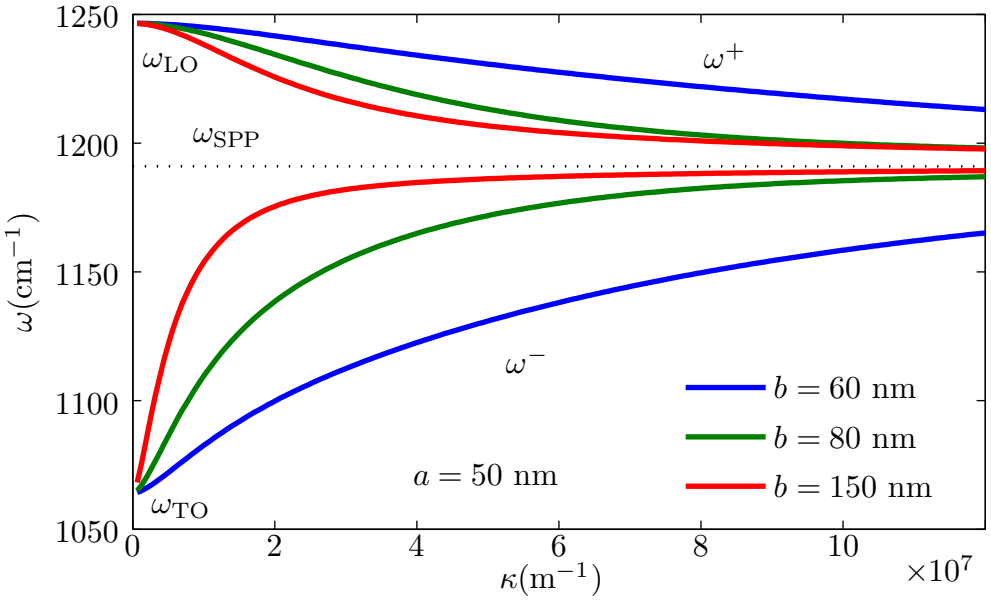

Figure 5.3: Dispersion relation of cylinder shell surface modes with polar symmetry ($m = 0$) calculated in quasi-static approximation and neglecting material losses. The dispersion relation is depicted for three different outer radii of cylindrical shell, $b = 60$ nm, $b = 80$ nm and $b = 150$ nm. The inner radius is $a = 50$ nm for all situations. The dispersion relation depicts hybridization of surface modes into high frequency (ω^+) and low frequency (ω^-) modes. All modes converge towards the calculated surface phonon frequency $\omega_{\mathrm{SPP}} \approx 1191$ cm^{-1}. The surface modes are allowed in the region between the transverse phonon frequency ω_{TO} and longitudinal frequency ω_{LO}.

are one order of magnitude smaller than in case of metallic resonant antennas of a similar size. The position of the resonant frequency can be qualitatively understood by considering a longitudinal resonance of a prolate spheroidal shell in quasi-static approximation. The longitudinal component of polarizability is given by [97]

$$\alpha_{\parallel} = V^{(2)}\varepsilon_0(\varepsilon - 1)\frac{\varepsilon(1-f) + (1-\varepsilon)(L_{\parallel}^{(1)} - fL_{\parallel}^{(2)})}{\left[\varepsilon + (1-\varepsilon)(L_{\parallel}^{(1)} - fL_{\parallel}^{(2)})\right]\left[1 + (\varepsilon - 1)L_{\parallel}^{(2)}\right] + fL_{\parallel}^{(2)}\varepsilon(1-\varepsilon)}, \tag{5.39}$$

where $V = 4\pi a_2 b_2 c_2/3$ is the volume of the larger ellipsoid (the outer boundary) and a_2, b_2 and c_2 are the ellipsoid semiaxes. $L_{\parallel}^{(1)}$ and $L_{\parallel}^{(2)}$ are depolarization parameters defined by geometry of the spheroid [97]. The parameter $f = a_1 b_1 c_1/a_2 b_2 c_2$ is a volume ratio between the inner and outer ellipsoid. We observe that for a prolate spheroid with a large ratio of the major semiaxes to the minor semiaxis, the depolarization factors approach zero. We can estimate their value from the geometry defined by the encapsulated linear antenna with help of the long cylinder depolarization factors $L^{(i)} \approx 2r_i^2/L_i^2$ [34], where r_i denotes the radius of the inner (outer) cylinder and L_i the respective cylinder length. Value of the depolarization factor will be of the order 10^{-2}, which allows us to neglect the products of depolarization

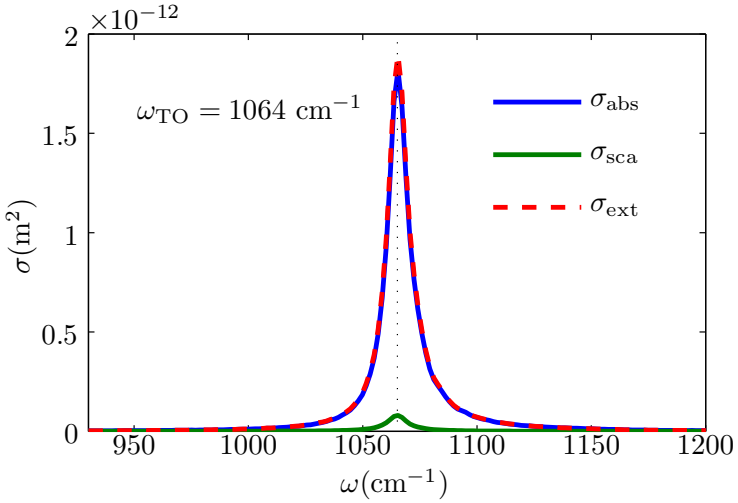

Figure 5.4: Absorption, scattering and extinction spectra calculated numerically including retardation effects. The spectra exhibit a sharp peak centred at the frequency of transverse phonon oscillation. The scattering cross section (green) is strongly suppressed compared to the absorption spectrum (blue) and the resulting extinction (red), which together with relatively low absolute values, one order of magnitude smaller than for resonant metallic antennas of similar size, indicates a weak dipole moment of the mode. The mode basically reflects the material resonance of SiO_2, which directly follows from its dielectric function. More details are provided in the main text.

factors with quantities of the same order as dielectric function, retaining only terms proportional directly to the dielectric function. Under these assumptions, the fraction in (5.39) will be almost equal to the constant $1 - f$, except for a narrow region close to the resonance of dielectric function, where a slight frequency dependence is still expected. The resonance of the shell will be predominantly driven by the material constant ε standing in front of the fraction and occur on the transverse phonon frequency ω_{TO}. This is in good agreement with the numerical simulation (compare Figure 5.2 and Figure 5.4).

Additionally to the previously mentioned considerations, we perform full numerical calculation of the antenna-layer system and identify the field distributions at frequencies ω_{LO}, ω_{TO} and ω_{SPP}. We perform the simulations for 30 nm thick layer. The field distributions of the modes are depicted in Figure 5.5. We identify a rotationally symmetric mode on the longitudinal phonon frequency ω_{LO}. This mode couples efficiently to the gold antenna dipole mode, being the surface mode ω^+ of the cylindrical part of the layer with wavenumber corresponding approximately to the double of the antenna length $\kappa \approx \pi / L_{\mathrm{antenna}}$. Such a wavenumber is small enough for the surface phonon to have a frequency almost equal to the longitudinal phonon frequency (note the flat ω^+ branch for low κ). When the system is excited at frequency ω_{SPP} or in its vicinity, the high wavenumber surface phonon is observed on the layer. We also noticed that the surface phonon wavelenth changes rapidly with slight deviation from the frequency ω_{SPP} (not shown in the Figure 5.5) in accor-

dance with dispersion of the ω^+ branch. At the frequency ω_{TO}, the whole structure oscillates as a dipole antenna in agreement with the theoretical prediction that the dipole mode of the SiO_2 shell will be in resonance.

We have identified the frequencies of the possible layer modes which can in principle contribute to the mutual interference of the antenna and the sample. Now we exploit results of the preceding discussion and propose a generalized polarizability of the sample in the form of a sum of independent Lorentz oscillators:

$$\alpha^{\mathrm{S}} = \alpha^{\mathrm{BG}} + \frac{f_{\mathrm{LO}}}{\omega_{\mathrm{LO}}^2 - \omega^2 - \mathrm{i}\gamma_{\mathrm{LO}}\omega} + \frac{f_{\mathrm{TO}}}{\omega_{\mathrm{TO}}^2 - \omega^2 - \mathrm{i}\gamma_{\mathrm{TO}}\omega} + \frac{f_{\mathrm{SPP}}}{\omega_{\mathrm{SPP}}^2 - \omega^2 - \mathrm{i}\gamma_{\mathrm{SPP}}\omega}, \tag{5.40}$$

where α^{BG} is the background polarizability, f_i are oscillator strengths of respective modes and γ_i are respective line-widths. These parameters, together with possible corrections of resonant frequencies, are either to be specified by matching of the coupled oscillator model to the experimental (or numerically calculated) data, or to be obtained from some more elaborate calculation. In practical applications, the experimentalist is usually left with a set of data supported by a limited amount of information. Accordingly we demonstrate that the proposed model satisfactorily reproduces data obtained from a numerical simulation when the parameters are chosen properly. We carry out a set of FDTD calculations of the model system consisting of the antenna and the SiO_2 layer of increasing thickness. The numerically calculated spectra and the spectra rising from our analytical model are compared in Figure 5.6.

The absorption, scattering and extinction spectra in Figures 5.6 exhibit an increasing dip in the middle of the bare antenna peak which splits the antenna resonance into two parts: the high energy peak and the low energy peak. This feature can be interpreted as a strong coupling effect between the antenna mode and the SiO_2 layer mode at the LO frequency, which further promotes with increasing layer thickness. When the coupling is stronger, the low energy peak red shifts, while the high energy peak position remains almost unchanged. The peak shifts can be explained by combination of two competing effects. The phonon excitation at longitudinal phonon frequency tends to open the transparency window (hence the EIT) in the middle of the antenna resonance, simultaneously blue shifting the high energy peak and red shifting the low energy peak. Effect of the constant sample background polarizability α_{BG} results in an overall red shift of the antenna spectrum, which almost fixes the position of the high energy peak and enhances the red shift of the low energy peak.

Additionally to the main effect of the peak splitting there appears a small peak at the frequency of the layer short wavelength surface modes. The peak at the surface phonon frequency becomes larger with increasing thickness of the layer. At the beginning, the coupling of the antenna mode with the mode at surface phonon frequency is hardly notable, but starts to develop into a peak when the antenna transparency window opens. Similarly, the resonance at the frequency ω_{TO} appears only after the main antenna peak splits and the low energy peak shifts to the proper position of the TO frequency resonance. The antenna field enhancement is considerably stronger at the TO frequency for thicker layers, which in turn causes stronger interaction between the antenna mode and the respective mode of the structure.

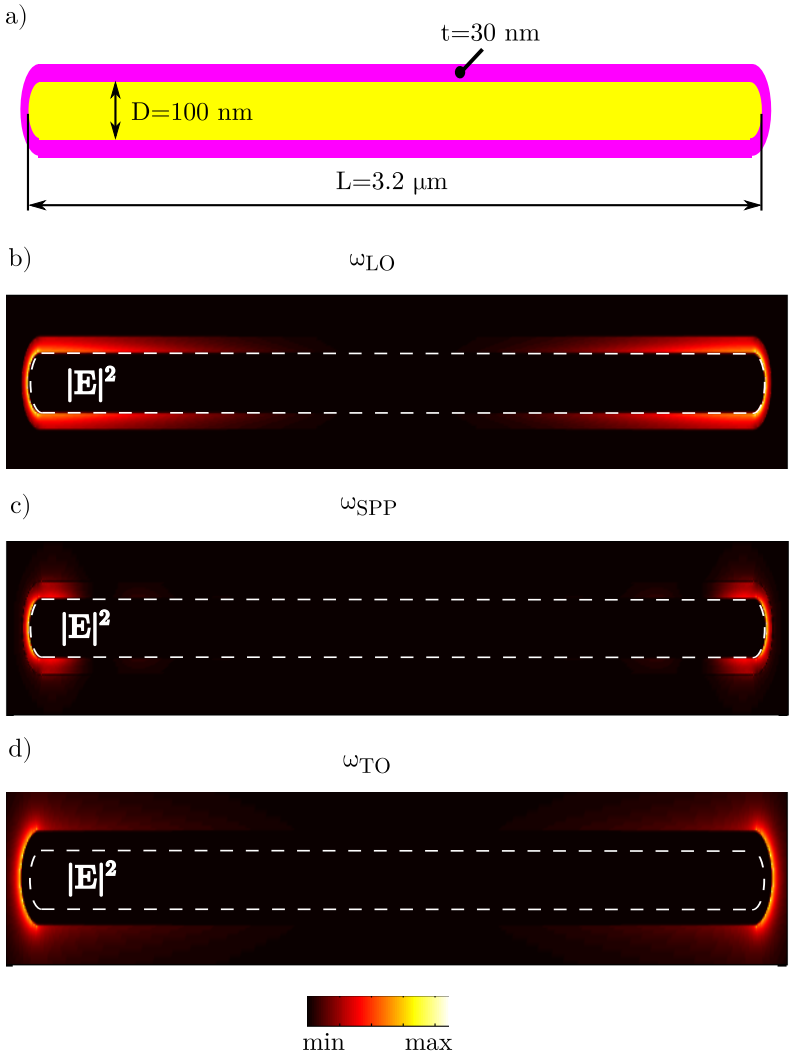

Figure 5.5: Field distributions $|E|^2$ at frequencies b) ω_{LO}, c) ω_{SPP} and d) ω_{TO} calculated numerically (FDTD) at the central cross-section of the antenna covered by 30 nm thick layer [see inset in a)]. The field distribution of mode excited on frequency ω_{LO} is identified as a surface ω^+ mode having wavenumber $\kappa \approx \pi / L_{\mathrm{antenna}}$. The mode found in the vicinity of the surface phonon frequency ω_{SPP} is excited at the antenna ends, where coupling to the short-wavelength surface phonons of the ω^+ branch is dominant. The mode found close to the frequency ω_{TO} resembles the dipole surface mode of the whole layer. Note that the electric field is pushed away from both the antenna and the layer.

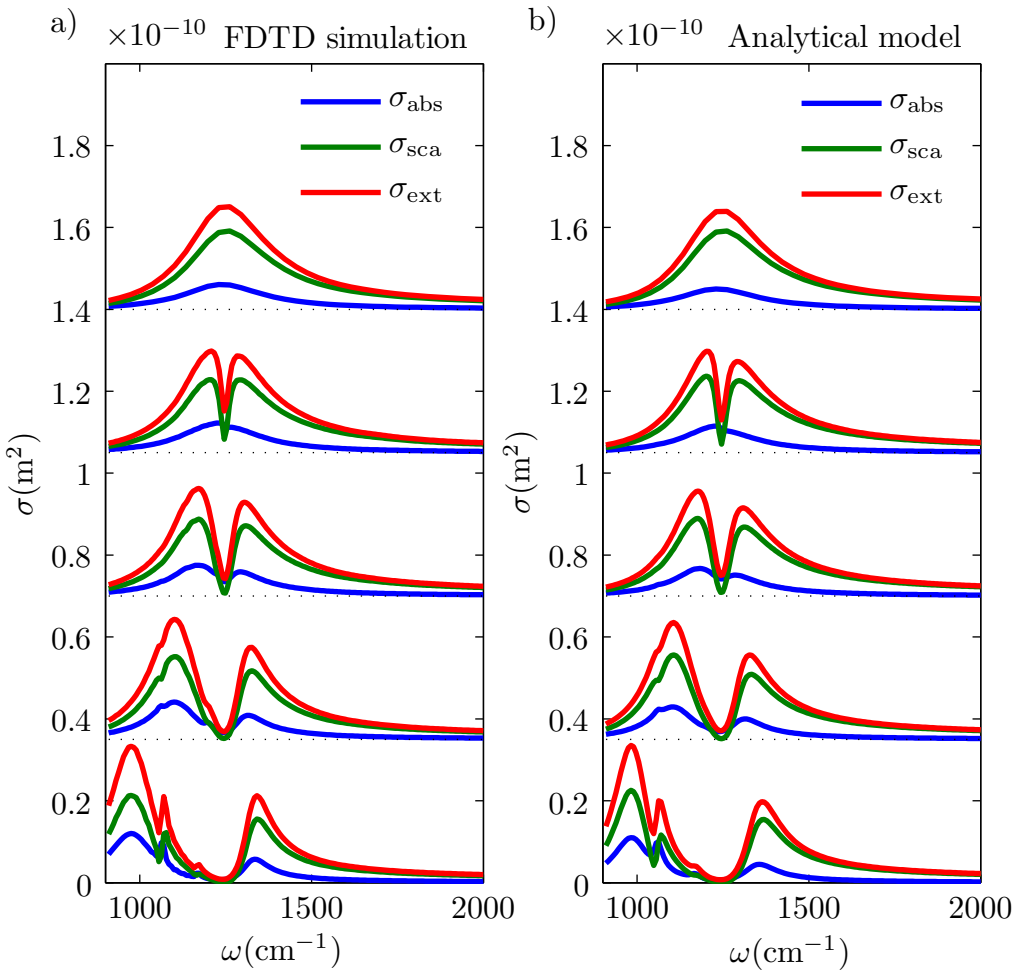

Figure 5.6: Numerically calculated spectra (left) and spectra calculated by the extended coupled harmonic oscillator model (right) are compared. The spectra are calculated for different layer thickness, ranging from top to the bottom 0 nm, 3 nm, 10 nm, 30 nm and 100 nm. The analytical model parameters were adjusted to provide good match with the numerical scattering spectrum, using three harmonic oscillators to model the layer modes and one oscillator to model the antenna dipole mode. The parameters used in the analytical model are for completeness summarized in Appendix B.

We see that the analytical model is not only a simple approach for calculation of the SEIRS spectra, but it is especially an invaluable tool for interpretation and understanding of the spectral features. We have to realize that the analytical model developed here is not able to describe the scattering system of the antenna and the layer exactly. For example, the harmonic oscillator centred at the position of the layer surface phonon frequency is obviously only an approximation to the otherwise more difficult problem of the mode continuum coupling with the antenna dipole mode. The approximation of the exactly centred oscillator explains well the shape of the spectra for thicker layers, but fails for thin layers where the flat surface phonon dispersion relation causes notable differences between the analytical model and the numerical simulation. Furthermore, the red shifted low energy peak is narrower in the analytical model than in the numerical simulation. This is another inaccuracy of the analytical description rising probably from the finite size of the antenna, neglecting the sample contributions to the spectra and consequent size effects which are lacking in our model [20].

It also shows up that the coupling parameter and the parameter of oscillator strength have the same impact on the spectral line shape. This follows from the product in which the coupling parameter $G^{\mathrm{A}\to\mathrm{S}}$ and the oscillator strengths appear. For this reason we do not distinguish between coupling parameters for particular modes and include the variable coupling to different modes into the mode oscillator strengths. Potential fitting of our model to experimental data would be therefore rather insensitive to the distinction between the coupling parameter and oscillator strength. Practically it means that we are not able to distinguish between signal from a small sample placed in a position where the antenna has a large near-field enhancement and a large sample placed into insensitive position of the antenna such as the antenna center. This is probably the largest obstacle for the quantitative analysis in SEIRS.

Moreover, we have to realize that the experimental data usually correspond to different physical quantities which resemble the extinction, scattering and absorption spectra considered here, but do not exactly match them. A special care must be therefore taken for selection of a correct model for calculation of the experimental spectrum. The extinction spectrum is usually the one which is experimentally accessed in the transmission experimental configurations. Because of the afore mentioned, we propose the model presented here more as a qualitative tool for understanding of the coupling mechanism rather than means for exact quantitative analysis.

In the following section, we will aim on influence of the near-field enhancement (hence the coupling parameter) on the antenna-sample interaction. The coupling will be studied on a system of antenna and a SiO_2 rings. The rings will be shifted along the antenna longitudinal axis.

5.3.2 Antenna with rings

In the previous section we identified possible modes of the antenna-layer coupled system, where we aimed on interaction of different layer modes with the antenna. Now, we will deal with a single sample of a well defined geometry – the pair of rota-

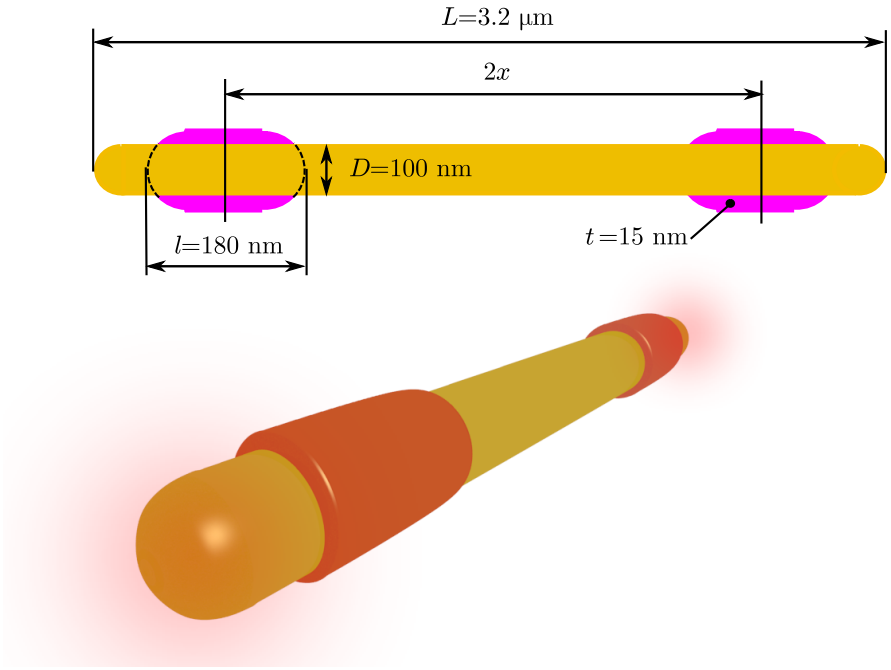

Figure 5.7: Schema of geometrical arrangement. Two rings of our model SiO_2 are placed along the antenna symmetrically to the antenna center with varying distance x from the center. The proportionality of the ring size and size of the antenna is not preserved in the drawing.

tionally symmetric rings placed symmetrically on the gold antenna as schematically depicted in Figure 5.7. We use exactly the same gold antenna and SiO_2 dielectric function as described in the previous sections.

The two artificial SiO_2 rings are positioned into increasing distance from the antenna center (measured to the ring center) from 0.1 μm to 1.45 μm so that sufficient distance is kept between them. In such case, the two rings can be treated as independent and the signal from the antenna will reflect only interaction between the antenna and the rings. The change of position therefore does not cause a change in the oscillator strength of the sample and the coupling strength between the antenna and the sample $G^{A\to S}$ remains the only variable parameter.

We perform numerical FDTD simulations of the antenna-ring system. The ring is shaped as a hollow cylinder of thickness 15 nm and length 180 nm with rounded edges. The inner diameter of the rings is equal to the diameter of the antenna, so that the rings closely stick to the antenna surface. The absorption, scattering and extinction spectra calculated numerically are shown in Figure 5.8. Coupling of the antenna dipole mode with the mode of the ring gives rise to the sharp dip positioned between the surface phonon frequency and the longitudinal phonon frequency. The position of the peak is a consequence of the surface phonon dispersion similarly as described in the previous section. When the ring is shifted towards the antenna apexes out of the antenna center, the characteristic Fano-resonance profile becomes more pronounced. The scattering and extinction spectra exhibit increasing dip in the position of the ring resonance. The absorption spectrum reveals a weak antiresonance feature which

slowly transforms into the antisymmetric Fano-resonance for ring positions close to the antenna apex. The coupling between the antenna and the sample is therefore stronger closer to the antenna apexes in accordance with intuitive expectations.

We follow the analysis of the paper [64], where the Fano-resonance size is measured as a peak-to-peak size of the resonance dip in the extinction spectrum normalized to the baseline. As a baseline we take the spectrum of the antenna with the same geometrical arrangement of the rings, but using a constant ring dielectric function $\varepsilon = 4$. We account so for the constant red-shift caused by the background polarizability of the rings but avoid the resonant antenna-sample coupling. We plot the size of the resonance as a function of distance from the antenna center and compare the obtained dependence with the numerically calculated antenna near-field enhancement along the antenna longitudinal axis in distance of 15 nm above the antenna surface in Figure 5.10. The near-field enhancement dependence on the distance from the antenna center has a linear character as it was experimentally verified in Chapter 3.2.2. Accordingly, the intensity profile follows the quadratic dependence on the distance from the antenna center having the parabolic shape. We find that the size of the dip in the extinction spectrum depends almost linearly on the ring position. Our finding seemingly contradicts the results of reference [64] where a dependence following the parabolic intensity profile was found. The dependence found in [64] is depicted in Figure 5.9.

The difference between our finding and results of reference [64] is striking. We attribute the different behaviour of the dip size to the different regime in which the antenna-sample interaction is operated. In the paper [64] a sample with weak resonance is used as a near-field probe. The weak interaction regime is achieved in the paper thanks to the weak material resonance of the sample which causes only negligible deviations of the antenna spectral line from the non-interacting case. The situation using the artificial SiO_2 rings is entirely different. The rings interact with the antenna strongly, causing splitting of the antenna resonance peak. In the strong interaction regime, the pure quadratic dependence of the signal can not be expected any more. We address therefore the almost linear behaviour of the dip dependence on the position to the strong coupling regime which occurs in the antenna sample interaction.

The increase of the coupling between the antenna and the ring is attributed to the antenna near-field enhancement in the position of the sample ring. This follows from the original integral relation from which the coupling coefficient was obtained:

$$\langle \mathbf{f} | \mathbf{G}_{\mathrm{SA}}^{\mathrm{st}} | \mathbf{e} \rangle \propto \int_{\mathrm{A}} \int_{\mathrm{S}} \mathbf{f}^*(\mathbf{r}'') \cdot \mathbf{G}(\mathbf{r}'', \mathbf{r}') \cdot \mathbf{e}(\mathbf{r}') \mathrm{d}\mathbf{r}' \mathrm{d}\mathbf{r}''. \tag{5.41}$$

The electric field distribution inside of the antenna $|\mathbf{e}\rangle$ corresponds to the antenna dipole mode. The integral therefore simply evaluates the external field induced by the antenna. The actual value of the antenna internal field is not included in the definition of the coupling coefficient and we therefore conclude that the coupling coefficient depends on the bare near-field profile of the antenna dipole mode. Due to the strong field enhancement in the vicinity of the antenna, we neglect the incident light with respect to the light scattered from the antenna. The coupling parameter between the antenna and the sample ring will be proportional to the field enhancement in the position of the ring. The coupling also inherently includes dependence of

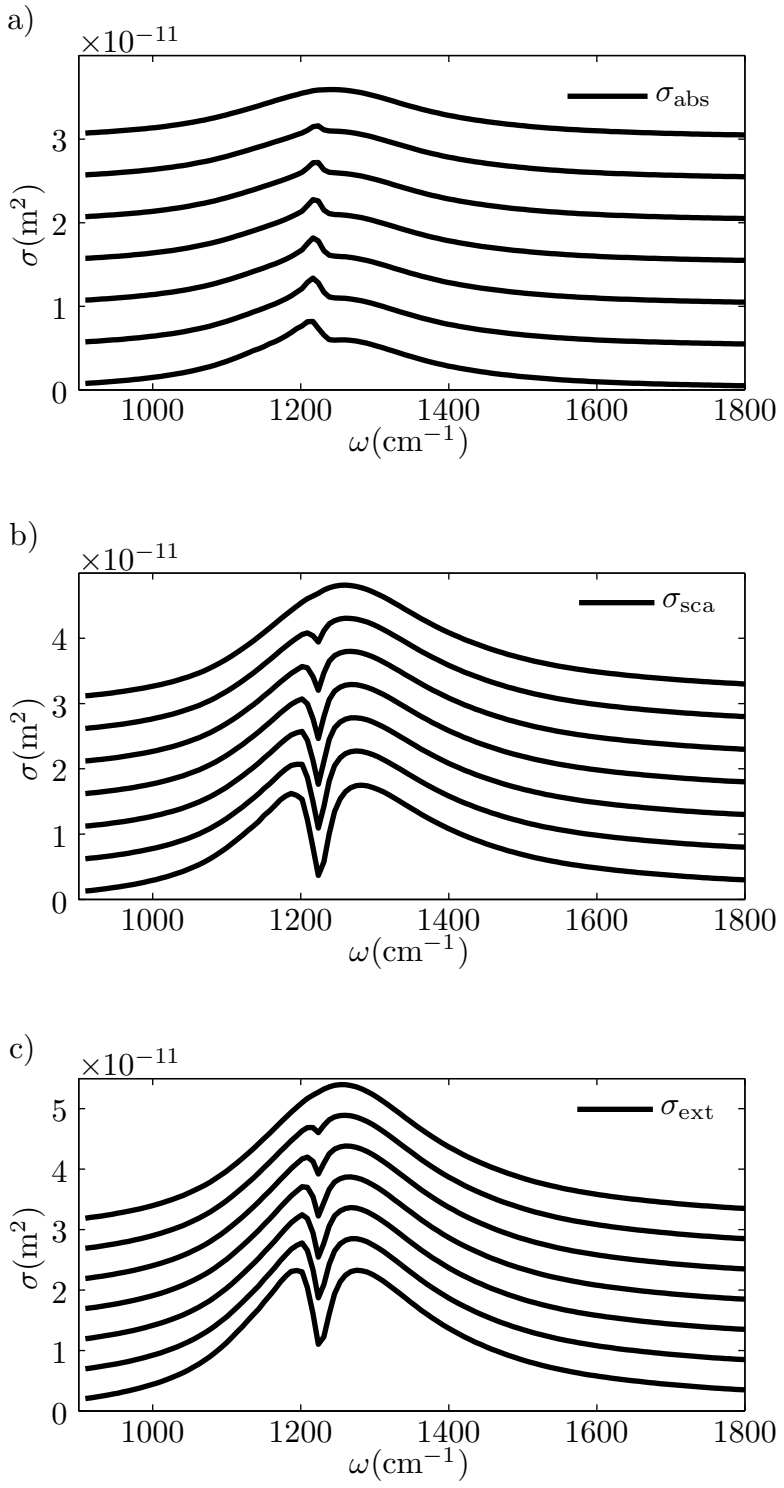

Figure 5.8: Numerically calculated a) the absorption b) the scattering and c) the extinction spectra of the antenna with a pair of rings which are gradually shifted towards the antenna ends. Spectra for ring positions x (from top to bottom) 0.1 µm, 0.4 µm, 0.6 µm, 0.8 µm, 1.0 µm, 1.2 µm and 1.45 µm.

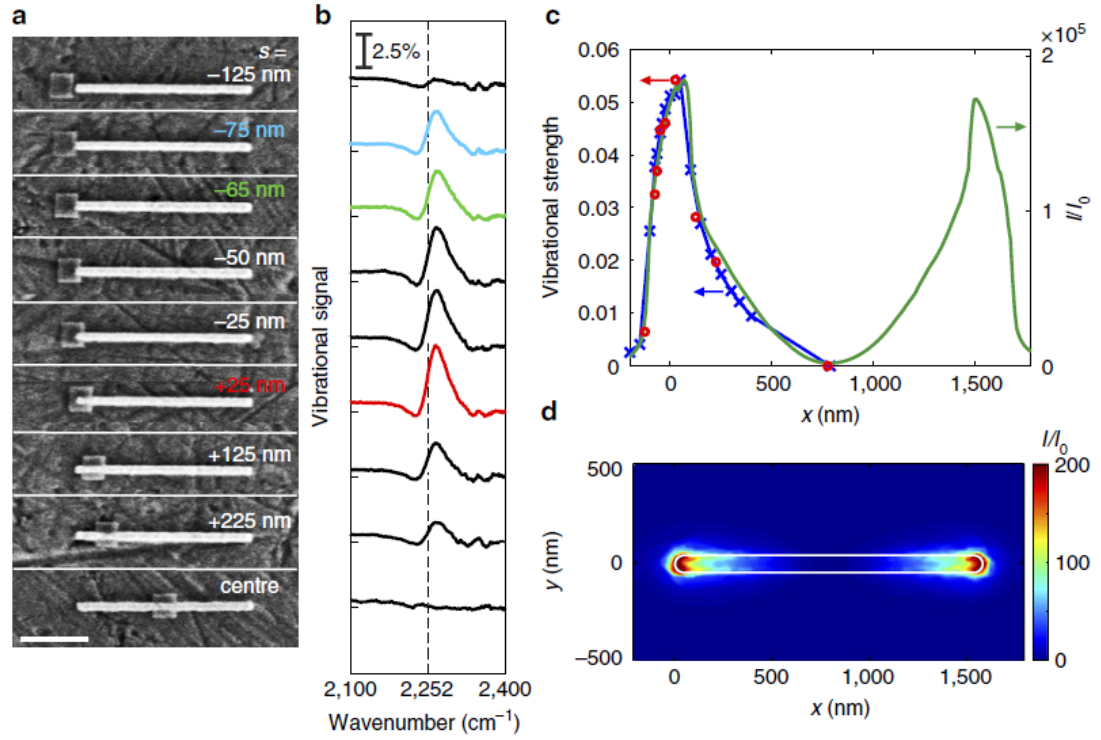

Figure 5.9: The measurement of depth of the spectral dip for different positions of the sample along the linear dipole antenna. The image is taken from reference [64]. The scanning electron images of the configuration are shown in a) and corresponding normalized spectral dip size is plotted in b). In c) the authors of [64] demonstrate that the dip peak to peak size copies the profile of near-field intensity ($\propto |E|^2$) in position of the sample. The experimental results are compared here to the FDTD calculations with a good match. The near-field distribution of the antenna in a constant height is depicted in d).

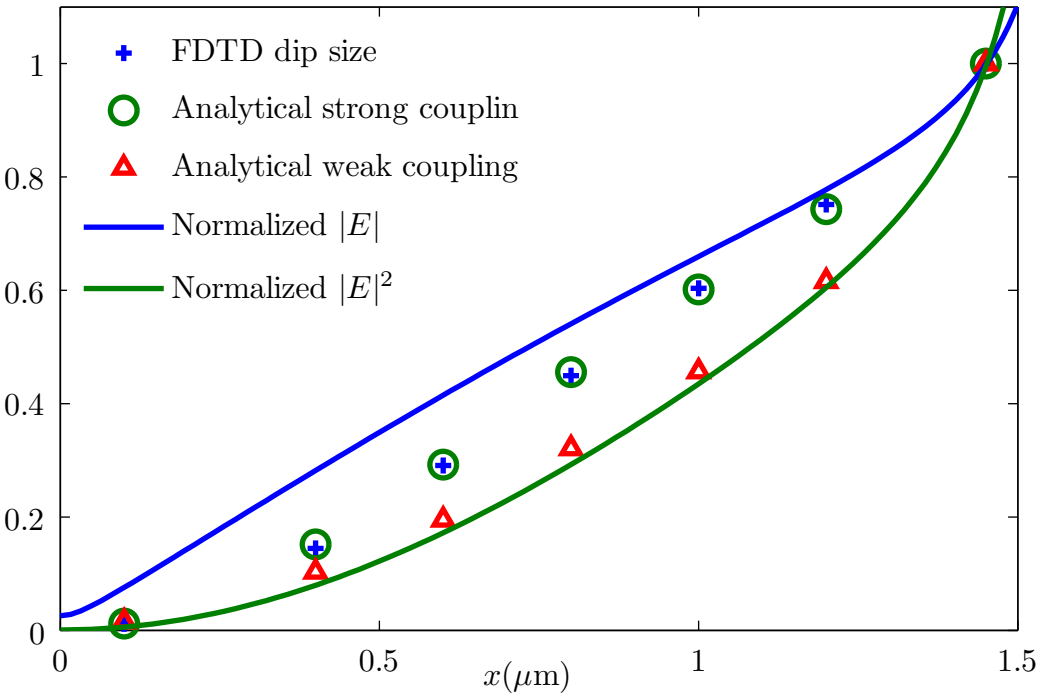

Figure 5.10: Normalized size of the dip in the extinction spectrum of the the antenna with rings for different ring positions x. The numerical FDTD results are compared with results obtained from the analytical model. The parameters of the model were matched to the numerical extinction spectrum. Additionally we calculated the dip sizes for patches with ten times weaker oscillator strength using the analytical model. We varied the coupling strength as a linear function of the bare antenna near-field enhancement in the position of the ring in both cases. For comparison, the normalized near-field enhancement and near-field intensity profiles are shown.

the sample shape and the distribution of the antenna induced fields over the sample volume. The electric field induced by the antenna must simply geometrically match the mode of the sample. The last step of the connection between the near-field enhancement and the coupling constant therefore assumes that the antenna induced field distribution over the sample volume will be equal for all of the sample positions. That requirement is met for the rings placed along the antenna.

We employ our radiation corrected analytical model and investigate how the spectral dip varies with the position of the ring along the linear antenna. In Figure 5.10 the dependence of the dip size is plotted as a function of the distance x. Following the discussion above, we set the coupling coefficient directly proportional to the antenna near-field calculated at the position of the ring x. Two dependencies of the dip-size on the coupling parameter are shown: a regime when the sample polarizability is weak and causes only minor change of the antenna dipole resonance and the regime when the dip almost splits the antenna resonance (similar to the numerical simulations of the rings). The transition from the quadratic dependence of the dip size for the weak interaction towards the linear regime is observed. We note that the linearity of the dip size is maintained only in the narrow region where the dip is sufficiently pronounced and does not completely split the main antenna peak.

Hence we found that for small samples positioned in the vicinity of the antenna the coupling constant corresponds to the near-field enhancement of the antenna in the respective position. That finding together with the dependence of the anti-resonant dip size on the coupling strength has consequences for quantitative understanding of the spectroscopic signal in SEIRS and also a significant overlap towards the field of the near-field microscopy. The interaction of the sample with the tip is described by similar equations as the antenna-sample interaction in SEIRS. The interpretation of the s-SNOM signal is a result of interference between the scattered light and a reference beam in a complex interferometric set-up. Only the modulated part of the light scattered from the antenna and the sample is detected, particularly the electric field rising from the mutual interaction of the antenna and the tip.

Thanks to it, the connection between the interference dip which strongly depends on the tip-sample configuration and the s-SNOM signal is relatively close. This can be shown for weakly interacting samples, where the multiple scattering approach can be applied. The electric field which is scattered towards the detector consists of a sum of the incident field, $\mathbf{E}^{\mathrm{inc}}$, the field coming from interaction with the bare antenna $\mathbf{E}^{\mathrm{A}}$ plus the scattering rising from the mutual antenna sample interaction $\mathbf{E}^{\mathrm{int}}$. We neglect here the direct scattering from the sample. The spectrum measured in the forward scattering direction corresponds to the square of the electric field modulus $|\mathbf{E}^{\mathrm{inc}} + \mathbf{E}^{\mathrm{A}} + \mathbf{E}^{\mathrm{int}}|^2$. By neglecting the second order contributions from $\mathbf{E}^{\mathrm{int}}$ the spectral signal reduces to a sum of the bare antenna spectral response $|\mathbf{E}^{\mathrm{inc}} + \mathbf{E}^{\mathrm{A}}|^2$ plus the terms linearly proportional to the electric field emerging from the antenna-sample interaction $(\mathbf{E}^{\mathrm{inc}} + \mathbf{E}^{\mathrm{A}}) \cdot \mathbf{E}^{\mathrm{int}\,*} + (\mathbf{E}^{\mathrm{inc}} + \mathbf{E}^{\mathrm{A}})^* \cdot \mathbf{E}^{\mathrm{int}}$. The second term is responsible for deviations from the bare antenna spectrum, including the spectral dip. Even though we established the relation between the s-SNOM signal and the spectral dip only for weakly scattering samples, we can expect some connection in the strong interaction regime as well.

Our findings indicate that the s-SNOM signal obtained with strongly interacting resonant probes might surprisingly follow almost linearly the profile of the antenna near-field. This result would bring a new insight into the field of the near-field microscopy and therefore deserves further thorough investigation. We therefore also propose experimental study on the topic of distinction between the weak and the strong interaction regime in the field of SEIRS, where spectroscopic measurements are instrumentally less demanding than the s-SNOM measurements. The weak interaction regime can be moreover easily distinguished from the antenna-sample spectral response which is difficult to perform with s-SNOM. The strong interaction regime will not be too sensitive to experimental noise and the practical measurements could be in principle performed with ease.

Unfortunately, the realistic dielectric function of the SiO_2 does not provide very strong resonance on the transverse and longitudinal phonon frequencies. The real SiO_2 could be in principle used in larger quantities to produce the spectral dip at frequency close to the TO phonon frequency [14]. Alternatively, another material which exhibits a strong Lorentz resonance would serve as a good substitute for the large amount of the SiO_2.

In conclusion, we propose the spectral experimental investigation of the samples strongly interacting with infrared antennas with hope that they become a starting point towards the complete understanding of the s-SNOM imaging. The strong interaction regime between the infrared antennas and the sample shows a novel almost linear dependence of the extinction spectrum dip size on the coupling strength between the sample and the antenna. The coupling strength is shown to be proportional to the near-field enhancement of the antenna which establishes the connection between the infrared spectroscopy and the near-field microscopy.

6 | Conclusion

The development of nanotechnology enabled manufacturing of matter on nanoscale and gave rise to completely new research area of near-field optics, nano-photonics and plasmonics. The classical problem of electromagnetic scattering suddenly gained a new perspective, the perspective of the near-electromagnetic field, its engineering and applications. The metallic nano- and micro-particles became devices which are able to squeeze and consequently also enhance the electromagnetic field on sub-wavelength scale. This way of localizing electromagnetic field is often referred as nano-focusing which breaks the diffraction limit of conventional optics. The obtained field enhancement has already proven useful especially in the field of field enhanced spectroscopy including the vibrational and fluorescent spectroscopic methods. The applications of the metallic structures are strongly connected to the near-field properties of the structures which implies that both, the methods for tailoring of the proper structure shape and size and methods for subsequent characterization of the prepared structures are needed.

In Chapter 3 we discussed one of the most prominent nano-imaging techniques, the scattering type near-field optical microscopy. We have shown, that the interpretation of the s-SNOM images is not straightforward and we have proposed a model for interpretation of images obtained with weakly scattering probes. The model presented in this thesis brings a new insight to the interpretation of the near-field maps in terms of the near-field components. We conclude that the s-SNOM polarization resolved signal is formed as a scalar product of the antenna electric near-field with the auxiliary electric field, which would be excited around the antenna by a source of the same polarization and in the same position as the signal detector, weighted by the polarizability of the tip. The signal consequently emerges as a quadratic expression of the real near-field components and the auxiliary field components. The theoretically calculated images of infrared linear antennas were compared with experiments and a good match between the experiment and the theory was found. The signal was shown to be either linearly or quadratically dependent on the antenna near-field components in different polarization detection schemes, in other words, depending on the distribution of the auxiliary fields.

Conclusions of Chapter 3 have a huge practical influence for nano-characterization of resonant metallic structures and elucidate the near-field mechanism of the signal formation. However, the proposed model is restricted only to situations where a weakly interacting tip is used for the detection. This is not the case for strongly polarizable metallic tips, where the signal can not be obtained with help of the formalism developed herein. Anyway, we hope that the introduced formalism of s-SNOM signal formation might serve as a starting point for further analysis of in-

teraction between the strongly scattering tips and the sample antennas. We have also proposed a novel experimental arrangement on which the model for weakly interacting tips could be conclusively tested. The designed experiment may also help on the way to find the boundaries between the weak interaction and the strong interaction regime.

The practical importance of the infrared antennas rests especially in their application for surface enhanced infrared spectroscopy, which was discussed in Chapter 5. We discussed the interaction of the infrared linear antennas with analysed samples having a vibrational resonance close to the resonance of the antenna. Particularly, we performed a theoretical study of a model system where the antenna was covered by a layer of a artificial SiO_2. We established a simple analytical model for description of the coupling between the antenna mode and the sample modes. The model successfully described the spectra of the studied system which we calculated numerically. The main message of the model study of the antenna covered by a homogeneous sample layer is that the shape of the container in which the sample material is contained has an essential role for formation of the spectral signal. This detail should not be overlooked in the experimental studies.

Next we focused our attention on the influence of the near-field enhancement of the antenna in a position where the sample is placed. We touched the problem of a quantitative analysis in SEIRS. Due to an unclear border between the strength of the sample resonance and the near-field enhancement in the sample position, the quantitative analysis of SEIRS experiments seems to be quite remote. We decided to study solely the contribution of the bare antenna near-field enhancement on the size of the characteristic antiresonance dip in the extinction spectrum. For this purpose, we used a model where a pair of SiO_2 rings was placed symmetrically into different positions along the antenna. Our numerical calculations have shown that the dip size measured in the extinction spectrum of the antenna-sample system varies with the enhancement of the antenna near-field almost linearly in the strong interaction regime. We compared results of our calculations with similar study from literature and concluded that there is a manifest qualitative distinction between spectroscopic signal size when the antenna-sample interaction is weak and when the interaction is strong.

For weakly interacting samples, we found ourselves in a situation which resembled the interaction of the weakly polarizable s-SNOM probe with the antenna. We also stated the connection between the s-SNOM signal obtained in the weak interaction regime and the size of the dip in the extinction spectrum. The connection follows from the possibility to write the transmitted electric field as a superposition of the field passing through the bare antenna plus term which appears due to the mutual antenna-sample interaction. The difference from the original antenna spectrum is shown to depend linearly on the interaction term. As it was shown in Chapter 3, it is the interaction term which is detected in the scattering type near-field microscopy. The connection between the s-SNOM measurements and the infrared spectroscopy is tight and experiments performed in one field have also impact in the other field. The near-field microscopy is therefore capable of mapping the spectroscopic enhancement caused by the sample antenna and conversely, the static spectroscopic measurements help to interpret the near-field images obtained with s-SNOM.

A special chapter, Chapter 4, was reserved for novel experimental developments in the field of near-field microscopy. Two state-of-the-art methods utilizing photoluminescence either as a novel method for near-field signal separation or as a tool for probing a totally different near-field quantity, the LDOS, were put forward. These methods find application especially in the visible part of the electromagnetic spectrum where the properties of the sample metallic structures are applied especially for the field enhanced optical spectroscopy. The topic of antennas in optics overwhelms the scope of the thesis. We present the methods operated dominantly in optics to complete the discussion of the tip based near-field imaging techniques.

Appendices

A | Surface modes of cylindrical shell

In this appendix we will calculate surface modes of cylindrical shell in quasi-static approximation. The cylindrical shell will be defined by inner radius a and outer radius b. We start with usual onset, considering the solutions of Laplace equation in cylindrical coordinates (ρ, φ, z) and imposing the standard boundary conditions. Solution of the Laplace equation must be regular in the center of the cylinder; similarly, the solution outside of the shell should not diverge for infinite ρ. The solutions in the inner region (i), region in between the two boundaries (m) and outside of the shell (e) read:

$$\phi^{(\mathrm{i})} = C_1 \mathrm{I}_m(\kappa\rho)\exp(\mathrm{i}\kappa z)\exp(\mathrm{i}m\varphi), \tag{A.1}$$
$$\phi^{(\mathrm{m})} = [C_2 \mathrm{I}_m(\kappa\rho)\exp(\mathrm{i}\kappa z) + C_3 \mathrm{K}_m(\kappa\rho)\exp(\mathrm{i}\kappa z)]\exp(\mathrm{i}m\varphi), \tag{A.2}$$
$$\phi^{(\mathrm{e})} = C_4 \mathrm{K}_m(\kappa\rho)\exp(\mathrm{i}\kappa z)\exp(\mathrm{i}m\varphi). \tag{A.3}$$

The condition of continuity of the potential and the normal component of electric induction on the boundaries $\rho = a$ and $\rho = b$ yields

$$C_1 \mathrm{I}_m(\kappa a) = C_2 \mathrm{I}_m(\kappa a) + C_3 \mathrm{K}_m(\kappa a), \tag{A.4}$$
$$C_1 \mathrm{I}'_m(\kappa a) = \varepsilon\left[C_2 \mathrm{I}'_m(\kappa a) + C_3 \mathrm{K}'_m(\kappa a)\right], \tag{A.5}$$
$$C_4 \mathrm{K}_m(\kappa b) = C_2 \mathrm{I}_m(\kappa b) + C_3 \mathrm{K}_m(\kappa b), \tag{A.6}$$
$$C_4 \mathrm{K}'_m(\kappa b) = \varepsilon\left[C_2 \mathrm{I}'_m(\kappa b) + C_3 \mathrm{K}'_m(\kappa b)\right], \tag{A.7}$$
$$\tag{A.8}$$

where we considered that the shell has dielectric function ε in the region (m) and is surrounded by vacuum. The bar denotes derivative with respect to argument. The set of four equations for four coefficients C_1, C_2, C_3 and C_4 has solution only when the equations (A.4) to (A.7) are linearly dependent. Hence

$$\varepsilon^2[D(\kappa) - N(k)] + \varepsilon[A(\kappa) + B(\kappa) - 2D(\kappa)] + D(\kappa) - C(\kappa) = 0 \tag{A.9}$$

must be fulfilled. In the following we will restrict ourselves for discussion of the rotationally symmetric mode ($m = 0$). The functions of wavenumber $A(\kappa)$, $B(\kappa)$,

$C(\kappa)$, $D(\kappa)$ and $N(\kappa)$ are defined accordingly

$$A(\kappa) = \mathrm{I}_1(\kappa b)\mathrm{K}_0(\kappa b)\mathrm{K}_0(\kappa a)\mathrm{I}_1(\kappa a), \tag{A.10}$$
$$B(\kappa) = \mathrm{K}_1(\kappa b)\mathrm{I}_0(\kappa b)\mathrm{I}_0(\kappa a)\mathrm{K}_1(\kappa a), \tag{A.11}$$
$$C(\kappa) = -\mathrm{I}_0(\kappa b)\mathrm{K}_1(\kappa b)\mathrm{K}_0(\kappa a)\mathrm{I}_1(\kappa a), \tag{A.12}$$
$$D(\kappa) = -\mathrm{K}_0(\kappa b)\mathrm{K}_1(\kappa b)\mathrm{I}_0(\kappa a)\mathrm{I}_1(\kappa a), \tag{A.13}$$
$$N(\kappa) = \mathrm{I}_1(\kappa b)\mathrm{K}_0(\kappa b)\mathrm{I}_0(\kappa a)\mathrm{K}_1(\kappa a). \tag{A.14}$$
$$\tag{A.15}$$

We consider now the dielectric function of the material in form of the Lorentz dielectric function, disregarding losses

$$\varepsilon(\omega) = \varepsilon_\infty + \frac{\Omega^2}{\omega_{\mathrm{TO}}^2 - \omega^2}. \tag{A.16}$$

The dispersion relation $\omega(\kappa)$ can now be obtained explicitly from equation (A.9) together with (A.16):

$$\omega^2 = \frac{1}{2}\frac{1}{\varepsilon_\infty^2[D-N] + \varepsilon_\infty[A+B-2D] + D - C}\left[F \pm G\right], \tag{A.17}$$

where

$$\begin{aligned} F =& 2\varepsilon_\infty^2\omega_{\mathrm{TO}}^2\left[D - N + \frac{A+B-2D}{\varepsilon_\infty}\right] + 2\varepsilon_\infty\Omega^2[D-N] + \\ &+ \Omega^2[A+B-2D] + 2\omega_{\mathrm{TO}}^2[D-C] \end{aligned} \tag{A.18}$$

and

$$G = \Omega^2\sqrt{[A+B]^2 - 4[AD + BD + CN - CD - DN]}. \tag{A.19}$$

B | Analytical model parameters

The parameters used in the analytical were adjusted by hand to show a best visual match with the numerical spectra. Here we present the model parameters for varying layer thickness. Note that the important value is the product of the coupling coefficient and the oscillator strength. The notation of the parameters corresponds to equations (5.31) and (5.40).

Table B.1: Model parameters used for calculation of the spectra for different layer thickness t. We used $\gamma_{\mathrm{LO}} = 13.5\,\mathrm{cm}^{-1}$, $\gamma_{\mathrm{TO}} = 21.2\,\mathrm{cm}^{-1}$, $\gamma_{\mathrm{SPP}} = 15.9\,\mathrm{cm}^{-1}$.

t/nm	α_{BG}/F m^2	f_{LO}/F m^2 cm^{-2}	f_{TO}/F m^2 cm^{-2}	f_{SPP}/F m^2 cm^{-2}	R_{eff}/nm
3	$1.44 \cdot 10^{-34}$	$3.92 \cdot 10^{-26}$	$4.97 \cdot 10^{-28}$	$5.58 \cdot 10^{-28}$	610
10	$1.03 \cdot 10^{-33}$	$7.85 \cdot 10^{-26}$	$4.97 \cdot 10^{-28}$	$5.58 \cdot 10^{-28}$	570
30	$1.44 \cdot 10^{-33}$	$6.54 \cdot 10^{-26}$	$4.97 \cdot 10^{-28}$	$1.86 \cdot 10^{-27}$	495
100	$1.08 \cdot 10^{-33}$	$6.54 \cdot 10^{-26}$	$1.99 \cdot 10^{-27}$	$3.72 \cdot 10^{-27}$	420

The oscillator resonant frequencies ω_{LO}, ω_{TO}, ω_{SPP} were held close to the frequencies calculated in the main text with negligible variations (less than $10\,\mathrm{cm}^{-1}$).

Bibliography

[1] P. Muhlschlegel, H.-J. Eisler, O. J. F. Martin, B. Hecht, and D. W. Pohl. Resonant optical antennas. *Science*, 308(5728):1607–1609, 2005.

[2] M. Schnell, A. García-Etxarri, A. J. Huber, K. Crozier, J. Aizpurua, and R. Hillenbrand. Controlling the near-field oscillations of loaded plasmonic nanoantennas. *Nature Photonics*, 3(5):287–291, 2009.

[3] P. Bharadwaj, B. Deutsch, and L. Novotny. Optical antennas. *Advances in Optics and Photonics*, 1(3):438–483, 2009.

[4] R. Kalousek, P. Dub, L. Břínek, and T. Šikola. Response of plasmonic resonant nanorods: an analytical approach to optical antennas. *Optics express*, 20(16):17916–17927, 2012.

[5] L. Novotny. Effective wavelength scaling for optical antennas. *Physical Review Letters*, 98(26):266802, 2007.

[6] L. Novotny and N. van Hulst. Antennas for light. *Nature Photonics*, 5(2):83–90, 2011.

[7] S. Nie and S. R. Emory. Probing single molecules and single nanoparticles by surface-enhanced Raman scattering. *Science*, 275(5303):1102–1106, 1997.

[8] D. R. Ward, N. K. Grady, C. S. Levin, N. J. Halas, Y. Wu, P. Nordlander, and D. Natelson. Electromigrated nanoscale gaps for surface-enhanced Raman spectroscopy. *Nano Letters*, 7(5):1396–1400, 2007.

[9] R. F. Aroca. Plasmon enhanced spectroscopy. *Physical Chemistry Chemical Physics*, 15(15):5355–5363, 2013.

[10] K. Kneipp, Y. Wang, H. Kneipp, L. T. Perelman, I. Itzkan, R. R. Dasari, and M. S. Feld. Single molecule detection using surface-enhanced raman scattering (SERS). *Physical Review Letters*, 78(9):1667–1670, 1997.

[11] C. D'Andrea, J. Bochterle, A. Toma, C. Huck, F. Neubrech, E. Messina, B. Fazio, O. M. Maragò, E. Di Fabrizio, M. Lamy de La Chapelle, P. G. Gucciardi, and A. Pucci. Optical nanoantennas for multiband surface-enhanced infrared and Raman spectroscopy. *ACS Nano*, 7(4):3522–3531, 2013.

[12] F. Neubrech and A. Pucci. Plasmonic enhancement of vibrational excitations in the infrared. *IEEE Journal of Selected Topics in Quantum Electronics*, 19(3):4600809, 2013.

[13] J. Bochterle, F. Neubrech, T. Nagao, and A. Pucci. Angstrom-scale distance dependence of antenna-enhanced vibrational signals. *ACS Nano*, 6(12):10917–10923, 2012.

[14] L. V. Brown, K. Zhao, N. King, H. Sobhani, P. Nordlander, and N. J. Halas. Surface-enhanced infrared absorption using individual cross antennas tailored to chemical moieties. *Journal of American Chemical Society*, 135(9):3688–3695, 2013.

[15] A. Otto. The 'chemical' (electronic) contribution to surface-enhanced Raman scattering. *Journal of Raman Spectroscopy*, 36(6-7):497–509, 2005.

[16] A. Otto. Surface-enhanced Raman scattering of adsorbates. *Journal of Raman Spectroscopy*, 22(12):743–752, 1991.

[17] A. Campion and P. Kambhampati. Surface-enhanced Raman scattering. *Chemical Society Reviews*, 27(4):241–250, 1998.

[18] R. Esteban, A. G. Borisov, P. Nordlander, and J. Aizpurua. Bridging quantum and classical plasmonics with a quantum-corrected model. *Nature Communications*, 3:825, 2012.

[19] L. Novotny and B. Hecht. *Principles of Nano-Optics*. Cambridge University Press, New York, 2006.

[20] M. Agio and A. Aliu. *Optical antennas*. Cambridge University Press, Cambridge, 2013.

[21] A. J. Ward and J. B. Pendry. Refraction and geometry in Maxwell's equations. *Journal of Modern Optics*, 43(4):773–793, 1996.

[22] A. Aubry, D. Y. Lei, A. I. Fernández-Domínguez, Y. Sonnefraud, S. A. Maier, and J. B. Pendry. Plasmonic light-harvesting devices over the whole visible spectrum. *Nano Letters*, 10(7):2574–2579, 2010.

[23] A. Aubry, D. Y. Lei, S. A. Maier, and J. B. Pendry. Plasmonic hybridization between nanowires and a metallic surface: A transformation optics approach. *ACS Nano*, 5(4):3293–3308, 2011.

[24] E.H. Synge. XXXVIII. A suggested method for extending microscopic resolution into the ultra-microscopic region. *Philosophical Magazine Series 7*, 6(35):356–362, 1928.

[25] E.H. Synge. III. a microscopic method. *Philosophical Magazine Series 7*, 11(68):65–80, 1931.

[26] J.W. Strutt. LVIII. On the scattering of light by small particles. *Philosophical Magazine Series 4*, 41(275):447–454, 1871.

[27] G. Mie. Beiträge zur optik trüber medien, speziell kolloidaler metallösungen. *Annalen der Physik*, 330:377–445, 1908.

[28] Lumerical solutions, inc. `http://www.lumerical.com/tcad-products/fdtd/`, visited 2014-05-20.

[29] Comsol inc. `http://www.comsol.com/`, visited 2014-05-20.

[30] F. J. García de Abajo and A. Howie. Retarded field calculation of electron energy loss in inhomogeneous dielectrics. *Physical Review B*, 65(11):115418, 2002.

[31] U. Hohenester and A. Trügler. MNPBEM - a matlab toolbox for the simulation of plasmonic nanoparticles. *Computer Physics Communications*, 183(2):370 – 381, 2012.

[32] B. A. Lippmann and J. Schwinger. Variational principles for scattering processes. I. *Physical Review*, 79(3):469–480, 1950.

[33] B. A. Lippmann. Variational principles for scattering processes. II. Scattering of slow neutrons by para-hydrogen. *Physical Review*, 79(3):481–486, 1950.

[34] A.D. Yaghjian. Electric dyadic Green's functions in the source region. *Proceedings of the IEEE*, 68(2):248–263, 1980.

[35] O. Keller. *Quantum theory of near-field electrodynamics*. Springer Berlin Heidelberg, Berlin, 2011.

[36] P. de Vries, D. V. van Coevorden, and A. Lagendijk. Point scatterers for classical waves. *Review of Modern Physics*, 70:447–466, 1998.

[37] C.-T. Tai. *Dyadic green functions in electromagnetic theory*. IEEE Press, Piscataway, NJ, 1994.

[38] Leung Tsang. *Scattering of electromagnetic waves*. Wiley, New York, 2000.

[39] J. A. Stratton. *Electromagnetic Theory*. New York: McGraw-Hill, New York, 1941.

[40] J. Nelayah, M. Kociak, O. Stephan, F. J. Garcia de Abajo, M. Tence, L. Henrard, D. Taverna, I. Pastoriza-Santos, L. M. Liz-Marzan, and C. Colliex. Mapping surface plasmons on a single metallic nanoparticle. *Nature Physics*, 3(5):348–353, 2007.

[41] U. Hohenester, H. Ditlbacher, and J. R. Krenn. Electron-energy-loss spectra of plasmonic nanoparticles. *Physical Review Letters*, 103(10):106801, 2009.

[42] F. J. García de Abajo and A. Howie. Relativistic electron energy loss and electron-induced photon emission in inhomogeneous dielectrics. *Physical Review Letters*, 80(23):5180–5183, 1998.

[43] M. Burresi, D. van Oosten, T. Kampfrath, H. Schoenmaker, R. Heideman, A. Leinse, and L. Kuipers. Probing the magnetic field of light at optical frequencies. *Science*, 326(5952):550–553, 2009.

[44] J.-J. Greffet and R. Carminati. Image formation in near-field optics. *Progress in Surface Science*, 56(3):133–237, 1997.

[45] R. Hillenbrand and F. Keilmann. Complex optical constants on a subwavelength scale. *Physical Review Letters*, 85(14):3029–3032, 2000.

[46] R. Hillenbrand, F. Keilmann, P. Hanarp, D. S. Sutherland, and J. Aizpurua. Coherent imaging of nanoscale plasmon patterns with a carbon nanotube optical probe. *Applied Physics Letters*, 83(2):368–370, 2003.

[47] N. Ocelic, A. Huber, and R. Hillenbrand. Pseudoheterodyne detection for background-free near-field spectroscopy. *Applied Physics Letters*, 89(10):101124, 2006.

[48] M. Schnell, A. Garcia-Etxarri, J. Alkorta, J. Aizpurua, and R. Hillenbrand. Phase-resolved mapping of the near-field vector and polarization state in nanoscale antenna gaps. *Nano Letters*, 10(9):3524–3528, 2010.

[49] H. Gersen, L. Novotny, L. Kuipers, and N. F. van Hulst. On the concept of imaging nanoscale vector fields. *Nature Photonics*, 1(5):242, 2007.

[50] J. A. Porto, P. Johansson, S. P. Apell, and T. López-Ríos. Resonance shift effects in apertureless scanning near-field optical microscopy. *Physical Review B*, 67(8):085409, 2003.

[51] A. J. Huber, F. Keilmann, J. Wittborn, J. Aizpurua, and R. Hillenbrand. Terahertz near-field nanoscopy of mobile carriers in single semiconductor nanodevices. *Nano Letters*, 8(11):3766–3770, 2008.

[52] J. M. Stiegler, A. J. Huber, S. L. Diedenhofen, J. Gómez Rivas, R. E. Algra, E. P. A. M. Bakkers, and R. Hillenbrand. Nanoscale free-carrier profiling of individual semiconductor nanowires by infrared near-field nanoscopy. *Nano Letters*, 10(4):1387–1392, 2010.

[53] S. Jäger, A. M. Kern, M. Hentschel, R. Jäger, K. Braun, D. Zhang, H. Giessen, and A. J. Meixner. Au nanotip as luminescent near-field probe. *Nano Letters*, 13(8):3566–3570, 2013.

[54] F. Keilmann and R. Hillenbrand. Near-field microscopy by elastic light scattering from a tip. *Philosophical Transactions-Royal Society of London Series A, Mathematical, Physical and Engineering Sciences*, 362(1817):787–806, 2004.

[55] M. Schnell, P. S. Carney, and R. Hillenbrand. Synthetic optical holography for rapid nanoimaging. *Nature Commununications*, 5:3499, 2014.

[56] L. Gomez, R. Bachelot, A. Bouhelier, G. P. Wiederrecht, S. Chang, S. K. Gray, F. Hua, S. Jeon, J. A. Rogers, M. E. Castro, S. Blaize, I. Stefanon, G. Lerondel, and P. Royer. Apertureless scanning near-field optical microscopy: a comparison between homodyne and heterodyne approaches. *Journal of the Optical Society of America B*, 23(5):823–833, 2006.

[57] P. Alonso-González, P. Albella, F. Golmar, L. Arzubiaga, F. Casanova, L. E. Hueso, J. Aizpurua, R. Hillenbrand, and et al. Visualizing the near-field coupling and interference of bonding and anti-bonding modes in infrared dimer nanoantennas. *Optics express*, 21(1):1270–1280, 2013.

[58] O. Keller, M. Xiao, and S. Bozhevolnyi. Configurational resonances in optical near-field microscopy: a rigorous point-dipole approach. *Surface Science*, 280(1-2):217–230, 1993.

[59] J. Sun, P. S. Carney, and J. C. Schotland. Strong tip effects in near-field scanning optical tomography. *Journal of Applied Physics*, 102(10):103103, 2007.

[60] B. Deutsch, R. Hillenbrand, and L. Novotny. Visualizing the optical interaction tensor of a gold nanoparticle pair. *Nano Letters*, 10(2):652–656, 2010.

[61] M. Rang, A. C. Jones, F. Zhou, Z.-Y. Li, B. J. Wiley, Y. Xia, and M. B. Raschke. Optical near-field mapping of plasmonic nanoprisms. *Nano Letters*, 8(10):3357–3363, 2008.

[62] M. Esslinger and R. Vogelgesang. Reciprocity theory of apertureless scanning near-field optical microscopy with point-dipole probes. *ACS Nano*, 6(9):8173–8182, 2012.

[63] M. Moskovits. Surface-enhanced spectroscopy. *Review of Modern Physics*, 57(3):783–826, 1985.

[64] D. Dregely, F. Neubrech, H. Duan, R. Vogelgesang, and H. Giessen. Vibrational near-field mapping of planar and buried three-dimensional plasmonic nanostructures. *Nature Communications*, 4:2237, 2013.

[65] P. Alonso-González, P. Albella, M. Schnell, J. Chen, F. Huth, A. García-Etxarri, F. Casanova, F. Golmar, L. Arzubiaga, L. E. Hueso, J. Aizpurua, and R. Hillenbrand. Resolving the electromagnetic mechanism of surface-enhanced light scattering at single hot spots. *Nature Commununications*, 3:684, 2012.

[66] R. Hillenbrand, M. Stark, and R. Guckenberger. Higher-harmonics generation in tapping-mode atomic-force microscopy: Insights into the tip-sample interaction. *Applied Physics Letters*, 76(23):3478, 2000.

[67] R. Esteban, R. Vogelgesang, and K. Kern. Tip-substrate interaction in optical near-field microscopy. *Physical Review B*, 75(19):195410, 2007.

[68] D.-S. Kim, J. Heo, S.-H. Ahn, S. W. Han, W. S. Yun, and Z. H. Kim. Real-space mapping of the strongly coupled plasmons of nanoparticle dimers. *Nano Letters*, 9(10):3619–3625, 2009.

[69] P. Alonso-Gonzalez, M. Schnell, P. Sarriugarte, H. Sobhani, C. Wu, N. Arju, A. Khanikaev, F. Golmar, P. Albella, L. Arzubiaga, F. Casanova, L. E. Hueso, P. Nordlander, G. Shvets, and R. Hillenbrand. Real-space mapping of fano interference in plasmonic metamolecules. *Nano Letters*, 11(9):3922–3926, 2011.

[70] S. Scheel, L. Knöll, and D.-G. Welsch. Spontaneous decay of an excited atom in an absorbing dielectric. *Physical Review A*, 60(5):4094–4104, 1999.

[71] R. Carminati, J.-J. Greffet, C. Henkel, and J. M. Vigoureux. Radiative and non-radiative decay of a single molecule close to a metallic nanoparticle. *Optics Communications*, 261(2):368–375, 2006.

[72] S. D'Agostino, F. Della Sala, and L. C. Andreani. Dipole-excited surface plasmons in metallic nanoparticles: Engineering decay dynamics within the discrete-dipole approximation. *Physical Review B*, 87(20):205413, 2013.

[73] L. Rogobete, F. Kaminski, M. Agio, and V. Sandoghdar. Design of plasmonic nanoantennae for enhancing spontaneous emission. *Optics Letters*, 32(12):1623–1625, 2007.

[74] K. H. Drexhage. Influence of a dielectric interface on fluorescence decay time. *Journal of Luminescence*, 1(2):693–701, 1970.

[75] O. Kulakovich, N. Strekal, A. Yaroshevich, S. Maskevich, S. Gaponenko, I. Nabiev, U. Woggon, and M. Artemyev. Enhanced luminescence of CdSe quantum dots on gold colloids. *Nano Letters*, 2(12):1449–1452, 2002.

[76] A. W. Schell, P. Engel, J. F. M. Werra, C. Wolff, K. Busch, and O. Benson. Scanning single quantum emitter fluorescence lifetime imaging: Quantitative analysis of the local density of photonic states. *Nano Letters*, 0(0):null, 2014.

[77] K. Imura, T. Nagahara, and H. Okamoto. Near-field two-photon-induced photoluminescence from single gold nanorods and imaging of plasmon modes. *The Journal of Physical Chemistry B*, 109(27):13214–13220, 2005.

[78] M. R. Beversluis, A. Bouhelier, and L. Novotny. Continuum generation from single gold nanostructures through near-field mediated intraband transitions. *Physical Review B*, 68(11):115433, 2003.

[79] E. Dulkeith, T. Niedereichholz, T. A. Klar, J. Feldmann, G. von Plessen, D. I. Gittins, K. S. Mayya, and F. Caruso. Plasmon emission in photoexcited gold nanoparticles. *Physical Review B*, 70(20):205424, 2004.

[80] M. Yorulmaz, S. Khatua, P. Zijlstra, A. Gaiduk, and M. Orrit. Luminescence quantum yield of single gold nanorods. *Nano Letters*, 12(8):4385–4391, 2012.

[81] Y. Fang, W.-S. Chang, B. Willingham, P. Swanglap, S. Dominguez-Medina, and S. Link. Plasmon emission quantum yield of single gold nanorods as a function of aspect ratio. *ACS Nano*, 6(8):7177–7184, 2012.

[82] F. Wackenhut, A. V. Failla, and A. J. Meixner. Multicolor microscopy and spectroscopy reveals the physics of the one-photon luminescence in gold nanorods. *The Journal of Physical Chemistry C*, 117(34):17870–17877, 2013.

[83] T. V. Shahbazyan. Theory of plasmon-enhanced metal photoluminescence. *Nano Letters*, 13(1):194–198, 2013.

[84] H. Hu, H. Duan, J. K. W. Yang, and Z. X. Shen. Plasmon-modulated photoluminescence of individual gold nanostructures. *ACS Nano*, 6(11):10147–10155, 2012.

[85] F. Neubrech, A. Pucci, T. W. Cornelius, S. Karim, A. García-Etxarri, and J. Aizpurua. Resonant plasmonic and vibrational coupling in a tailored nanoantenna for infrared detection. *Physical Review Letters*, 101(15):157403, 2008.

[86] H. Xu, E. J. Bjerneld, M. Käll, and L. Börjesson. Spectroscopy of single hemoglobin molecules by surface enhanced Raman scattering. *Physical Review Letters*, 83(21):4357–4360, 1999.

[87] M. Fleischmann, P.J. Hendra, and A.J. McQuillan. Raman spectra of pyridine adsorbed at a silver electrode. *Chemical Physics Letters*, 26(2):163–166, 1974.

[88] H. Xu, J. Aizpurua, M. Käll, and P. Apell. Electromagnetic contributions to single-molecule sensitivity in surface-enhanced Raman scattering. *Physical Review E*, 62(3):4318–4324, 2000.

[89] D. L. Rousseau and P. F. Williams. Resonance Raman scattering of light from a diatomic molecule. *The Journal of Chemical Physics*, 64(9):3519–3537, 1976.

[90] J. F. Li, Y. F. Huang, Y. Ding, and et al. Shell-isolated nanoparticle-enhanced raman spectroscopy. *Nature*, 464(7287):392–395, 2010.

[91] B. Pettinger, B. Ren, G. Picardi, R. Schuster, and G. Ertl. Nanoscale probing of adsorbed species by tip-enhanced Raman spectroscopy. *Physical Review Letters*, 92(9):096101, 2004.

[92] E. A. Pozzi, M. D. Sonntag, N. Jiang, J. M. Klingsporn, M. C. Hersam, and R. P. Van Duyne. Tip-enhanced Raman imaging: An emergent tool for probing biology at the nanoscale. *ACS Nano*, 7(2):885–888, 2013.

[93] U. Fano. Effects of configuration interaction on intensities and phase shifts. *Physcal Review*, 124(6):1866–1878, 1961.

[94] B. Gallinet and O. J. F. Martin. Ab initio theory of Fano resonances in plasmonic nanostructures and metamaterials. *Physical Review B*, 83(23):235427, 2011.

[95] P. Alonso-González, P. Albella, F. Neubrech, C. Huck, J. Chen, F. Golmar, F. Casanova, L. E. Hueso, A. Pucci, J. Aizpurua, and R. Hillenbrand. Experimental verification of the spectral shift between near- and far-field peak intensities of plasmonic infrared nanoantennas. *Physical Review Letters*, 110(20):203902, 2013.

[96] R. Adato, A. Artar, S. Erramilli, and H. Altug. Engineered absorption enhancement and induced transparency in coupled molecular and plasmonic resonator systems. *Nano Letters*, 13(6):2584–2591, 2013.

[97] C. F. Bohren and D. R. Huffman. *Absorption and scattering of ligth by small particles*. John Wiley & Sons, New York, 1983.

[98] S. Albaladejo, R. Gómez-Medina, L. S. Froufe-Pérez, H. Marinchio, R. Carminati, J. F. Torrado, G. Armelles, A. García-Martín, and J. J. Sáenz. Radiative corrections to the polarizability tensor of an electrically small anisotropic dielectric particle. *Optics Express*, 18(4):3556–3567, 2010.

[99] A. A. Govyadinov, I. Amenabar, F. Huth, P. S. Carney, and R. Hillenbrand. Quantitative measurement of local infrared absorption and dielectric function with tip-enhanced near-field microscopy. *The Journal of Physical Chemistry Letters*, 4(9):1526–1531, 2013.

[100] W. Zhang, B. Gallinet, and O. J. F. Martin. Symmetry and selection rules for localized surface plasmon resonances in nanostructures. *Physical Review B*, 81(23):233407, 2010.

[101] M. A. Kats, N. Yu, P. Genevet, Z. Gaburro, and F. Capasso. Effect of radiation damping on the spectral response of plasmonic components. *Optics Express*, 19(22):21748–21753, 2011.

[102] C. Forestiere, L. Dal Negro, and G. Miano. Theory of coupled plasmon modes and fano-like resonances in subwavelength metal structures. *Physical Review B*, 88(15):155411, 2013.

[103] E. Castanié, R. Vincent, R. Pierrat, and R. Carminati. Absorption by an optical dipole antenna in a structured environment. *International Journal of Optics*, 2012(2012):452047, 2012.

[104] R. Marty, A. Mlayah, A. Arbouet, C. Girard, and S. Tripathy. Plasphonics: local hybridization of plasmons and phonons. *Optics Express*, 21(4):4551–4559, 2013.

[105] F. Neubrech, D. Weber, D. Enders, T. Nagao, and A. Pucci. Antenna sensing of surface phonon polaritons. *The Journal of Physical Chemistry C*, 114(16):7299–7301, 2010.

[106] R. Fuchs and K. L. Kliewer. Optical modes of vibration in an ionic crystal slab. *Physical Review*, 140(6A):A2076–A2088, 1965.

[107] K. L. Kliewer and R. Fuchs. Optical modes of vibration in an ionic crystal slab including retardation. I. nonradiative region. *Physical Review*, 144(2):495–503, 1966.

[108] E.D. Palik. *Handbook of Optical Constants of Solids*. Number vol. 2 in Academic Press handbook series. 1991.

[109] R. Englman and R. Ruppin. Optical lattice vibrations in finite ionic crystals: I. *Journal of Physics C: Solid State Physics*, 1(3):614, 1968.

[110] J. Schwinger, L. L. Deraad, K. A. Milton, W. Tsai, and J. Norton. *Classical electrodynamics*. Perseus Books, Reading, Massachusetts, 1998.